

Mesoscale eddies observed by moored current-meters at abyssal depths in the western North Pacific during 1978–1985

Shiro IMAWAKI¹⁾ * and Kenzo TAKANO²⁾

Abstract: Observations by moored current-meters were carried out repeatedly in mid-ocean of the western North Pacific, providing 50 velocity records. A continuous velocity record for almost seven years was obtained at 5000 m depth. The overall mean velocity is directed to the north with a speed of less than 1 cm s^{-1} . The kinetic energy of low-frequency velocity-fluctuations, or mesoscale eddies is more than 30 times larger than that of mean flow. Frequency spectra of eddy kinetic energy show that most of the energy is contained in mesoscale bands (periods of 31–235 days), with zonal (meridional) dominance of energy in the longer (shorter) period band. An array observation at 4000 m depth shows that the local change of relative vorticity of mesoscale eddies is balanced mainly with the advection of planetary vorticity, although the horizontal advection of relative vorticity and higher-order horizontal divergence may play some role. Those results suggest that the mesoscale eddies are understood as primarily plane barotropic Rossby waves with possible modification.

Keywords : *mesoscale eddies, moored current-meter, frequency spectrum, vorticity balance*

1. Introduction

Synoptic current fluctuations having typical temporal scales of weeks to months and horizontal scales of tens to hundreds of kilometers are called “mesoscale eddies.” They are also called “low-frequency fluctuations” or “low-frequency eddies.” Mesoscale eddies dominate in the mid-ocean flow field (ROBINSON, 1983). They were first recognized from observations in 1959 by neutrally-buoyant floats at mid-depths in the North Atlantic (CREASE, 1962). They have been measured by moored current-meters and neu-

trally-buoyant floats at depth, most intensively in 1970s and 1980s. The highlight was the Mid-Ocean Dynamics Experiment (MODE) carried out in 1973 in the western North Atlantic (MODE GROUP, 1978). Mesoscale eddies at surface layers have been measured by surface drifting-buoys tracked by satellites (NILER, 2001). Since the Topex/Poseidon satellite was launched in 1992, mesoscale eddies have been intensively measured by satellite altimeters; details of mesoscale eddies with surface manifestation have been revealed, especially for their global views (FU and MORROW, 2013).

To understand the nature of mesoscale eddies, their mechanisms and their roles in ocean circulation, observations at depth are necessary as well as surface observations. A considerable

1) Professor Emeritus of Kyushu University, Yokohama, 224-0014, Japan

2) Matsudo, Chiba Prefecture, 271-0064, Japan

*Corresponding author:

E-mail: imawaki@g04.itscom.net

fraction of velocity and temperature fluctuations observed in the MODE area is accounted for by a combination of barotropic and first-mode baroclinic Rossby waves (MCWILLIAMS and FLIERL, 1976). In the Gulf Stream recirculation region in the North Atlantic, a barotropic Rossby wave modified by bottom topography was observed beneath the thermocline (PRICE and ROSSBY, 1982). At a site called R to the east of the Izu-Ogasawara Ridge in the western North Pacific, a considerable fraction of mesoscale eddies at abyssal depths is accounted for by a set of three barotropic Rossby waves (IMAWAKI, 1985). Recent studies show that fluctuations at the same site having specific spectral peaks are explained by plane topographic Rossby waves (MIYAMOTO *et al.*, 2017; 2019). Under the Kuroshio Extension, topographic Rossby waves in a period band of 30–60 days were observed (GREENE *et al.*, 2012).

Examination of vorticity balance of mesoscale eddies at 1500 m depth in the MODE area shows that a 10-day mean balance is highly nonlinear but a 60-day mean balance is marginally linear (MCWILLIAMS, 1976). In the North Equatorial Current region in the Atlantic, the local change of relative vorticity is balanced with the advection of planetary vorticity in the thermocline as well as in the deep layer, for a period band of 24–81 days (KEFFER, 1983). At the Site R to the east of the Izu-Ogasawara Ridge, the local change of relative vorticity is accounted for by the advection of planetary vorticity at 5000 m depth within the estimated error (IMAWAKI, 1983).

These studies suggest that the dynamics of mid-ocean mesoscale eddies differs at locations, depths and temporal/spatial scales, and further examinations are required to understand the eddy field. Intensive observations by moored current-meters were carried out at abyssal depths at more than 20 stations in the Site R during

1978–1985, in order to primarily investigate mesoscale eddies. The present paper provides description of the velocity measurements and results obtained mostly on mesoscale eddies.

The rest of the paper is organized as follows. Section 2 describes the observation site, mooring operations, current measurements and data processing. Section 3 gives general statistics of individual velocity records and describes combining individual records. Section 4 shows features of mean flows. Section 5 describes statistical features of mesoscale eddies. Section 6 shows features of frequency spectra. Section 7 describes the vorticity balance of mesoscale eddies using the current-meter data, with Subsection 7.1 on Array-83 and Subsection 7.2 on Array-84. Sections 8 and 9 are discussions and summary, respectively.

2. Current measurements

The observation site called R is centered at 30°N, 147°E in the western North Pacific. At shallow depths, the site center is located about 400 km south of the Kuroshio Extension (Fig. 1) and on the indistinct southern boundary of the broad west-southwestward flowing Kuroshio Countercurrent (UCHIDA and IMAWAKI, 2003). At abyssal depths, it is sufficiently distant from the weak deep western boundary current located east of the Izu-Ogasawara Ridge (KAWABE and FUJIO, 2010). Like the MODE area, the observation site is located between a strong current region and the interior.

Figure 1 also shows bottom topography based on ETOPO1 (AMANTE and EAKINS, 2009). The site center is located about 500 km east of the Izu-Ogasawara Ridge. The water depth varies between 6000 and 6300 m within 100 km of the center. The bottom topography is generally flat with small gentle undulations and no apparent large-scale slopes. Exception is several sea-

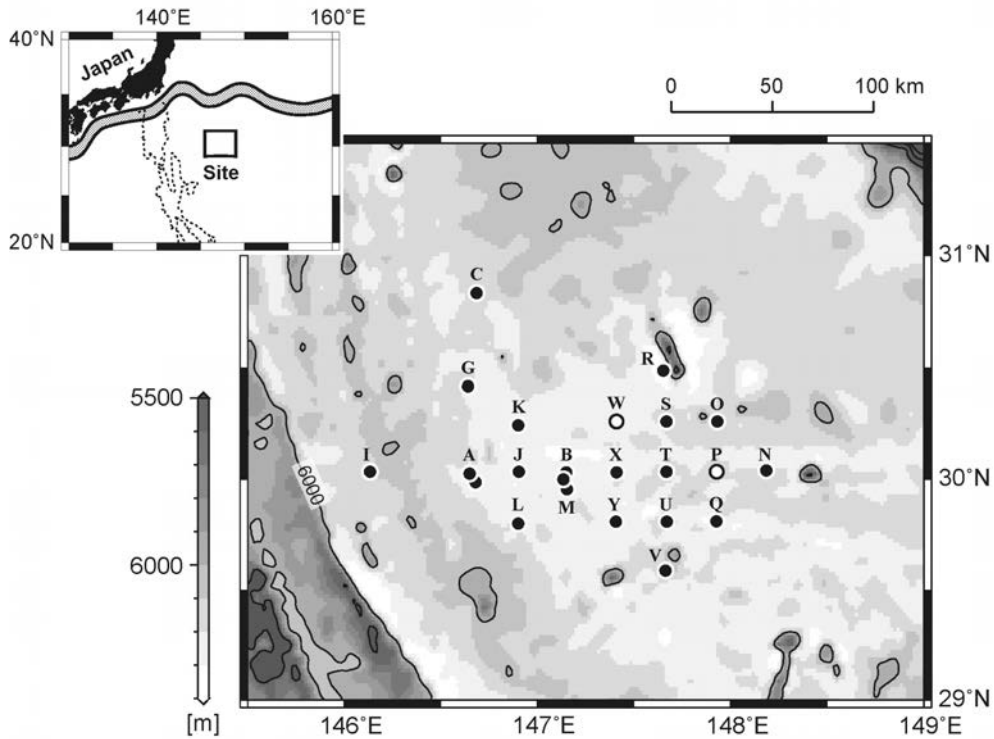


Fig. 1 Location of mooring stations with bottom topography. Dots with station names show locations where current-meter data were obtained; the first “R” of station names is omitted. Two open circles show locations where moorings were deployed but not recovered in Obs. 9. Darker gray indicates shallower depth, with contours of 500 m interval. The rectangle within the small-scale physiographic inset illustrates the location of the present study area relative to both the Kuroshio system, whose mean path during 1993–2000 is shown by shading, and the Izu-Ogasawara Ridge, whose horizontal extent at 3000 m depth is shown by dotted lines.

mounts, for example, a small seamount near Stn. RR, which was not known at the observation time.

Configuration of a used conventional intermediate mooring is shown in Fig. 2 schematically. The mooring line with current-meters inserted was designed to be held vertical in fluctuating flows by both large buoyancy of a glass-sphere cluster at the top and dead weight on the seabed. The mooring was deployed by the so-called “buoy-first/anchor-last” way. It was recovered by releasing an anchor weight through a command from the ship to an acoustic release. When

the mooring line surfaced, a radio-transmitter sent a radio signal to the ship to be located. The mooring technology had been developed by the Buoy Group of Woods Hole Oceanographic Institution (HEINMILLER, 1976) and was transferred to Japan in mid 1970s.

Numbers of current-meters were moored mostly at abyssal depths at various locations in Site R (Fig. 1) repeatedly during 1978 through 1985. Table 1 shows the summary of mooring operations. First moorings were deployed in October 1978. In March 1979, they were recovered and second moorings were deployed on the same

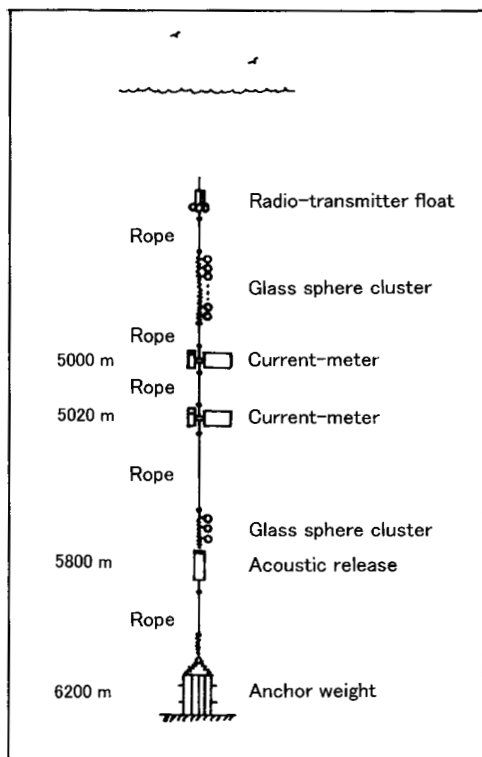


Fig. 2 Schematic view of an intermediate mooring, deployed at 6200 m depth as an example.

cruise. Such recovery and deployment cruises were repeated. Finally, last moorings were recovered in July 1985. As a result, nine mooring observations were performed; they are called Obs. 1 through 9.

Totally 44 moorings were deployed. Thirty-two of them were recovered successfully to provide numbers of good quality records. Two others were recovered without useful records. Ten were not recovered, mostly in Obs. 3, probably because anchor weights made of bundling cut-rails were taken apart during mooring. Therefore, the recovery rate of mooring is 77 % as a whole; it increases to 87 % if Obs. 3 is excluded. Data were not retrieved successfully from 13 current-meters on 12 recovered moorings; they are not listed in Table 1. Totally 50 records are

available. Measurements were restricted mostly to abyssal depths because our mooring technology at that time did not allow us to obtain safe and stable platforms at shallow depths.

Aanderaa RCM-5 current-meters were moored. The current-meter measured current speed by a Savonius rotor and current direction by a magnetic compass, which detected the direction of the instrument body following the fluctuating flow freely. The current-meter recorded current speed, current direction and temperature on a small magnetic tape at an interval of mostly one hour.

After the recovery, the data were linearly interpolated in time, in order to correct possible gain or delay of the inside clock and provide the data every hour on the hour, if recording had continued until the recovery; the discrepancy was typically less than one hour. The reference of flow direction was transferred from the magnetic north to the true north; the magnetic north was located to 2-3° W at the present site. Then noises and doubtful data were removed by eye.

An example of raw data from a nominal depth of 4000 m is shown in Fig. 3 (a). [The current-meter depth is hereafter understood as "nominal."] The velocity record shows very regular oscillations, for example, during year-days -50 to -30; the flow direction changes clockwise quite regularly. The average oscillation period during that part is estimated to be 24.3 h, which is close to the local inertial period (theoretical period of inertial oscillation) at 30° N (23.93 h). Those local inertial oscillations are ubiquitous in velocity records obtained. Temperature data are not used in the present study.

In the raw data, diurnal and semi-diurnal tidal fluctuations are apparent as well as inertial oscillations. Those high-frequency fluctuations in the eastward (u) and northward (v) velocity-components are filtered out by Godin filter (GODIN,

Table 1. Summary of mooring observations at Site R during 1978–1985. Listed are 32 successfully recovered moorings with at least one current-meter providing a good quality record. The time coordinate is Japan Standard Time.

Obs. No.	Stn.	Location		Water depth (m)	Nominal depth (m) of current-meter	Deployment Date and Cruise*	Recovery Date and Cruise*	Duration (days)
		Lat. (N)	Long. (E)					
1	RA	29° 59.2'	146° 40.7'	6210	4000, 5000	1 Oct. 1978 H	17 Mar. 1979 H	167
	RB	30° 00.1'	147° 08.6'	6240	4000, 5000	2 Oct. 1978 H	19 Mar. 1979 H	168
	RC	30° 49.8'	146° 41.1'	6180	4000, 5000	2 Oct. 1978 H	17 Mar. 1979 H	166
2	RB	29° 59.9'	147° 07.6'	6220	4000, 4500, 5000, 5180	19 Mar. 1979 H	21 Nov. 1979 T	247
	RC	30° 49.3'	146° 41.6'	6170	4000	17 Mar. 1979 H	21 Nov. 1979 T	249
3	RB	29° 56.4'	147° 08.2'	6210	4000	21 Nov. 1979 T	23 Aug. 1980 T	276
4	RA	30° 01.8'	146° 38.2'	6210	650, 1500, 3000, 5000	28 Sept. 1980 H	19 July 1981 T	294
	RB	29° 54.8'	147° 08.3'	6220	5000	24 Aug. 1980 T	19 July 1981 T	329
	RG	30° 25.0'	146° 38.4'	6180	5000	25 Aug. 1980 T	19 July 1981 T	327
	RI	30° 02.2'	146° 07.3'	6110	5000	25 Aug. 1980 T	18 July 1981 T	327
5	RB	30° 02.0'	147° 09.0'	6260	4980, 5000	19 July 1981 T	18 July 1982 B	364
	RI	30° 01.7'	146° 07.5'	6090	5000	20 July 1981 T	17 July 1982 B	362
6	RB	30° 02.1'	147° 09.0'	6250	5000	18 July 1982 B	15 May 1983 H	301
	RI	30° 02.8'	146° 07.9'	6070	5000	19 July 1982 B	13 May 1983 H	298
7	RA	30° 01.1'	146° 39.4'	6230	4000, 4020	14 May 1983 H	25 Oct. 1983 B	164
	RB	30° 00.5'	147° 09.1'	6250	4000, 5000	15 May 1983 H	25 Oct. 1983 B	163
	RJ	30° 02.0'	146° 54.1'	6260	4000, 4020	14 May 1983 H	25 Oct. 1983 B	164
	RK	30° 14.6'	146° 54.0'	6210	4000	15 May 1983 H	24 Oct. 1983 B	162
	RL	29° 48.0'	146° 54.0'	6150	4000, 4020	14 May 1983 H	27 Oct. 1983 B	166
8	RB	30° 02.4'	147° 09.1'	6250	5000	25 Oct. 1983 B	2 July 1984 B	251
	RM	29° 57.3'	147° 09.1'	6210	5000	27 Oct. 1983 B	2 July 1984 B	249
9	RB	30° 01.9'	147° 08.9'	6260	5000	3 July 1984 B	1 July 1985 B	363
	RN	30° 02.4'	148° 11.0'	6200	4000	5 July 1984 B	4 July 1985 B	364
	RO	30° 15.6'	147° 55.8'	6180	4000	7 July 1984 B	2 July 1985 B	360
	RQ	29° 48.6'	147° 55.5'	6230	4000	5 July 1984 B	4 July 1985 B	364
	RR	30° 29.1'	147° 39.0'	6320	4100, 4120	7 July 1984 B	2 July 1985 B	360
	RS	30° 15.6'	147° 40.0'	6180	4000, 4020	7 July 1984 B	2 July 1985 B	360
	RT	30° 02.0'	147° 40.0'	6160	4000	6 July 1984 B	3 July 1985 B	362
	RU	29° 48.5'	147° 40.1'	6160	4000, 4020	4 July 1984 B	3 July 1985 B	364
	RV	29° 35.2'	147° 39.7'	6200	4020	4 July 1984 B	3 July 1985 B	364
	RX	30° 01.9'	147° 24.5'	6250	4000	3 July 1984 B	1 July 1985 B	363
RY	29° 48.5'	147° 24.3'	6210	4000, 4020	4 July 1984 B	1 July 1985 B	362	

* H: *Hakuho Maru*, T: *Tokaidai-gaku Maru II*, B: *Bosei Maru II*.

1972) for analyses on the low-frequency fluctuations. Figure 4 shows the shape of Godin filter and its power gain. The shape comes from taking running-means of hourly data three times over 24, 24 and 25 data repeatedly; the filter consists of 71 terms. Therefore, the filter guarantees almost complete removal of diurnal and semi-diurnal tidal fluctuations, although the response

with half power gain at 3.9 days is not satisfactorily sharp. The inertial period at the present site varies between 23.34 h (Stn. RC) and 24.24 h (Stn. RV), and therefore, Godin filter can remove inertial oscillations effectively as well. Figure 3 (b) shows low-pass-filtered data of the raw data shown in Fig. 3 (a).

After the high-frequency fluctuations are fil-

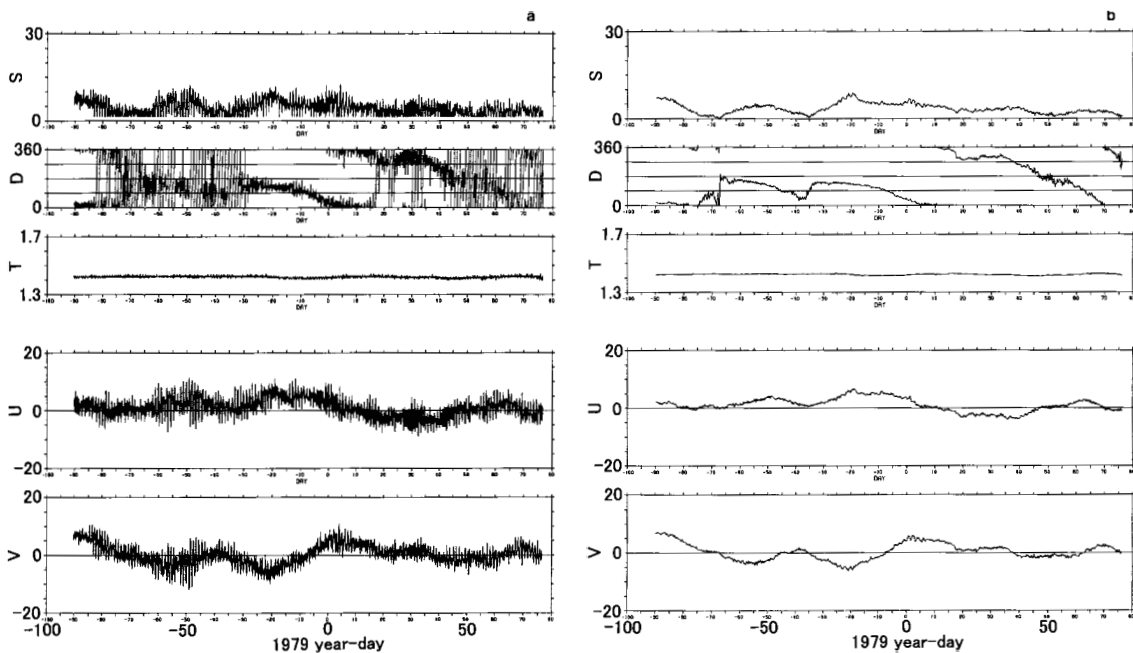


Fig. 3 Time series of velocity and temperature observed at 4000 m depth at Stn. RA during Obs. 1. Panel (a) is the raw data sampled at 30-minute interval and (b) their low-pass-filtered data. From top to bottom in each panel, current speed (S ; cm s^{-1}), current direction (D ; degrees, clockwise from the true north), temperature (T ; degrees Celsius), eastward velocity-component (U ; cm s^{-1}) and northward one (V ; cm s^{-1}) are shown. The abscissa is time in year-day of 1979, or the serial day from 1 January 1979.

tered out, data are subsampled at midnight of Japan Standard Time to provide the daily data. The aliasing due to fluctuations with periods between one and two days is small because the response of the filter is not sharp. The measurement error of these low-pass-filtered data is estimated to be 0.43 cm s^{-1} for both u and v components, from standard deviations of differences between two sets of velocity data obtained at almost same depths (only 20 m apart vertically) near 4000 or 5000 m depth on the same mooring lines at eight stations (Table 2). For those pairs of data sets, the raw data are also almost identical with each other.

3. General statistics and combining records

Table 2 shows the general statistics of all the

50 records obtained at 19 stations (Fig. 1). All calculations are done for the low-pass-filtered daily velocities. Statistics for Obs. 1 have already been reported (IMAWAKI, 1985). At abyssal depths (at 4000 m or deeper), the mean flow is weak and therefore, the kinetic energy per unit mass for the mean flow, or mean kinetic energy (K_M) is small; it varies between 0.1 and $5.6 \text{ cm}^2 \text{ s}^{-2}$. The kinetic energy per unit mass for meso-scale eddies, or eddy kinetic energy (K_E) varies between 5 and $24 \text{ cm}^2 \text{ s}^{-2}$; it is an order of magnitude larger than the K_M . This indicates that the site is located in the mid-ocean.

Time-space averages of those individual statistics at abyssal depths are calculated with weight of measurement duration and listed at the bottom of Table 2. The present 47 records at abys-

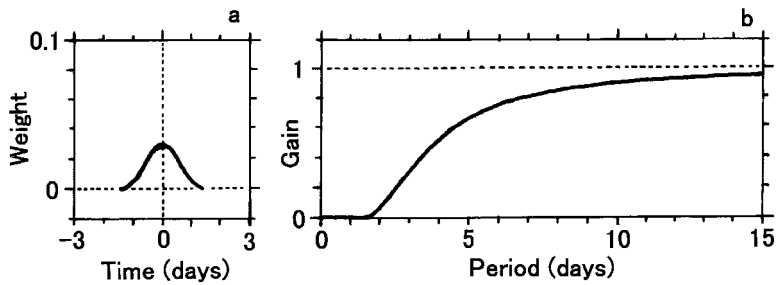


Fig. 4 Godin filter. Panel (a) shows the distribution of weights to be put on 71 hourly data. Panel (b) shows the square of filter response factor as a function of fluctuation period.

sal depths provide the sum of 11,660 day (32 year) data. Records obtained at several depths at the same station may not be independent from each other for the low-frequency fluctuations and therefore, incomplete records are excluded first, if any, and then remaining complete records are weighted to represent one record at that station, except for Stn. RY, where the longer record is chosen. The data used for calculation of averages are totally 8830 day (24 year) data, and therefore, those statistics are considered to be representative values at the present site. The time-space average u and v components (-0.29 and 0.71 cm s^{-1} , respectively) are small. The average zonal and meridional variances (10 and $11 \text{ cm}^2 \text{ s}^{-2}$, respectively) are almost equal to each other. The K_E ($11 \text{ cm}^2 \text{ s}^{-2}$) is about 40 times larger than the K_M ($0.3 \text{ cm}^2 \text{ s}^{-2}$). Note that the K_M listed in the table is calculated from the average u and v components; the average of individual K_M 's is $1.5 \text{ cm}^2 \text{ s}^{-2}$.

For shallower flow field, three records were obtained at 650, 1500 and 3000 m depths at Stn. RA during Obs. 4. The record at 3000 m depth shows very similar features to those at 5000 m depth, in the time series of low-pass-filtered velocity and the general statistics. The record at 1500 m depth is too short to discuss mesoscale eddies but the hourly raw data shows an inter-

esting phenomenon of unusually long-lived inertial oscillation. The flow direction continues to change clockwise quite regularly for more than 40 days without any major disturbances or interruption (not shown here). The average oscillation period is estimated to be 22.8 h (41.8 days for 44 cycles), which is a little shorter than the local inertial period of 23.93 h. The record at 650 m depth shows quite different features; zonal and meridional variances and K_E are several times larger than those at 5000 m depth (Table 2).

At Stn. RB, moored current-meters were maintained continuously during all the nine observations; each mooring was located within 10 km from the mean position. By combining those records, a long continuous record was obtained at 5000 m depth for 2462 days (6.7 years) from October 1978 through June 1985 as shown in Fig. 5. For Obs. 3, no current-meter was moored at 5000 m depth, and it is justifiably made up for by the record at 4000 m depth, because low-pass-filtered daily velocities at those abyssal depths at the same station are similar to each other as shown at beginnings of Sections 4 and 5. At Stn. RC, a continuous record was obtained at 4000 m depth for 411 days from October 1978 through November 1979; each mooring was located within 1 km from the mean position. At Stn. RI, a con-

Table 2. Statistics of low-pass-filtered daily velocities from 50 individual records. Symbol u (v) denotes eastward (northward) velocity-component; overbar denotes temporal average over the record length and prime denotes deviation from it; K_M (K_E) denotes mean (eddy) kinetic energy. Time-space averages of those individual statistics at abyssal depths (see the text) are shown at the bottom.

Obs. No.	Stn.	Depth (m)	First data	Last data	Duration (days)	\bar{u}	\bar{v}	K_M	$\overline{u'^2}$	$\overline{v'^2}$	K_E	$\overline{u'v'}$
						(cm s ⁻¹)	(cm ² s ⁻²)		(cm ² s ⁻²)	(cm ² s ⁻²)		(cm ² s ⁻²)
1	RA	4000	4 Oct. 1978	16 Mar. 1979	164	1.1	0.3	0.6	5.6	7.7	6.6	-2.3
		5000	4 Oct. 1978	3 Mar. 1979	151*	1.2	-0.3	0.8	5.6	8.0	6.8	-2.3
	RB	4000	4 Oct. 1978	18 Mar. 1979	166	0.2	-0.4	0.1	9.0	9.5	9.3	0.4
		5000	4 Oct. 1978	18 Mar. 1979	166	-0.0	-0.4	0.1	7.9	9.2	8.6	-0.2
	RC	4000	5 Oct. 1978	15 Mar. 1979	162	-1.3	2.1	3.0	9.3	14.3	11.8	1.6
		5000	5 Oct. 1978	15 Mar. 1979	162	-1.8	2.0	3.7	9.4	11.8	10.6	1.4
2	RB	4000	22 Mar. 1979	8 Oct. 1979	201*	-0.8	-0.4	0.4	6.9	6.0	6.5	-1.7
		4500	22 Mar. 1979	20 Oct. 1979	213*	-0.3	-0.2	0.1	8.5	6.3	7.4	-0.9
		5000	22 Mar. 1979	20 Nov. 1979	244	-0.3	0.2	0.1	8.5	7.6	8.1	-1.8
		5180	22 Mar. 1979	20 Nov. 1979	244	-0.2	0.3	0.1	8.2	7.6	7.9	-1.9
	RC	4000	19 Mar. 1979	19 Nov. 1979	246	-1.0	-0.2	0.5	13.1	20.1	16.6	-2.6
3	RB	4000	24 Nov. 1979	22 Aug. 1980	273	-0.6	0.6	0.4	5.3	6.8	6.1	-1.0
4	RA	650	1 Oct. 1980	17 July 1981	290	0.0	1.2	0.7	38.6	33.1	35.9	6.8
		1500	8 Nov. 1980	22 Dec. 1980	45*	0.1	0.1	0.0	7.9	1.8	4.8	0.9
		3000	1 Oct. 1980	17 July 1981	290	-0.3	0.4	0.1	4.4	6.5	5.4	-2.0
		5000	1 Oct. 1980	17 July 1981	290	-0.3	-0.6	0.2	4.8	7.8	6.3	-2.5
	RB	5000	26 Aug. 1980	17 July 1981	326	-1.0	0.4	0.5	4.3	6.1	5.2	-1.9
	RG	5000	28 Aug. 1980	16 July 1981	323	-0.7	-0.1	0.2	8.5	15.1	11.8	-2.1
	RI	5000	27 Aug. 1980	17 July 1981	325	-0.9	2.3	3.0	4.3	16.8	10.5	-0.2
5	RB	4980	22 July 1981	23 Oct. 1981	94*	0.7	0.2	0.3	6.2	8.3	7.2	2.5
		5000	22 July 1981	16 July 1982	360	-0.1	1.0	0.5	9.3	9.2	9.3	-2.8
	RI	5000	23 July 1981	15 July 1982	358	-0.3	2.5	3.2	8.2	18.0	13.1	1.7
6	RB	5000	21 July 1982	13 May 1983	297	0.9	1.0	1.0	15.2	9.2	12.2	1.2
	RI	5000	22 July 1982	12 May 1983	295	-0.7	2.9	4.3	4.0	5.5	4.8	-2.2
7	RA	4000	17 May 1983	23 Oct. 1983	160	-0.8	-1.1	0.9	11.6	5.4	8.5	2.1
		4020	17 May 1983	23 Oct. 1983	160	-0.9	-1.4	1.3	14.1	7.3	10.7	1.4
		4000	17 May 1983	24 Oct. 1983	161	-0.8	1.3	1.2	11.7	7.8	9.7	3.9
	RB	4000	17 May 1983	24 Oct. 1983	161	-0.5	0.9	0.5	12.3	8.3	10.3	4.5
		5000	17 May 1983	24 Oct. 1983	161	-0.7	0.1	0.3	9.9	6.3	8.1	3.2
	RJ	4000	17 May 1983	23 Oct. 1983	160	-0.7	0.1	0.3	9.9	6.3	8.1	3.2
		4020	17 May 1983	23 Oct. 1983	160	-0.6	0.0	0.2	11.2	5.1	8.2	1.7
	RK	4000	18 May 1983	23 Oct. 1983	159	-1.1	0.2	0.6	13.3	7.0	10.2	0.2
	RL	4000	17 May 1983	25 Oct. 1983	162	-0.3	-0.6	0.2	10.6	6.5	8.6	2.8
4020	17 May 1983	25 Oct. 1983	162	-0.4	-0.4	0.1	8.9	5.5	7.2	2.9		
8	RB	5000	28 Oct. 1983	1 July 1984	248	-0.1	1.2	0.7	9.7	6.2	8.0	-3.3
	RM	5000	30 Oct. 1983	1 July 1984	246	0.2	0.9	0.5	7.2	5.0	6.1	-1.5
9	RB	5000	6 July 1984	30 June 1985	360	0.4	1.0	0.6	12.7	12.0	12.4	-2.9
	RN	4000	8 July 1984	2 July 1985	360	-1.0	-0.3	0.5	12.4	10.0	11.2	-0.8
	RO	4000	9 July 1984	1 July 1985	358	1.8	0.1	1.6	15.9	17.3	16.6	-3.2
	RQ	4000	8 July 1984	2 July 1985	360	-2.3	0.2	2.6	9.1	9.4	9.3	-1.5
	RR	4100	10 July 1984	1 July 1985	357	2.9	-0.1	4.1	6.7	23.4	15.1	-4.8
		4120	10 July 1984	1 July 1985	357	2.8	0.2	3.9	7.4	21.5	14.4	-6.1
	RS	4000	10 July 1984	30 June 1985	356	2.5	0.8	3.4	19.1	21.5	20.3	-4.3
		4020	10 July 1984	2 Apr. 1985	267*	3.3	0.7	5.6	22.2	25.5	23.9	-6.5
	RT	4000	9 July 1984	1 July 1985	358	-0.7	1.2	0.9	14.3	13.4	13.9	-2.2

RU	4000	7 July 1984	1 July 1985	360	-2.0	0.6	2.2	10.4	10.6	10.5	-0.6
	4020	7 July 1984	19 Oct. 1984	105*	-2.8	1.5	5.1	14.3	3.3	8.8	0.9
RV	4020	7 July 1984	18 Nov. 1984	135*	-3.0	0.7	4.7	11.4	2.2	6.8	-0.4
RX	4000	6 July 1984	7 June 1985	337*	-0.3	1.4	1.0	14.9	13.0	14.0	-0.5
RY	4000	6 July 1984	7 June 1985	337*	-1.4	0.9	1.4	12.0	9.1	10.5	-1.2
	4020	6 July 1984	16 Mar. 1985	254*	-1.3	0.8	1.1	11.9	11.2	11.6	-0.9
Time-space average					-0.29	0.71	0.29	10.19	11.37	10.79	-1.32

* Incomplete record which stopped before recovery due to battery trouble or instrumental failure

Table 3. Summary and statistics of long continuous records obtained by combining successive records. See Table 2 for notations.

Stn.	Mean location		Water depth (m)	Meter depth (m)	First deployment	Last recovery	Obs. No.	Duration (days)
	Lat. (N)	Long. (E)						
RB	30° 00'	147° 08'	6240	5000*	2 Oct. 1978	1 July 1985	1 - 9	2464
RC	30° 50'	146° 41'	6170	4000	2 Oct. 1978	21 Nov. 1979	1, 2	415
RI	30° 02'	146° 08'	6090	5000	25 Aug. 1980	13 May 1983	4 - 6	992

Stn.	Meter depth (m)	First data	Last data	Duration (days)	\bar{u}	\bar{v}	K_M	$\overline{u'^2}$	$\overline{v'^2}$	K_E	$\overline{u'v'}$
					(cm s ⁻¹)	(cm ² s ⁻²)		(cm ² s ⁻²)	(cm ² s ⁻²)		
RB	5000*	4 Oct. 1978	30 June 1985	2462	-0.12	0.72	0.27	9.8	8.5	9.2	-1.2
RC	4000	5 Oct. 1978	19 Nov. 1979	411	-1.06	0.73	0.83	11.6	18.9	15.3	-1.1
RI	5000	27 Aug. 1980	12 May 1983	989	-0.66	2.53	3.42	5.8	14.0	9.9	-0.2

* For Obs. 3, velocities at 4000 m depth are used instead of 5000 m (see the text).

tinuous record was obtained at 5000 m depth for 989 days (2.7 years) from August 1980 through May 1983; each mooring was located within 2 km from the mean position. Table 3 shows the statistics of the three records. A part of the present time series of daily velocity has already been published (IMAWAKI and TAKANO, 1982; MIYAMOTO *et al.*, 2017).

4. Mean flows

Differences of mean velocities between 4000 and 5000 m depths at the same station are small in five available comparison cases at Stns. RA, RB and RC (Table 2); standard deviations of differences of mean u and v components between the two depths are both 0.40 cm s⁻¹, which is the same level as the estimated measurement error (Section 2). That is to say mean velocities at

abyssal depths at the same station are similar to each other.

Figure 6 shows horizontal distribution of mean velocities at abyssal depths. A striking feature is the large anticyclonic vortex observed during Obs. 9 at 11 stations east of Stn. RB. This steady vortex, however, is beyond the scope of the present paper and described on a separate paper (IMAWAKI and TAKANO, 2019). The mean v component at Stn. RI (2.5 cm s⁻¹) is remarkably large. It comes from a stable mean flow toward north-northwest; means of v component during Obs. 4, 5 and 6 are 2.3, 2.5 and 2.9 cm s⁻¹, respectively (Table 2).

At Stn. RB, nine observations were carried out continuously (Table 1 and Fig. 5). The mean velocity during each observation is shown in Fig. 7. Those mean velocities are weak and their maxi-

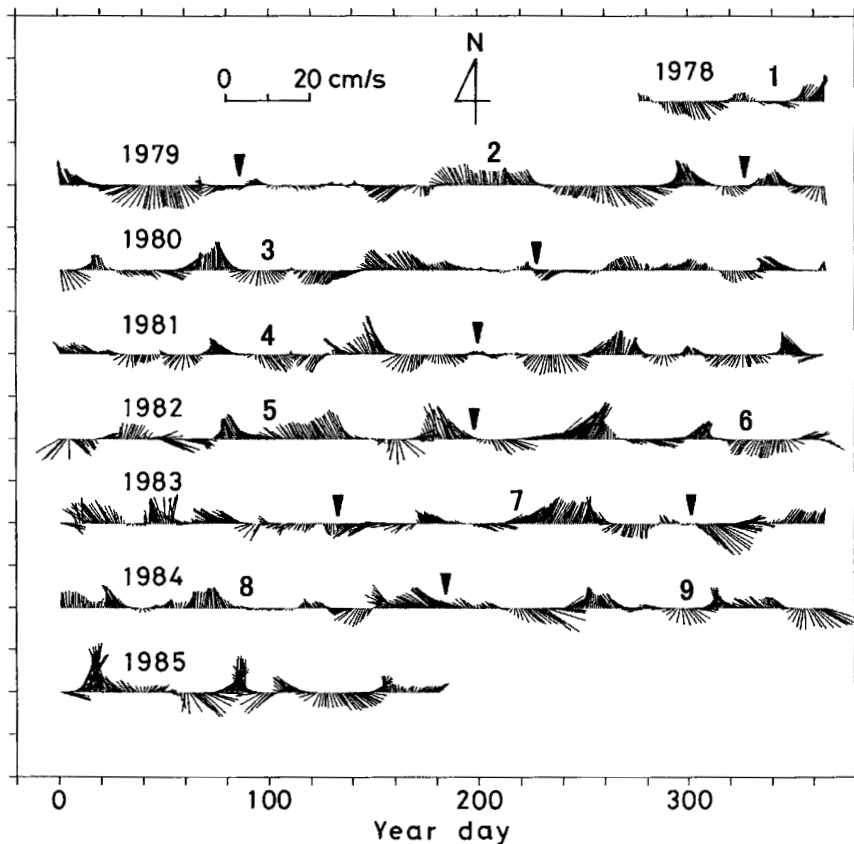


Fig. 5 Time series of low-pass-filtered daily velocity obtained at 5000 m depth at Stn. RB from 4 October 1978 through 30 June 1985. For Obs. 3, velocities at 4000 m depth are used. Each stick represents a daily velocity vector (upward north). The abscissa is time in year-day. Arrowheads indicate exchange of moorings. Numerals indicate observation numbers.

mum speed is only 1.4 cm s^{-1} during Obs. 6. Their v components are positive, except during Obs. 1. Their combined record shows followings (Table 3). The overall mean velocity during seven years is less than 1 cm s^{-1} in speed and directed to the north; the mean u (v) component is -0.12 (0.72) cm s^{-1} (Fig. 7). The K_M ($0.3 \text{ cm}^2 \text{ s}^{-2}$) is very small. Those statistics are quite similar to the time-space averages of all individual statistics at abyssal depths (Table 2).

Errors of those estimated mean u and v components due to low-frequency fluctuations are

evaluated at the 95 % confidence level, following ZENK and MÜLLER (1988) and TALLEY *et al.* (2011), as follows. The standard error S_e is given by $\sigma_0 / \sqrt{N_d}$, where σ_0 is the standard deviation of the original time series and N_d the degrees of freedom. The degrees of freedom is given by T_r / τ_i , where T_r is the record length and τ_i the integral timescale estimated approximately by integrating the autocorrelation function until its first zero-crossing. Assuming normal distribution, the error ε of the estimated mean at the 95 % confidence level is given by $t_s S_e$, where t_s ,

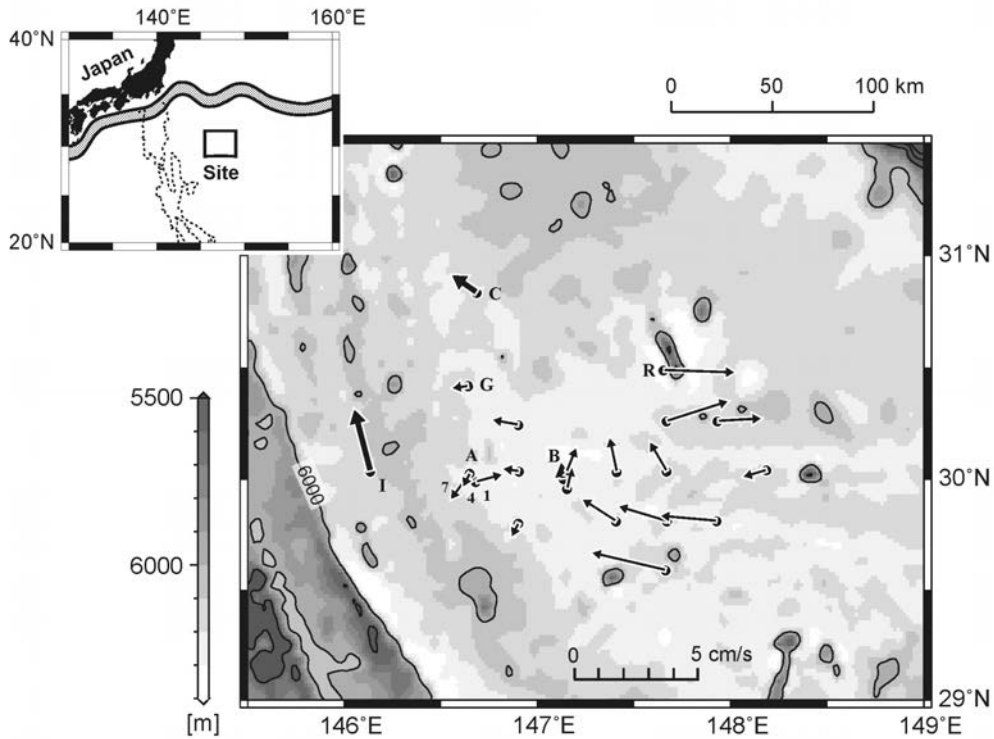


Fig. 6 Horizontal distribution of mean velocities at abyssal depths during individual observations (thin arrows; Table 2) and those from three combined records (thick arrows; Table 3). Velocities at 4000 m depth are shown, except 5000 m depth velocities at Stns. RB, RG and RI, and for Obs. 4 at Stn. RA. Three arrows at Stn. RA are for Obs. 1, 4 and 7. At Stn. RB, the mean velocity during Obs. 9 is shown as well as that from the combined record. Selected station names are shown with the first “R” omitted. Darker gray indicates shallower depth, with contours of 500 m interval.

the Student’s t -variable is about 2.0 when the degrees of freedom is larger than 27. Those properties for the present combined record at Stn. RB are shown in Table 4. The mean v component ($0.72 \pm 0.35 \text{ cm s}^{-1}$) is positive significantly, while the mean u component ($-0.12 \pm 0.44 \text{ cm s}^{-1}$) is not significantly different from zero. Estimated means also include the measurement error, which is not discussed here.

It is interesting to examine how a shorter-term “mean” fluctuates around a long-term mean, which is regarded to be closer to the true mean, and how it converges with increasing data

used, on real data. The present seven-year long data can provide many “means” estimated for shorter durations. For example, “means” for 200 days can be estimated in 12 independent cases; the “mean” u (v) components vary between -1.6 and 2.2 cm s^{-1} (-0.4 and 1.7 cm s^{-1}) with standard deviation of 1.0 (0.6) cm s^{-1} . Dependence of standard deviation of those “means” upon the length of data used for estimation is shown in Fig. 8. The figure also shows the standard error S_e as a function of record length. The standard deviation decreases with increasing data length quite similarly to the standard error, al-

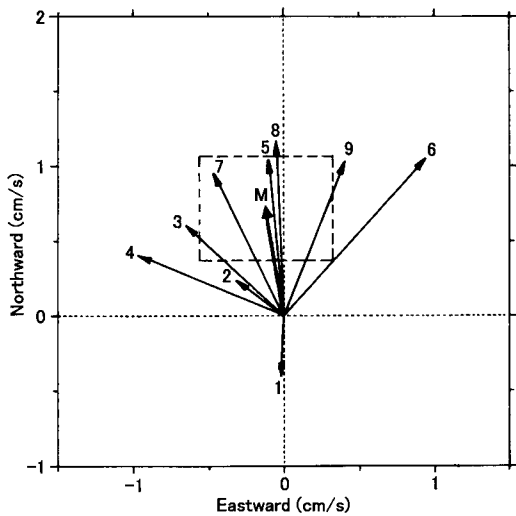


Fig. 7 Mean velocities for nine individual observations at 5000 m depth at Stn. RB. Numerals indicate observation numbers. Also shown is the mean velocity (M) from the long combined record (Fig. 5), with its estimated error at the 95% confidence level (broken line).

though the standard deviation is 1.2 (1.1) times larger than the standard error for the u (v) component, on an average, in the present case.

5. Statistics of mesoscale eddies

In some observations, records at both 4000 and 5000 m depths are available at the same station. Their low-pass-filtered daily velocities are very similar to each other and no significant dif-

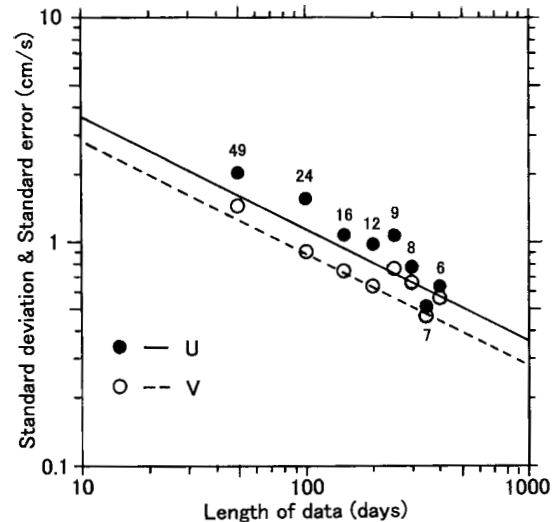


Fig. 8 Dependence of standard deviation of “means” upon the length of data used for their estimations. Each numeral is the number of “means” estimated for a certain data length. Two lines show the standard error $S_e [= \sigma_0 \sqrt{(\tau_i / T_r)}$ with σ_0 and τ_i in Table 4] as a function of record length (T_r). Dots and the solid line are for u component, and open circles and the broken line are for v component. The figure is drawn by utilizing the seven-year long record at Stn. RB.

ferences are recognized in their time series (not shown here); their statistics are basically similar to each other (Table 2). It suggests that the velocity field of mesoscale eddies is almost uniform vertically at abyssal depths.

Figure 9 shows K_E 's during individual obser-

Table 4. Estimating errors of mean u and v components for almost seven years at 5000 m depth at Stn. RB.

	u	v
Standard deviation σ_0 (cm s $^{-1}$)	3.1	2.9
Record length T_r (days)	2462	2462
Integral timescale τ_i (days)	12.3	8.7
Degrees of freedom N_d	200	283
Standard error S_e (cm s $^{-1}$)	0.22	0.17
Error on 95% confidence level ϵ (cm s $^{-1}$)	0.44	0.35
Mean (cm s $^{-1}$)	-0.12 ± 0.44	0.72 ± 0.35

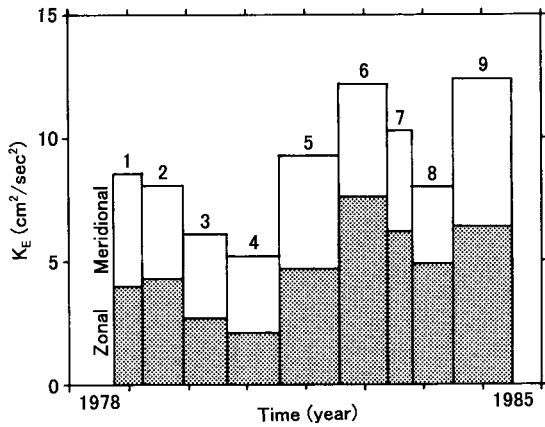


Fig. 9 Eddy kinetic energies during nine individual observations at 5000 m depth at Stn. RB. Numerals indicate observation numbers. Partition of zonal K_E (shaded box) and meridional K_E (blank box) is also shown.

vations at Stn. RB (Fig. 5). Fluctuation of the K_E is large; the maximum K_E ($12.4 \text{ cm}^2 \text{ s}^{-2}$) is more than two times larger than the minimum K_E ($5.2 \text{ cm}^2 \text{ s}^{-2}$). The figure also shows the partition of zonal and meridional K_E 's. Ratios of meridional to zonal K_E 's vary between 0.6 and 1.4, with a mean of 0.9. The long combined record at Stn. RB (Fig. 5 and Table 3) shows followings. The flow direction of daily velocity changes mostly counterclockwise. The zonal variance ($10 \text{ cm}^2 \text{ s}^{-2}$) is similar to the meridional variance ($9 \text{ cm}^2 \text{ s}^{-2}$). The K_E ($9.2 \text{ cm}^2 \text{ s}^{-2}$) is more than 30 times larger than the K_M ($0.3 \text{ cm}^2 \text{ s}^{-2}$). Those statistics are quite similar to the time-space averages of all individual statistics at abyssal depths (Table 2).

For the combined record at Stn. RC (Table 3), the meridional variance ($19 \text{ cm}^2 \text{ s}^{-2}$) is large, which results in large K_E ($15 \text{ cm}^2 \text{ s}^{-2}$). Those two are also large for individual records (Obs. 1 and 2) compared with other stations (Table 2). For the combined record at Stn. RI, the meridional variance ($14 \text{ cm}^2 \text{ s}^{-2}$) is more than two

times larger than the zonal variance ($6 \text{ cm}^2 \text{ s}^{-2}$). At Stn. RR, both two records (separated by 20 m in vertical) show that the meridional variance ($22 \text{ cm}^2 \text{ s}^{-2}$) is three times larger than the zonal variance ($7 \text{ cm}^2 \text{ s}^{-2}$), which is unique in the present statistics. At Stn. RS, both two records (separated by 20 m in vertical) show large K_E 's (20 and $24 \text{ cm}^2 \text{ s}^{-2}$), which are about twice of the overall time-space average (Table 2).

6. Frequency spectra

The seven-year long velocity record at 5000 m depth at Stn. RB (Fig. 5) gives statistically significant estimates of frequency spectra for the eddy kinetic energy (Fig. 10). Zonal and meridional power spectral densities are estimated from energy densities obtained by the fast Fourier transform method and averaged over 10 frequencies. Hence spectra for the zonal and meridional K_E 's are regarded as containing 20 degrees of freedom, and their 95 % confidence limits are from 0.58 to 2.1 times individual estimates. The spectrum for the total K_E is estimated as the sum of those two and therefore, its confidence limits are somewhat narrower than that range.

For convenience, each spectrum is divided into six frequency bands. They are labeled "annual/secular scale," "mesoscale I," "mesoscale II," "mesoscale III," "monthly scale" and "rest." Their period ranges and K_E 's contained in those bands are shown in Table 5, which also shows ratios of the meridional to zonal K_E 's.

Most of the total K_E (78 %) is contained in the mesoscale I, II and III bands (period range of 31-235 days). Therefore, the three bands as a whole could be called an energy-containing or eddy-containing band (MODE GROUP, 1978). In the whole eddy-containing band, the zonal and meridional K_E 's are equal to each other (both, $3.5 \text{ cm}^2 \text{ s}^{-2}$). In the mesoscale I, the zonal K_E is

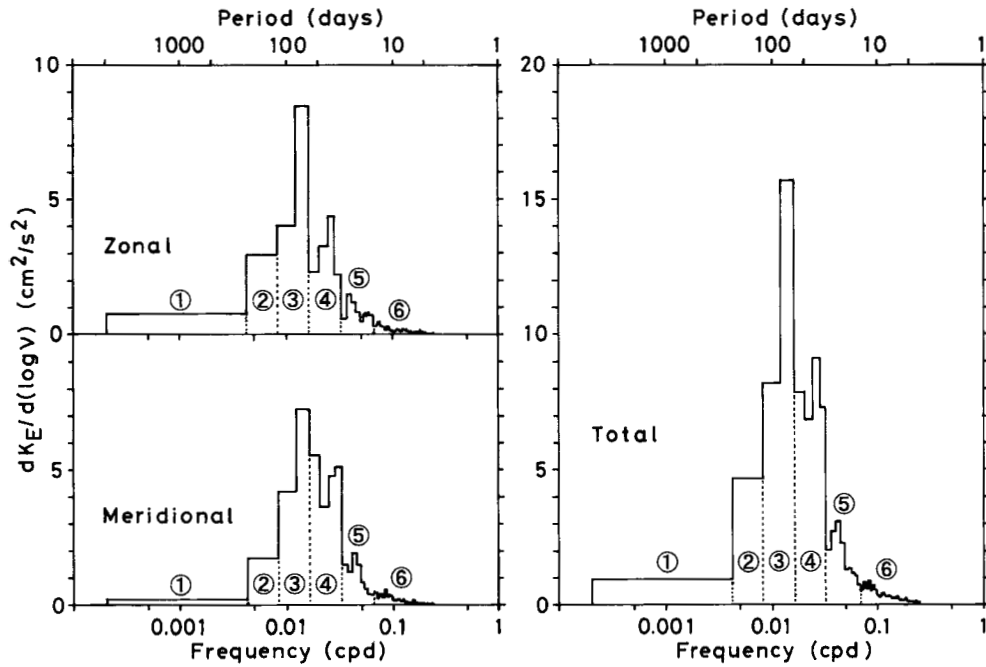


Fig. 10 Frequency spectra of eddy kinetic energy estimated from the seven-year long record at 5000 m depth at Stn. RB (Fig. 5). They are plotted in a variance-preserving form, i.e., an area below the curve represents energy contents in the corresponding frequency range. Symbol ν denotes frequency in cycle per day. Spectra of zonal, meridional and total K_E 's are shown. Each spectrum is divided into six frequency bands, whose ranges are shown by dotted lines and whose reference numbers are indicated by circled numerals. See Table 5 for details.

Table 5. Zonal, meridional and total eddy kinetic energies contained in six frequency bands of the spectra shown in Fig. 10. Also shown are labels of frequency bands, their period ranges, and ratios of meridional to zonal K_E 's. Small discrepancy among numerals is due to rounding lower digits.

Label of frequency band	Period range (days)	Zonal K_E	Meridional K_E	Total K_E	Ratio
		(cm ² s ⁻²)			
1 Annual/secular scale	235 - 4924	1.0	0.2	1.2	0.2
2 Mesoscale I	120 - 235	0.9	0.5	1.4	0.6
3 Mesoscale II	61 - 120	1.7	1.6	3.4	0.9
4 Mesoscale III	31 - 61	0.9	1.4	2.3	1.6
5 Monthly scale	16 - 31	0.3	0.3	0.6	1.3
6 Rest	2 - 16	0.1	0.1	0.2	1.2
Whole	2 - 4924	4.9	4.2	9.2	0.9

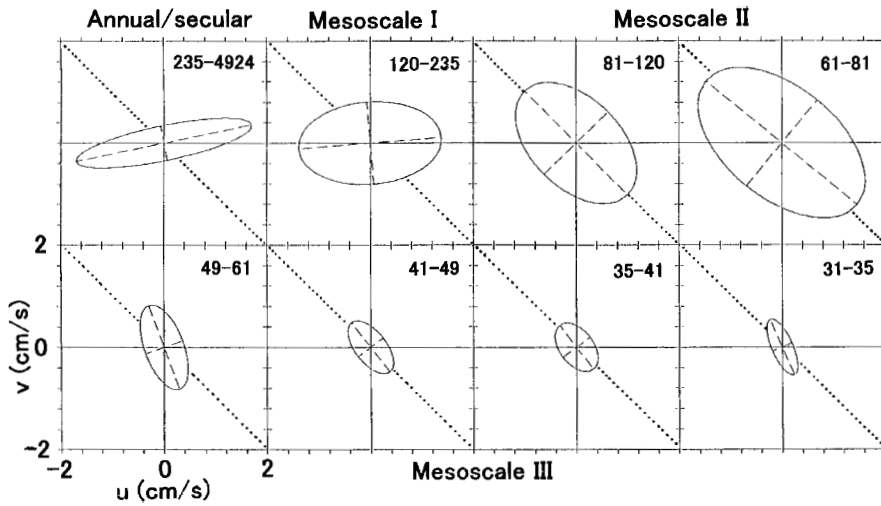


Fig. 11 Current ellipses of lowest eight frequency bands of spectra shown in Fig. 10. Numerals at upper-right corner of each panel show the period range (in days) of that frequency band. Solid lines are u and v axes, dashed lines are major and minor axes, and dotted lines indicate the northwest/southeast direction.

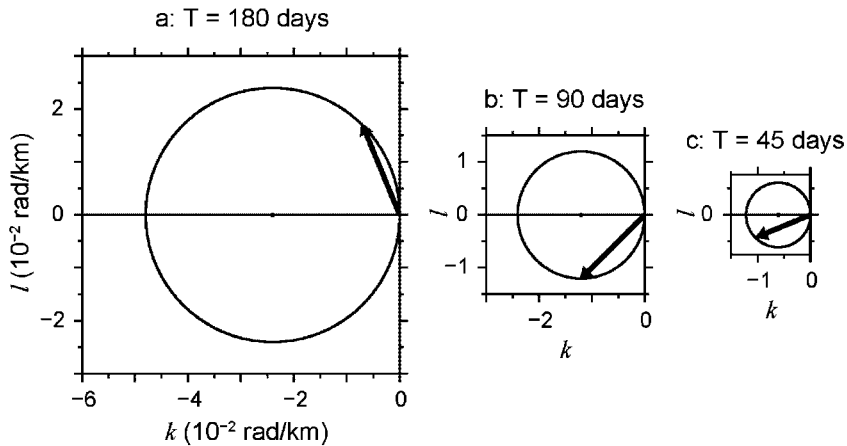


Fig. 12 Conceptual figures of dispersion relation of barotropic Rossby waves (circles) for three periods and selected wavenumber vectors (arrows). Panel (a) is for the period of 180 days and a wavenumber vector directed to the north-northwest with a wavelength of 290 km, (b) for 90 days and the south-west, with 360 km, and (c) for 45 days and the west-southwest, with 570 km. Symbol k (l) denotes the zonal (meridional) wavenumber.

dominant, while in the mesoscale III, the meridional K_E is dominant. In the mesoscale II, they are almost equal to each other. In the annual/

secular scale, the zonal K_E is more than four times larger than the meridional K_E . In the monthly scale, they are almost equal to each oth-

er. In the rest, they are trivially small.

Those spectral features are shown in a different way as current ellipses based on rotary spectrum analysis (Fig. 11). In the annual/secular scale and mesoscale I, the major axis is almost parallel to the u -axis, and zonal fluctuations are dominant. In the mesoscale II (two panels), the major axis is parallel to the northwest/southeast, and zonal and meridional fluctuations are comparable. In the mesoscale III (four lower panels), the major axis is parallel to the north-northwest/south-southeast, and meridional fluctuations are dominant.

Both zonal dominance in the longer-period bands and meridional dominance in the shorter-period band are understood qualitatively by difference in phase propagation direction of fluctuations, if the fluctuations are assumed as plane barotropic Rossby waves having moderate wavelengths of hundreds of kilometers, as pointed out by IMAWAKI and TAKANO (1982). The assumption of plane waves is supported by MIYAMOTO et al. (2019). Figure 12 shows this situation conceptually. The plane Rossby wave of a longer period (Panel a; mesoscale I) is able to have a wavenumber vector (with a moderate magnitude) directed nearly to the north or south; its associated motion is dominantly zonal. On the other hand, the Rossby wave of a shorter period (Panel c; mesoscale III) is able to have a moderate wavenumber vector directed nearly to the west; its associated motion is dominantly meridional. The Rossby wave of a moderate period (Panel b; mesoscale II) is able to have a moderate wavenumber vector directed to the southwest or northwest; its associated motion is of no dominance. The wavelengths shown in Fig. 12 are similar to those estimated by fitting a set of barotropic Rossby waves to fluctuations at several stations in the present site (IMAWAKI, 1985).

7. Vorticity balance

Theoretically, the motion of mid-ocean mesoscale eddies is described as follows. Let x (y) be the eastward (northward) coordinate, and (u, v) the corresponding velocity components. The Rossby number R_o is defined as U/fL , where U is a characteristic horizontal velocity scale, f the Coriolis parameter and L a characteristic horizontal length scale. Taking $U = 10 \text{ cm s}^{-1}$, $f = 10^{-4} \text{ s}^{-1}$ and $L = 100 \text{ km}$, the R_o is 0.01, which is small enough for equations to be developed in an asymptotic series in R_o , providing the quasi-geostrophic regime (PEDLOSKY, 1996) as follows.

Under the Boussinesq approximation and hydrostatic approximation, the quasi-geostrophic field is described as follows. The horizontal velocity \mathbf{v} is expanded as $\mathbf{v} = \mathbf{v}_0 + \mathbf{v}_1 + \dots$, where $\mathbf{v}_0 = (u_0, v_0)$ is the lowest order velocity and \mathbf{v}_1 the first order velocity, being as small as $R_o \mathbf{v}_0$. The lowest order velocity \mathbf{v}_0 is in geostrophic balance and horizontally non-divergent.

$$f_0 \mathbf{k}_U \times \mathbf{v}_0 = -\rho^{-1} \nabla p \quad (1)$$

$$\nabla \cdot \mathbf{v}_0 = 0. \quad (2)$$

Here \mathbf{k}_U is the upward unit-vector perpendicular to the x - y plane, f_0 the Coriolis parameter at the origin, ρ the water density and p the pressure, of the lowest order. The equation for the vertical component of relative vorticity $\zeta = [v_{0x} - u_{0y}]$ of the lowest order is

$$\zeta_t + \mathbf{v}_0 \cdot \nabla \zeta + \beta v_0 + f_0 \nabla \cdot \mathbf{v}_1 = 0. \quad (3)$$

Here notation ϕ_t means time derivative of a scalar property ϕ , and ϕ_x (ϕ_y) means x (y) derivative of ϕ . The parameter β is the meridional gradient of Coriolis parameter at the origin; β is $0.20 \times 10^{-12} \text{ cm}^{-1} \text{ s}^{-1}$ at 30° N . Equation (3) shows that the local time change of relative vorticity is

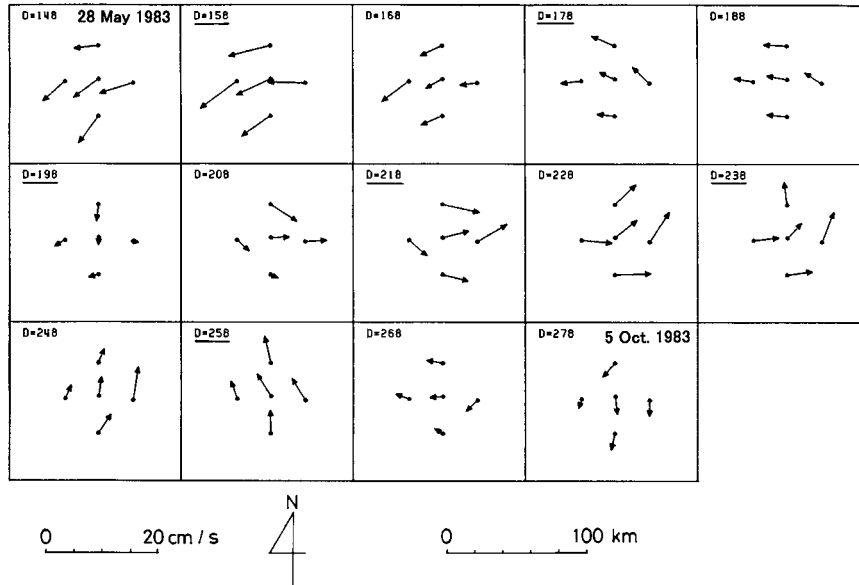


Fig. 13 Sequence of 10-day interval snapshots of 10-day mean velocities at 4000 m depth during Array-83. The year-day of 1983 is shown at the upper-left corner of each panel. On underlined days, vorticity balance is examined.

balanced with the sum of the horizontal advection of relative vorticity, horizontal advection of planetary vorticity (beta-effect) and divergence of the first order horizontal velocity (vertical stretching). If the flow is associated with barotropic planetary Rossby waves, the vorticity equation becomes the linear non-divergent vorticity balance, which is simply

$$\zeta_t + \beta v_0 = 0. \quad (4)$$

On the basis of this theoretical framework, we examine how well the local change of relative vorticity is balanced with the advection of planetary vorticity [Eq. (4)] for actual mesoscale eddies, using the present current-meter data. Observed horizontal velocity \mathbf{V}_{obs} represents mostly the lowest order velocity \mathbf{v}_0 because the first order velocity \mathbf{v}_1 is too small to be distinguished from measurement error. The diver-

gence of observed horizontal velocity $\nabla \cdot \mathbf{V}_{obs}$ estimated by finite difference includes an error due to smaller-scale fluctuations which cannot be resolved by the present observations, as well as the measurement error. It means that the calculated divergence may not be zero, although the divergence should be zero theoretically [Eq. (2)]. Therefore, the value of calculated divergence can be regarded as an error in both measurement and finite differencing (IMAWAKI, 1983).

$$\nabla \cdot \mathbf{V}_{obs} = Error. \quad (5)$$

The first three terms in Eq. (3) can be estimated from observed velocities, but the last term (vertical stretching) cannot be estimated directly.

To examine the vorticity balance, field measurements were carried out twice. The first was a set of five stations in a cross pattern centered at

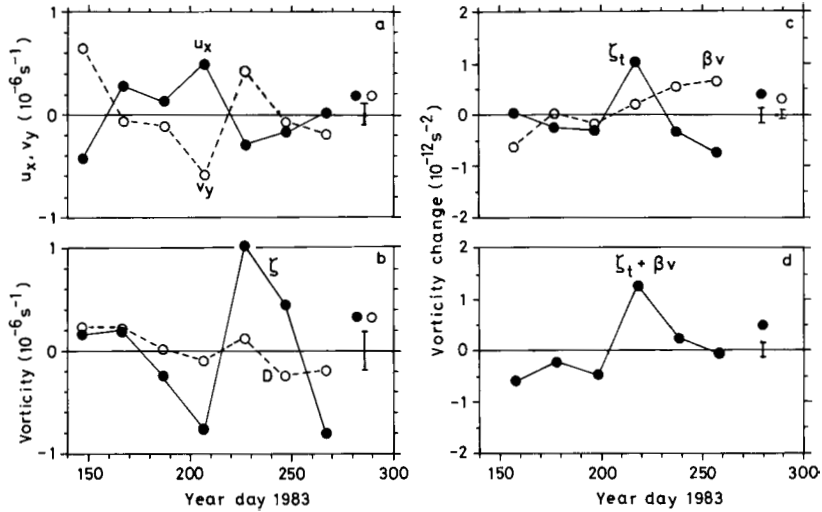


Fig. 14 Time series of various properties concerning the vorticity balance at Stn. RJ during Array-83. Panel (a) is for u_{0x} (dots) and v_{0y} (open circles), (b) for ζ (dots) and calculated horizontal divergence (D ; open circles), (c) for ζ_t (dots) and βv_{0y} (open circles), and (d) for the sum of these two ($\zeta_t + \beta v_{0y}$). In each panel, vertical bars on the right-hand side indicate corresponding estimated errors.

Stn. RJ with zonal and meridional separations of 24 km (Fig. 1). It was carried out from May through October 1983 as Array-83 (Obs. 7). The second was a set of 13 stations in a diamond shape centered at Stn. RT with separations of 25 km. It was carried out from July 1984 through July 1985 as Array-84 (Obs. 9).

7.1 Array-83

Figure 13 shows a sequence of 10-day mean velocities at 4000 m depth during Array-83. Eddies having a speed of 10 cm s^{-1} travel in the site. Figure 14 shows variables concerning the vorticity balance at Stn. RJ, at 20-day interval. Estimated variables are temporally independent from each other because the time interval is much longer than integral timescales of u and v components (Table 4). In this section, all variables are based on 20-day mean velocities; targeted eddies are having temporal scales of more

than several-ten days (periods longer than the mesoscale III). Horizontal derivatives are estimated by finite difference of velocities with a spatial interval of 48 km, in a straightforward manner. Their error is estimated to be $0.09 \times 10^{-6} \text{ s}^{-1}$ from the error (0.3 cm s^{-1}) of u and v components. The station-spacing is fine enough compared with the typical horizontal scale of fluctuations, which is inferred from the lag (70–90 km) of first zero-crossing of transverse correlation function of velocity fluctuations.

After subtracting averages during the array observation, horizontal derivatives u_{0x} and v_{0y} are estimated [Fig. 14 (a)]. They have generally opposite signs and almost equal magnitudes; their correlation coefficient (-0.89) is very high in magnitude, and standard deviations of u_{0x} and v_{0y} are almost the same, suggesting that they are balanced well with each other. Horizontal divergence calculated from the two is shown in

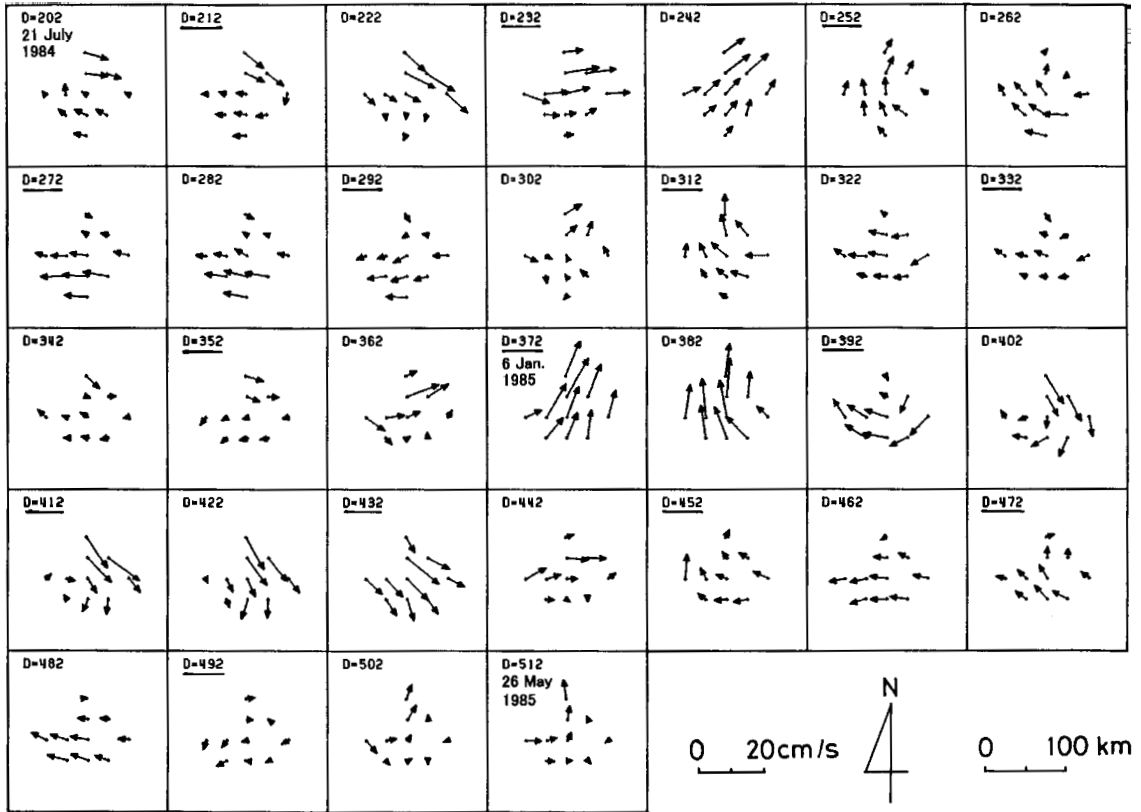


Fig. 15 Same as Fig. 13, but for Array-84 and serial year-day of 1984. At Stns. RB and RR, velocities at 5000 and 4100 m depths, respectively are used.

Fig. 14 (b). As shown in Eq. (5), the calculated divergence is regarded as an error; i.e., its standard deviation ($0.18 \times 10^{-6} \text{ s}^{-1}$) gives the error in addition or subtraction of two similar horizontal derivatives. Figure 14 (b) also shows the estimated relative vorticity ζ . Its standard deviation ($0.61 \times 10^{-6} \text{ s}^{-1}$) is more than three times larger than the estimated error.

The local change of relative vorticity ζ_t is estimated from difference of ζ 's separated by 20 days. The advection of planetary vorticity βv_0 is estimated from the v component at Stn. RJ. Those two are shown in Fig. 14 (c). The standard deviation of βv_0 ($0.43 \times 10^{-12} \text{ s}^{-2}$) is not much different from that of ζ_t ($0.54 \times 10^{-12} \text{ s}^{-2}$),

but their correlation coefficient (-0.27) is rather low. Figure 14 (d) shows the sum of these two, which is the departure from the linear non-divergent vorticity balance [Eq. (4)]. The sum is small in half of six cases (for year-days 178, 238 and 258), being below or close to its estimated error ($0.15 \times 10^{-12} \text{ s}^{-2}$), but large in other cases, especially on year-day 218, for which a large increase of ζ from year-days 208 to 228 cannot be accounted for by βv_0 . The horizontal advection of relative vorticity cannot be estimated from the Array-83 data.

As conclusion of this subsection, the local change of relative vorticity is balanced basically with the advection of planetary vorticity but oc-

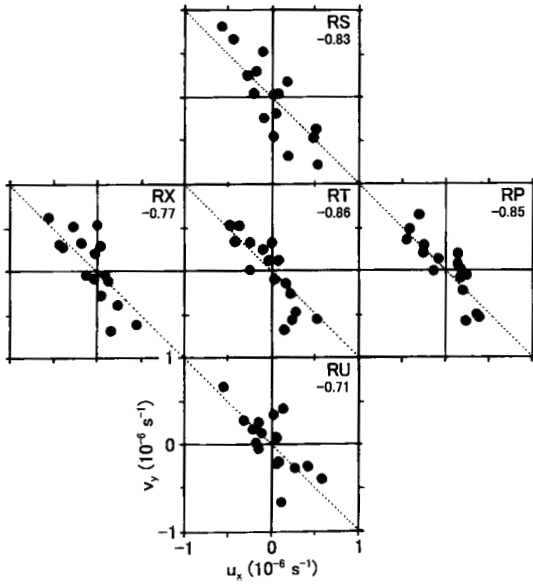


Fig. 16 Scatter plots of u_{0x} versus v_{0y} at five stations, whose names are shown at the upper-right corner of each panel, during Array-84. Numerals below station names are correlation coefficients of 16 cases each. Dotted lines indicate the perfect out-of-phase correlation.

asionally some unknown terms are required to complete the vorticity balance.

7.2 Array-84

Figure 15 shows a sequence of 10-day mean velocities at 4000 m depth during Array-84. The flow is very smooth horizontally and organized well; for example, velocity vectors are like a school of swimming-fish on year-days 242, 372 and 432, and well-organized anticyclonic eddies are seen on year-days 252 and 402. The flow is dominated by anticyclonic patterns. It is because the flow is heavily biased by the steady vortex (Fig. 6) having strong negative vorticity of $-1.1 \times 10^{-6} \text{ s}^{-1}$ at Stn. RT and RP (IMAWAKI and TAKANO, 2019). Time series of daily velocities at all stations show that the flow direction changes mostly counterclockwise (not shown here).

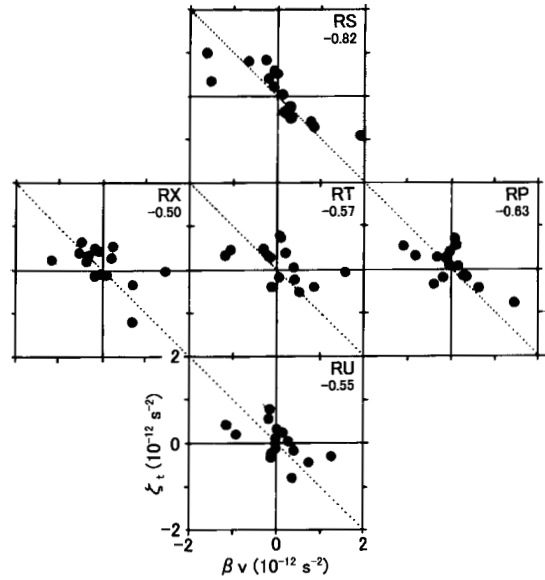


Fig. 17 Same as Fig. 16, but for plots of βv_0 versus ζ_t , and 15 cases.

In the following analysis, missing data at Stn. RP (RW) are filled by averaging data from Stns. RO, RN, RQ and RT (RR and RB). At Stn. RV, data are available only during first 135 days, and so we are forced to use data extrapolated linearly from Stns. RT and RU for the remaining period. At Stns. RX and RY, the usable data stopped before the end of array observation, and so the analysis on vorticity balance is stopped at that time (year-day 525).

After subtracting averages during the array observation, analysis similar to Array-83 is carried out for Stns. RS, RP, RT, RX and RU, using data at five nearby stations separated by 25 km. The results are shown as scatter plots (Figs. 16 and 17). Horizontal derivatives u_{0x} and v_{0y} have generally opposite signs and almost equal magnitudes (Fig. 16). Their correlation coefficients are very high in magnitude at all five stations. For the overall average of 80 cases, the correlation coefficient is -0.80 , and standard deviations of u_{0x} and v_{0y} are similar to each other, suggesting

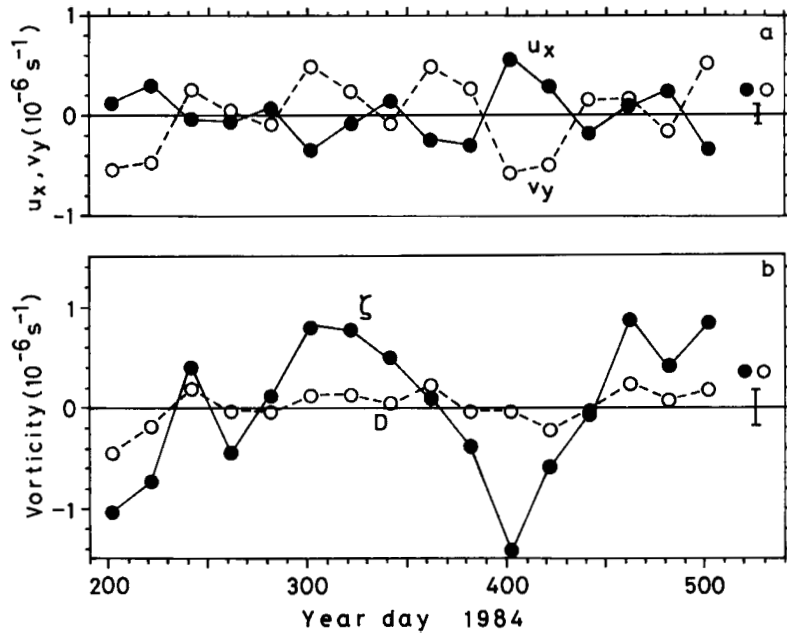


Fig. 18 Time series of properties concerning the vorticity balance at Stn. RT during Array-84. Panel (a) is for u_{0x} (dots) and v_{0y} (open circles), and (b) for ζ (dots) and calculated horizontal divergence (D ; open circles). In each panel, a vertical bar on the right-hand side indicates corresponding estimated error.

that the two variables are balanced very well.

Vorticity balances between the local change of relative vorticity ζ_t and advection of planetary vorticity βv_0 at the five stations are shown in Fig. 17. The two properties have generally opposite signs and almost equal magnitudes. Their correlation coefficients are high at Stn. RS. They are not so high at other stations but significantly different from zero at the 95 % confidence level. The overall correlation coefficient of 75 cases is -0.61 , which is high enough in magnitude to be significantly different from zero at the 95 % confidence level. The overall standard deviation of ζ_t is $0.65 \times 10^{-12} \text{ s}^{-2}$ and that of βv_0 is $0.45 \times 10^{-12} \text{ s}^{-2}$.

The same results as the scatter plot for Stn. RT in Fig. 16 are shown as time series of u_{0x} and v_{0y} in Fig. 18 (a). They have generally opposite

signs and similar magnitudes; their correlation coefficient (-0.86) is very high in magnitude and standard deviations of u_{0x} and v_{0y} are similar to each other, suggesting well-balanced variations. The time series of sum of the two, namely the calculated horizontal divergence is shown in Fig. 18 (b); its standard deviation ($0.18 \times 10^{-6} \text{ s}^{-1}$) gives the error of the relative vorticity ζ and is numerically the same as the corresponding one in Array-83. The standard deviation of ζ ($0.69 \times 10^{-6} \text{ s}^{-1}$) is almost four times larger than the error.

Similarly, the same results as the scatter plot for Stn. RT in Fig. 17 are shown as time series of ζ_t and βv_0 in Fig. 19 (a). Their correlation coefficient (-0.57) is significantly different from zero at the 95 % confidence level as mentioned above. The standard deviation of βv_0 ($0.64 \times 10^{-12} \text{ s}^{-2}$)

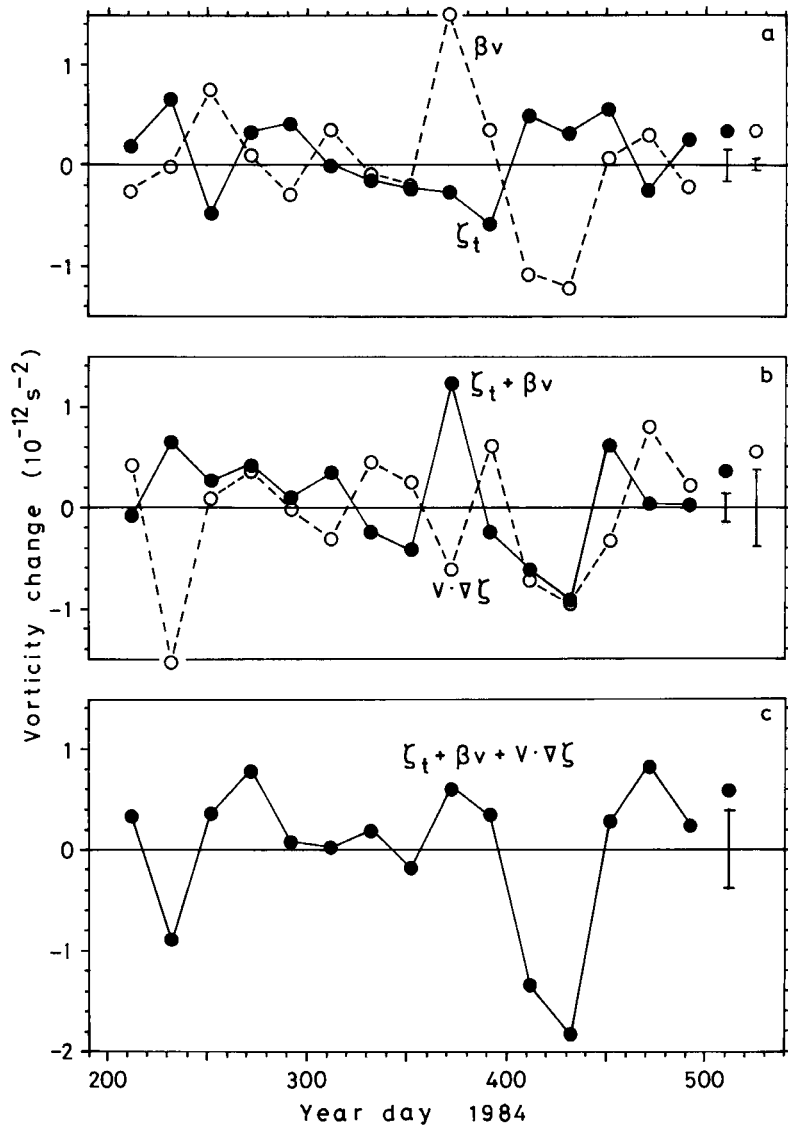


Fig. 19 Time series of various terms of vorticity balance at Stn. RT during Array-84. Panel (a) is for ζ_t (dots) and βv_0 (open circles), (b) for the sum of these two ($\zeta_t + \beta v_0$; dots) and advection of relative vorticity ($\mathbf{v}_0 \cdot \nabla \zeta$; open circles), and (c) for the sum of those three ($\zeta_t + \beta v_0 + \mathbf{v}_0 \cdot \nabla \zeta$). In each panel, vertical bars on the right-hand side indicate corresponding estimated errors.

is larger than that of ζ_t ($0.38 \times 10^{-12} \text{ s}^{-2}$). The sum of these two [Fig. 19 (b)] is small in about half of 15 cases (for year-days 212, 252, 292, 332, 392, 472 and 492), being below or close to its esti-

estimated error ($0.15 \times 10^{-12} \text{ s}^{-2}$), but large on year-days 232, 372, 412, 432 and 452. Especially on year-days 372, 412 and 432, the ζ_t is overbalanced by the large βv_0 .

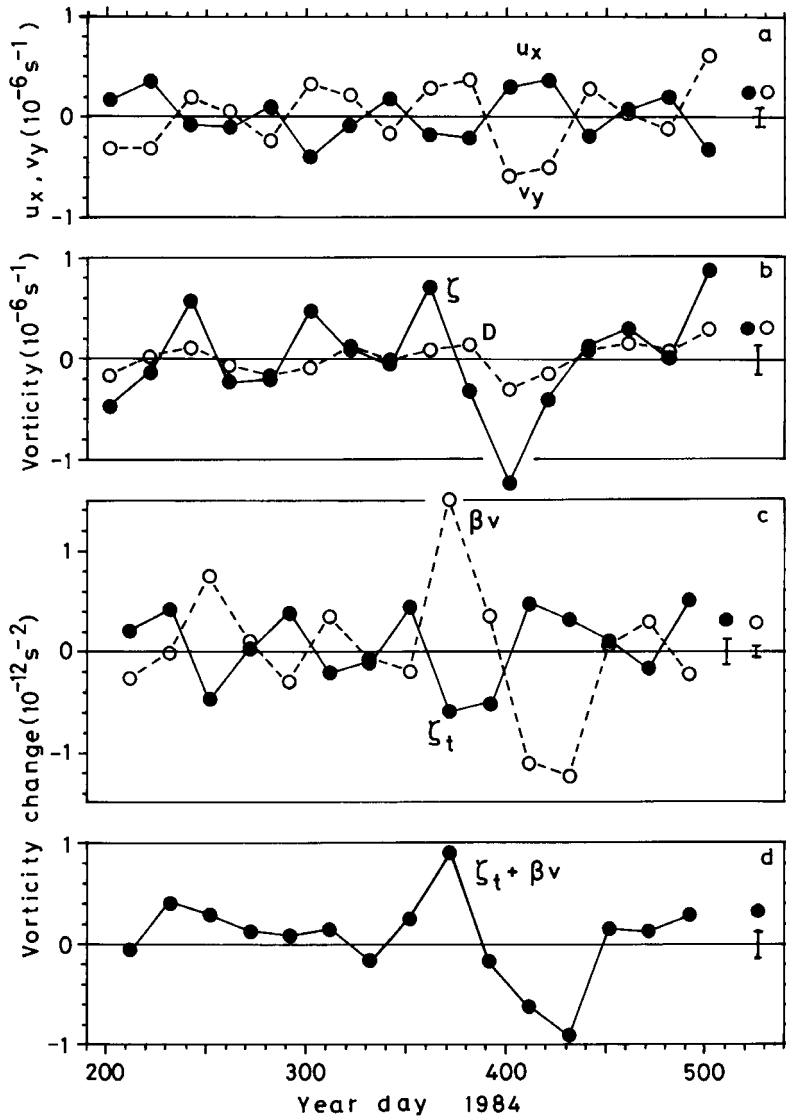


Fig. 20 Same as Fig. 14, but for Stn. RT during Array-84, using data at Stns. RR, RN, RV, RB and RT to examine a larger-scale balance.

Figure 19 (b) also shows the horizontal advection of relative vorticity $\mathbf{v}_O \cdot \nabla \zeta$, estimated from the velocity at Stn. RT and gradient of ζ over Stns. RS, RP, RU and RX. The advection of ζ accounts for the above sum ($\zeta_t + \beta v_\theta$) to some extent in several cases (for year-days 312, 332, 352, 372, 392 and 452), but does not account for

in other cases, having large negatives (for year-days 232, 412 and 432). In short, the horizontal advection of relative vorticity accounts for the imbalance between the local change of relative vorticity and advection of planetary vorticity in some cases, but makes the imbalance worse in other cases.

Finally, the vorticity balance is examined on a larger scale, using data at five stations separated by 50 km, namely Stns. RR, RN, RV, RB and RT. Time series of u_{0x} and v_{0y} at Stn. RT are shown in Fig. 20 (a). They have generally opposite signs and almost equal magnitudes; their correlation coefficient (-0.92) is very high in magnitude and standard deviations of u_{0x} and v_{0y} are almost the same. Figure 20 (b) shows the horizontal divergence calculated from the two and ζ ; the standard deviation of ζ ($0.50 \times 10^{-6} \text{ s}^{-1}$) is much larger than that of horizontal divergence ($0.15 \times 10^{-6} \text{ s}^{-1}$), which gives the error of ζ . The βv_0 (the same as the smaller scale) and ζ_t are shown in Fig. 20 (c). Their correlation coefficient (-0.80) is much higher in magnitude than the smaller scale. The standard deviation of βv_0 is larger than that of ζ_t ($0.37 \times 10^{-12} \text{ s}^{-2}$). The sum of these two [Fig. 20 (d)] is small in about half of 15 cases but large on year-days 372, 412 and 432, where ζ_t is again over-balanced by the large βv_0 . The relation between the two is a little better on the larger scale than smaller scale.

As conclusion of this subsection, the local change of relative vorticity is balanced basically with the advection of planetary vorticity on both smaller and larger scales. In some cases, the horizontal advection of relative vorticity accounts for the imbalance between the two, but makes it worse in other cases; the vorticity balance of mesoscale eddies has not yet been completed.

8. Discussions

Records at 5000 m depth at Stn. RI show a stable north-northwestward flow. The station is located at 40 km east of Stn. TA ($30^\circ 00'N$, $145^\circ 45'E$), where a strong south-southeastward mean flow along local isobaths was observed during 1978–1982, with bottomward intensification, namely the speed increase from 3.2 cm s^{-1} at

4000 m depth to 7.2 cm s^{-1} at 5800 m depth (50 m above the bottom) (Keisuke Taira, personal communication; Miyamoto et al., 2019). The stable flow at Stn. RI might be a part of the local circulation associated with this strong flow at Stn. TA.

Records at 4100 m depth level at Stn. RR show unique dominance of the meridional variance over zonal variance. As shown in Fig. 1, the station is located at the foot of western slope of the seamount, which rises from 6300 m deep bottom up to 5400 m depth. The meridional dominance is probably due to preference of fluctuating flows along local isobaths, although a remarkable mean flow associated with the steady vortex is directed to the seamount (Fig. 6). This local dominance of meridional variance could disturb the examination of vorticity balance but the possible distortion is not apparent in the Array-84 analysis.

A long velocity record for almost seven years was obtained at 5000 m depth at Stn. RB. This is probably one of the longest continuous records from moored current-meters at depth in the mid-ocean over the world, together with a similar long record at 1000 m depth in the eastern North Atlantic, where moorings were maintained during 1980–1986 (ZENK and MÜLLER, 1988). The mean v component (0.72 cm s^{-1}) at 5000 m depth at Stn. RB is almost exactly equal to that of time-space average (0.71 cm s^{-1}) of statistics of all records at abyssal depths in the present site, the mean u component of the former (-0.12 cm s^{-1}) is close to that of the latter (-0.29 cm s^{-1}), and the K_E of the former ($9.2 \text{ cm}^2 \text{ s}^{-2}$) is similar to that of the latter ($10.8 \text{ cm}^2 \text{ s}^{-2}$), suggesting that the record at Stn. RB represents the flow field at the present site quite well. On the other hand, the mean velocity at Stn. RB might be under the effect of the local steady vortex (Fig. 6; IMAWAKI and TAKANO, 2019). Therefore, it

is hard to definitely judge its representativeness of the site.

The eddy kinetic energy is compared with other locations. The level of K_E at the present site ($11 \text{ cm}^2 \text{ s}^{-2}$) is comparable with that ($12 \text{ cm}^2 \text{ s}^{-2}$) at 4000 m depth at similar latitudes along 152° E (SCHMITZ, 1984). The present level is higher than that in the central North Pacific (TAFT *et al.*, 1981) but lower than that in the Kuroshio Extension (SCHMITZ, 1984). It is comparable with the level of K_E at abyssal depths in the MODE area (Schmitz, 1978). At Stn. RC, the K_E is large, which might be due to the fact that the station is relatively near to the Kuroshio Extension, considering that the K_E at 4000 m depth along 152° E has the maximum ($45 \text{ cm}^2 \text{ s}^{-2}$) at 35° N , namely the vicinity of the upper layer expression of the Kuroshio Extension (SCHMITZ, 1984).

The spectral features of mesoscale eddies obtained in this study are compared with those of the three-year long first-half of the present record (IMAWAKI and TAKANO, 1982). All the major features of the first-half spectra are found in the present spectra, with a finer resolution and in a wider frequency range. The spectral analysis shows zonal dominance of eddy motions in longer-period bands and meridional dominance in the shorter-period band. If the fluctuations are associated with barotropic Rossby waves, the dominance is understood in the vorticity balance [Eq. (4)] as follows. If the period of waves is longer (shorter), the local change of relative vorticity ζ_t is smaller (larger) and therefore, the advection of planetary vorticity βv_θ is smaller (larger), which means the meridional component v_θ is smaller (larger), i.e., the zonal (meridional) fluctuations are dominant. Those spectral features are also seen in spectra at 4000 m depth in the western North Atlantic (RICHMAN *et al.*, 1977), although zonal dominance of energy

in the annual scale is not definite. The zonal dominance of eddy fields in longer periods has been suggested by theoretical works (e.g., RHINES, 1977). On the other hand, the meridional eddy kinetic energy is dominant in the temporal mesoscale band and even in the annual band at 1000 m depth in the eastern North Atlantic (ZENK and MÜLLER, 1988).

Concerning the vorticity balance, the local change of relative vorticity is balanced primarily with the advection of planetary vorticity, although the advection of relative vorticity and higher-order divergence may play some role in the balance. It is consistent with the earlier results (IMAWAKI, 1983) obtained by using 10-day mean velocities at 5000 m depth at five stations in the present site, whose station-spacing is somewhat similar to the present larger scale examination.

The present study shows that mesoscale eddies at abyssal depths in mid-ocean are understood basically as fluctuations associated with plane barotropic Rossby waves. Recent studies show that mesoscale fluctuations at the present site having specific spectral peaks are explained by topographic Rossby waves better than planetary Rossby waves (MIYAMOTO *et al.*, 2017; 2019); the former are influenced by the topographic beta-effect as well as planetary beta-effect. In the present analyses, topographic Rossby waves are indistinguishable from barotropic planetary Rossby waves. It is because wavelengths cannot be estimated from single-station data and therefore, the dispersion relation of Rossby waves cannot be used for comparison. It is also because the higher-order divergence in the vorticity balance, where the effect of bottom topography appears as well as the baroclinicity, does not seem to be estimated reliably as the residual of first three terms of Eq. (3).

In examination of vorticity balance during

Array-84, missing data at three stations are made up for by linearly interpolated or extrapolated data. Scatter plots of u_{0x} versus v_{0y} and βv_0 versus ζ_t at five stations using those data (Figs. 16 and 17) do not show any difference among stations. Therefore, the interpolation and extrapolation seem to have worked well. Objective analysis may improve filling the missing data as well as spatial smoothing.

9. Summary

Velocities at abyssal depths were measured by moored current-meters in mid-ocean of the western North Pacific during 1978–1985. Current-meters were moored mostly at 4000 and 5000 m depths at various locations for several months to one year repeatedly, providing 50 velocity records. In the raw data, inertial oscillations are apparent as well as diurnal and semi-diurnal tidal fluctuations. Those high-frequency fluctuations are filtered out numerically and low-pass-filtered daily velocities are used for the present analyses.

Time-space averages of statistics of 47 individual records at abyssal depths show followings. The average zonal and meridional velocity-components are less than 1 cm s^{-1} in magnitude. The average zonal and meridional variances are almost equal to each other. The eddy kinetic energy is about 40 times larger than the mean kinetic energy. Those statistics confirm that the site is located in typical mid-ocean apart from intense current zones. Both mean velocities and fluctuating velocities at abyssal depths at the same station are similar to each other.

A long velocity record for almost seven years was obtained at 5000 m depth at Stn. RB. This is probably one of the longest continuous records from moored current-meters at depth in the mid-ocean over the world. The overall mean velocity is directed to the north with a speed of less than

1 cm s^{-1} . The mean meridional velocity-component is positive significantly at the 95 % confidence level, while the mean zonal component is not significantly different from zero. The zonal variance is similar to the meridional variance. The eddy kinetic energy is more than 30 times larger than the mean kinetic energy. Those statistics are quite similar to the time-space averages of all individual statistics at abyssal depths mentioned above, suggesting that the long record at Stn. RB represents the flow field at the present site quite well, although the mean velocity might be under the effect of the local steady vortex.

This long velocity record at Stn. RB gives statistically significant estimates of frequency spectra for the eddy kinetic energy. Most of the eddy kinetic energy is contained in mesoscale bands I, II and III (period-range of 31–235 days). In the three bands as a whole, zonal and meridional energies are almost equal to each other. In the mesoscale I (120–235 days) the zonal energy is dominant, while in the mesoscale III (31–61 days) the meridional energy is dominant. In the annual/secular scale (295–4924 days) the zonal energy is highly dominant. Both zonal dominance in longer-period bands and meridional dominance in the shorter-period band are understood qualitatively by difference in phase propagation direction of fluctuations, if the fluctuations are assumed as plane barotropic Rossby waves having wavelengths of hundreds of kilometers.

The vorticity balance of mesoscale eddies is examined by using those current-meter data. Relative vorticity is estimated from horizontal derivatives of 20-day mean velocities. Its local change during 20 days is compared with the advection of planetary vorticity, at five stations, providing 75 independent comparison cases. The overall correlation coefficient between the two properties of those cases is -0.61 , which is high

enough to be significantly different from zero at the 95 % confidence level. The overall standard deviations of the two are not much different from each other. Therefore, the local change of relative vorticity is balanced primarily with the advection of planetary vorticity, although the advection of relative vorticity and higher-order horizontal divergence may play some role in the balance.

Those results suggest that mid-ocean mesoscale eddies at abyssal depths are understood as primarily plane barotropic Rossby waves with possible modification.

Acknowledgements

We thank Mr. Masatoshi Miyamoto of the University of Tokyo for informing the ETOPO1 bottom topography. We are grateful to two anonymous reviewers and Prof. Masahisa Kubota of Tokai University for careful and critical reading of the manuscript and valuable comments. We also thank Mr. Keith Bradley of the Woods Hole Oceanographic Institution (at that time) for introducing SI to the mooring technique. [Affiliation is hereafter understood “at that time.”] The mooring observations were carried out under the lead of KT of the Institute of Physical and Chemical Research and later of the University of Tsukuba with collaboration of SI of Kyoto University. We thank Mr. Satoshi Murata of the University of Tsukuba for his helpful assistance. Mooring deployment and recovery were carried out on board the research vessel *Hakuho Maru* of the University of Tokyo, the research and training vessels *Tokaidaiigaku Maru II* and *Bosei Maru II* of Tokai University (Table 1). We thank Captains and crews of those vessels for their earnest cooperation. The current measurements were done as a pre-operational survey for the disposal of low-level radioactive wastes, financially supported by the Science and Technology

Agency through the Radioactive Waste Management Center. The data were processed at the Data Processing Center of Kyoto University. The work was partly supported by Grants-in-Aid from the Ministry of Education, Science and Culture. The present low-pass-filtered velocities are available at the Website of Japan Oceanographic Data Center; <http://www.jodc.go.jp/jodcweb/JDOSS/>.

References

- AMANTE, C. and B. W. EAKINS (2009): ETOPO1 1 Arc-Minute Global Relief Model: Procedures, Data Sources and Analysis. NOAA Technical Memorandum NESDIS NGDC-24. National Geophysical Data Center, NOAA. doi: 10.7289/V5C8276M.
- CREASE, J. (1962): Velocity measurements in the deep water of the western North Atlantic, summary. *J. Geophys. Res.*, **67**, 3173–3176.
- FU, L.-L. and R. MORROW (2013): Remote sensing of the global ocean circulation. *In* Ocean Circulation and Climate: A 21st Century Perspective. G. SIEDLER, S. M. GRIFFIES, J. GOULD and J. A. CHURCH (eds.), Academic Press, London, pp. 83–111.
- GODIN, G. (1972): *The Analysis of Tides*. Liverpool University Press, 264 pp.
- GREENE, A. D., D. R. WATTS, G. G. SUTYRIN and H. SASAKI (2012): Evidence of vertical coupling between the Kuroshio Extension and topographically controlled deep eddies. *J. Mar. Res.*, **70**, 719–747, doi: 10.1357/002224012806290723.
- HEINMILER, R. H. (1976): Mooring Operations Techniques of the Buoy Project at the Woods Hole Oceanographic Institution, W.H.O.I. Technical Report 76-69. Woods Hole Oceanographic Institution, Woods Hole, Massachusetts, 94 pp.
- IMAWAKI, S. (1983): Vorticity balance for mid-ocean mesoscale eddies at an abyssal depth. *Nature*, **303**, 606–607, doi: 10.1038/303606a0.
- IMAWAKI, S. (1985): Features of mesoscale eddies in the deep mid-ocean of the western North Pacific. *Deep-Sea Res.*, **32**, 599–611, doi: 10.1016/0198-0149(85)90046-9.
- IMAWAKI, S. and K. TAKANO (1982): Low-frequency

- eddy kinetic energy spectrum in the deep western North Pacific. *Science*, **216**, 1407–1408, doi: 10.1126/science.216.4553.1407.
- IMAWAKI, S. and K. TAKANO (2019): Steady vortex observed by moored current-meters at 4000 m depth in the western North Pacific. (to be published)
- KAWABE, M. and S. FUJIO (2010): Pacific Ocean circulation based on observation. *J. Oceanogr.*, **66**, 389–403, doi: 10.1007/s10872-010-0034-8.
- KEFFER, T. (1983): Time-dependent temperature and vorticity balances in the Atlantic North Equatorial Current. *J. Phys. Oceanogr.*, **13**, 224–239.
- MCWILLIAMS, J. C. (1976): Maps from the Mid-Ocean Dynamics Experiment: Part II. Potential vorticity and its conservation. *J. Phys. Oceanogr.*, **6**, 828–846.
- MCWILLIAMS, J. C. and G. R. FLIERL (1976): Optimal, quasi-geostrophic wave analyses of MODE array data. *Deep-Sea Res.*, **23**, 285–300.
- MIYAMOTO, M., E. OKA, D. YANAGIMOTO, S. FUJIO, G. MIZUTA, S. IMAWAKI, M. KUROGI and H. HASUMI (2017): Characteristics and mechanism of deep mesoscale variability south of the Kuroshio Extension. *Deep-Sea Res. I*, **123**, 110–117, doi: 10.1016/j.dsr.2017.04.003.
- MIYAMOTO, M., E. OKA, D. YANAGIMOTO, S. FUJIO, M. NAGASAWA, G. MIZUTA, S. IMAWAKI, M. KUROGI and H. HASUMI (2019): Topographic Rossby waves at two different periods in the Northwest Pacific Basin. (to be published)
- MODE GROUP (1978): The Mid-Ocean Dynamics Experiment. *Deep-Sea Res.*, **25**, 859–910.
- NILER, P. (2001): The world ocean surface circulation. *In* *Ocean Circulation and Climate: Observing and Modelling the Global Ocean*. G. Siedler, J. Church, and J. Gould (eds.), Academic Press, London, pp. 193–204.
- PEDLOSKY, J. (1996): *Ocean Circulation Theory*. Springer-Verlag, Berlin, 453 pp.
- PRICE, J. F. and H. T. ROSSBY (1982): Observations of a barotropic planetary wave in the western North Atlantic. *J. Mar. Res.* **40**, suppl., 543–558.
- RHINES, P. B. (1977): The dynamics of unsteady currents. *In* *The Sea: Ideas and Observations on Progress in the Study of the Seas*, Vol. 6. E. D. GOLDBERG, I. N. MCCAIVE, J. J. O'BRIEN and J. H. STEEL (eds.), Wiley, New York, pp. 189–318.
- RICHMAN, J. G., C. WUNSCH and N. G. HOGG (1977): Space and time scales of mesoscale motion in the western North Atlantic. *Rev. Geophys. and Space Phys.*, **15**, 385–420.
- ROBINSON, A. R. (ed.) (1983): *Eddies in Marine Science*. Springer-Verlag, Berlin, 609 pp.
- SCHMITZ, W. J., Jr. (1978): Observations of the vertical distribution of low frequency kinetic energy in the western North Atlantic. *J. Mar. Res.*, **36**, 295–310.
- SCHMITZ, W. J., Jr. (1984): Abyssal eddy kinetic energy levels in the western North Pacific. *J. Phys. Oceanogr.*, **14**, 198–201.
- TAFT, B. A., S. R. RAMP, J. G. DWORSKI and G. HOLLOWAY (1981): Measurements of deep currents in the central North Pacific. *J. Geophys. Res.*, **86**, 1955–1968.
- TALLEY, L. D., G. L. PICKARD, W. J. EMERY and J. H. SWIFT (2011): *Descriptive Physical Oceanography: An Introduction*, Sixth Edition. Elsevier, London, 555 pp.
- UCHIDA, H. and S. IMAWAKI (2003): Eulerian mean surface velocity field derived by combining drifter and satellite altimeter data. *Geophys. Res. Lett.*, **30**, 1229, doi: 10.1029/2002GL016445.
- ZENK, W. and T. J. MÜLLER (1988): Seven-year current meter record in the eastern North Atlantic. *Deep-Sea Res. A*, **35**, 1259–1268, doi.org/10.1016/0198-0149(88)90082-9.

Received: September 19, 2018

Accepted: December 20, 2018

高解像度海洋モデルで表現された富山湾周辺海域における 近慣性内部波・沿岸捕捉波の発生・伝播過程

久賀みづき^{1)*}・井桁庸介¹⁾・広瀬直毅²⁾・渡邊達郎¹⁾

Generation and propagation processes of near-inertial internal waves and coastal-trapped waves in and around Toyama Bay, Japan, calculated by high-resolution nesting ocean model

Mizuki KUGA^{1)*}, Yosuke IGETA¹⁾, Naoki HIROSE²⁾ and Tatsuro WATANABE¹⁾

Abstract: Characteristics of near-inertial fluctuations generated by typhoon in and around Toyama Bay (TB) that opens its mouth toward the north were investigated by using results calculated by high-resolution nested ocean model which is usually operated for fisheries. From harmonic, spectral and vertical-mode decomposition analysis, we confirmed that density and current fluctuations were fundamentally characterized by propagation of coastal-trapped waves (CTWs) generated at seamount adjacent to the land tip of Noto Peninsula (NP) that is western boundary of the TB. This result in counterclockwise phase distribution in density fields. Near-inertial internal waves (NIWs) were also generated around land tip (Nyuzen) located at the eastern boundary of the TB through topographical scattering processes of the CTWs. The NIWs propagated the northwestward by way of center of the TB, finally were reflected along the eastern coast of the NP toward the northeast. The NIWs formed clockwise phase distribution in current fields, which is opposite properties against that by the CTWs. The region of strong currents confirmed around the Nyuzen was considered to be resonant-amplification of currents of the CTWs and inertial oscillations.

Keywords: *near-inertial coastal-trapped waves, near-inertial internal waves, deep bay, high-resolution ocean model*

-
- 1) 水産研究・教育機構 日本海区水産研究所
〒 951-8121 新潟県新潟市中央区水道町水道町
1丁目 5939-22
Japan Sea National Fisheries Research Institute,
Japan Fisheries Research and Education Agency,
1-5939-22 Suido-cho, Chuo, Niigata 951-8121,
Japan
- 2) 九州大学応用力学研究所
〒 816-8580 福岡県春日市春日公園 6-1
Research Institute for Applies Mechanics,

Kyushu University, 6-1 Kasuga-koen, Kasuga
city, Fukuoka, 816-8580, Japan

*連絡著者：久賀みづき

〒 951-8121 新潟県新潟市中央区水道町水道町
1丁目 5939-22

水産研究・教育機構 日本海区水産研究所

Tel: 025-228-0619

Fax: 025-223-7425

E-mail : mkuga@affrc.go.jp

1. はじめに

富山湾を中心とした能登～佐渡周辺海域では、気象擾乱に伴い、沿岸で強流が発生し定置網のワイヤーが破断するなどの被害が出ることもある。この現象は急潮と呼ばれ、日本海沿岸域における気象擾乱に伴う急潮は、沿岸捕捉波、沿岸密度流、近慣性周期変動等の、様々な海洋物理現象で解釈が試みられてきた（例えば、浅ら, 2007; IGETA *et al.*, 2009; 大慶ら, 2015）。

当該海域における沿岸捕捉波は、能登半島西岸～北岸において南～南西風の連吹によって発生し、それが5～10日周期スケールの変動として岸を右に見て能登半島東岸域へ伝播することが知られている（例えば、IGETA *et al.*, 2011）。そのシグナルは、定置網での流速観測や検潮所における潮位観測等で頻繁に確認できることから比較的多くの研究がなされている（例えば、FUKUDOME *et al.*, 2016）。一方、急潮へ寄与するような沿岸域における近慣性周期変動についても、岸に捕捉され海岸線を右に見て伝播する現象として解釈されてきた（浅ら, 2007; IGETA *et al.*, 2007）。これは、近慣性内部波が半島の先端部のような陸岸の突端部において散乱し、散乱波が近慣性沿岸捕捉波（DALE *et al.*, 2001）の特性を持って伝播したものと考えられている（IGETA *et al.*, 2009; 山崎ら, 2015）。

以上のような背景の下、岸を右に見て伝播する現象が急潮予測における根拠として使用されてきた（大慶ら, 2012）。一方、大慶ら（2015）は、能登半島東岸域において2週間程度持続した近慣性周期変動の観測事例を示し、それが定置網の操業を妨げたことを報告した。この近慣性周期変動の特徴として、能登半島東岸沿いの離れた2測点で時間的に同期する変動を持つことを挙げ、岸に沿って伝播すると考えると非常に大きな伝播速度を持つ（約 10ms^{-1} ）とした。そして、彼らはこれを能登半島沖で回折し海岸線に向かって伝播した近慣性内部波による流動であると推測した。

近慣性内部波は基本的には風によって励起される慣性振動をエネルギー源とし、発生域よりも赤道側へ伝播することが知られている（GILL, 1984; GARRETT, 2001）。一方で、陸岸境界が存在する状

況下で慣性振動が発生した場合には収束発散が強制的に起こり、それらが波源となり、近慣性内部波が発生・伝播する（KUNDU, 1984; WATANABE and HIBIYA, 2018）。従って、海洋の南岸にあり、且つ複雑な海岸・海底地形を持つ能登半島～富山湾周辺海域（Fig. 1 (a)）では、慣性振動の発生、もしくは近慣性内部波の入射の際の反射・回折過程を通して、近慣性沿岸捕捉波から近慣性内部波（慣性重力波）へのエネルギー移行、またその逆の過程が狭い海域内で起こり、複雑な振動系が形成される可能性が高い。大慶ら（2015）の観測は、そのような振動系の一端を捉えた可能性が高いが、その全体像や詳細については殆ど分かっていない。

複雑な海岸・海底地形による近慣性内部波の発生・反射・散乱を経て形成された振動系の時空間的な特徴を理解するためには、ロスビー内部変形半径を十分に解像した海洋数値モデルを用いた数値実験が適している。そこで本研究では、日本海区水産研究所で現業運用されている「リアルタイム急潮予測システム（<http://kyucho.dc.affrc.go.jp/kyucho/>）」の確定値を用い、富山湾周辺海域で気象擾乱に伴って発生した近慣性内部波の伝播過程の記述を試みた。

2. 数値モデル, データ

リアルタイム急潮予測システムの海洋数値モデルは九州大学応用力学研究所開発のDR_C（HIROSE *et al.*, 2017）で、より現実的な日本海沿岸の流れを再現するための高解像度シミュレーションモデルである。基盤となる海洋モデルはRIAM Ocean Model（LEE *et al.*, 2003）で、球面座標系において静水圧平衡の下でブシネスク近似、自由表面を仮定したプリミティブ方程式を有限差分法で解く海洋大循環モデルである。Fig. 1 (b)に示す鳥取県～山形県沿岸を計算領域とし、水平解像度は東西1分、南北0.8分、鉛直層数は36層で、表層ほど鉛直解像度が高い（鉛直36層; 層厚2～480m）。海底地形はJTOPO30v2とJ-EGG500の相加平均によって作成された。さらに、海岸の地形をより現実的にする為の修正が施されてい

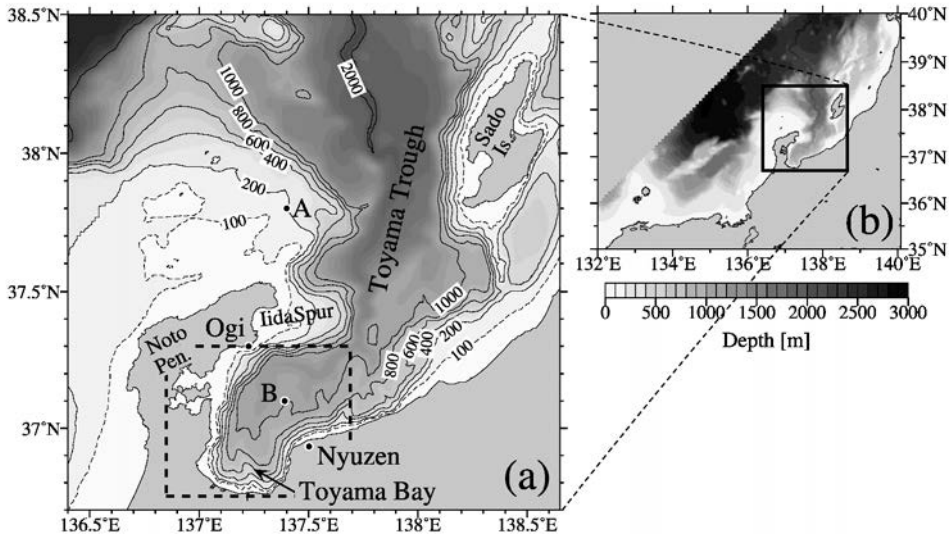


Fig. 1 Bottom topography of (a) study area around Toyama Bay and (b) model domain of DR_C. Station A and B indicate representative locations of wind and current velocity shown in Fig.3. Horizontally averaged values are estimated in the region enclosed by the dashed line.

る。開境界条件は、日本海と東シナ海を計算領域とする渦解像可能なデータ同化モデル DR_M (HIROSE *et al.*, 2013) による単方向ネスティングによって、海面高度、水温、塩分、水平流速（東・北向き成分）が与えられている。気象外力は気象庁のGPV-MSM データ（海面気温、比湿、雲量、降水量、風ベクトル）を時空間で線形補間して与えている。

解析に使用した出力変数は、水平流速（東・北向き成分）、水温、塩分の1時間平均値で、それぞれの出力時間間隔は1時間である。解析対象期間である2010年8月10日9時から23日9時までのデータを使用した。本稿では、このシステムで計算されたデータを DR_C データと呼ぶことにする。

3. 結果

3.1 台風1004号による近慣性周期変動の励起

DR_C データには、気象擾乱のない静穏時に対馬暖流沿岸・沖合分枝、地形性渦、もしくはそれらを起源とする流動現象が見られた。一方で、台

風・温帯低気圧通過時には富山湾内外に短周期で変動する強流を確認出来た。また、その強流については、岸に捕捉された数日間持続する流れと、沖合での振動する流れとが混在する様子が見られた。本研究では、近慣性周期変動が卓越した一例として、2010年8月に能登半島の北沖を東進した台風1004号（T04）通過に伴う近慣性周期変動に着目する。

T04は2010年8月7日頃にフィリピン沖で発生した後に北上した。11日に対馬海峡を經由し日本海へ入り、能登半島北方沖を12日9~12時の間に通過した（Fig. 2）。能登半島~富山湾周辺では、T04接近に伴い南風が強まったが、台風中心が能登半島付近を通過した12日午前以降は、風速ベクトルが時計回りに回転しつつ北寄りの風に変わった（Fig. 3 (a)）。

能登半島北方沖を北東方向へ進行する台風・温帯低気圧は、能登半島~富山湾沿岸域に風速ベクトルが時計回りに回転するような時間変動をする風速場を形成する。このような風速場は近慣性振動流を共鳴的に強めることが知られており

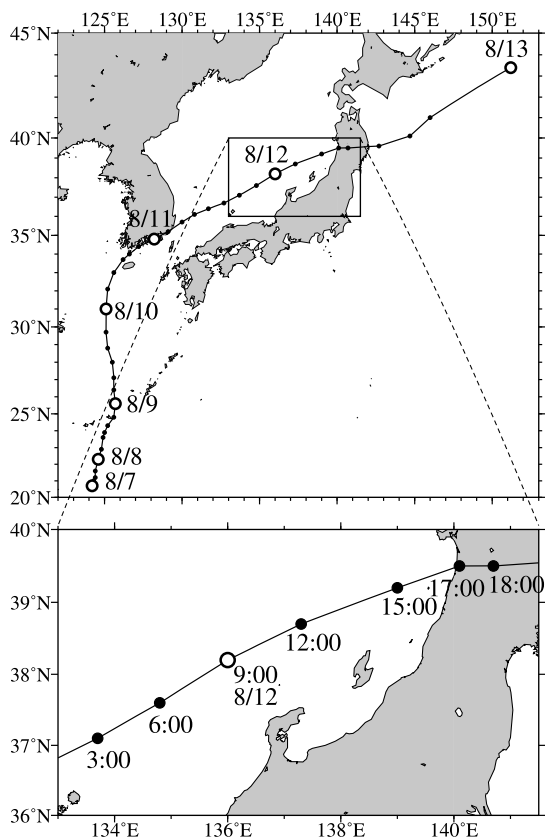


Fig. 2 Track of Typhoon 1004. Open circles denote the position at 9:00JST.

(D'ASARO, 1985), このような台風・低気圧によって当該海域に大きな振幅の近慣性振動流が発生することが知られている (例えば, 大慶ら, 2009; IGETA *et al.*, 2011; 大慶ら, 2015; 山崎ら, 2015)。T04 は上記の海洋物理現象を効果的に発生させる気象擾乱として良い例であると共、この台風に伴う流動変動は、DR_C によって高い精度で再現されたことが HIROSE *et al.* (2017) で示されていることから、近慣性周期変動の挙動を調べるには非常に適した事例である。

まず、T04 通過による近慣性周期変動が DR_C データに見られるかどうかを確認する。Fig. 3 (b) は、Fig. 1 (a) の測点 B における 30m 深流速の東西・南北成分である。台風通過直後から、富山湾内では流速振幅が大きくなり、東西・南北成

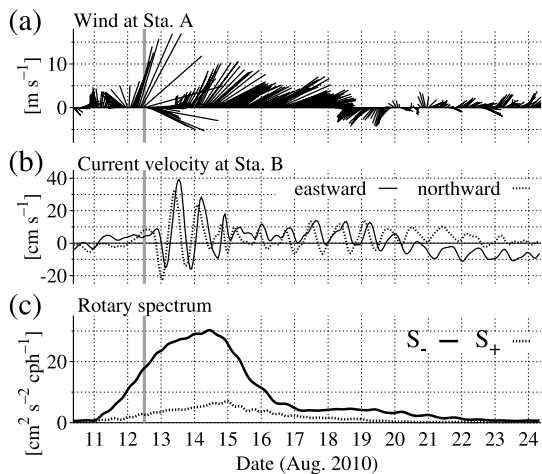


Fig. 3 Time series of (a) wind vectors at station A, (b) eastward (solid line) and northward (dashed line) current velocities at station B at the depth of 30m, and (c) clockwise (solid line) and counterclockwise (dashed line) spectra of current with a period of 19-hours averaged horizontally at the depth of 30m. The gray vertical lines indicate the time when Typhoon 1004 passed the north of Noto Peninsula.

分ともに同程度の振幅で振動している。流速の振動周期は 20 時間程度で、東西、南北成分で位相が 90° 程度ずれていることから、流体粒子が水平的に円運動をしていたことが分かる。この流速振動は 19 日まで確認出来る。

流速の振動周期を見積もるために、水平流速の時計回り、反時計回りの回転スペクトルエネルギー密度 S_- , S_+ (付録 A (1a), (1b) 式) を直接フーリエ変換により算出した。富山湾内の測点 B (Fig. 1 (a)) における 30m 深水平流速の 8 月 11 日 9 時から 19 日 9 時の時系列データを使って得られた回転スペクトルエネルギー密度 (Fig. 4) から、19 時間周期の時計回り流速振動が卓越していることがわかった。これに従い、本事例では、19 時間周期変動を近慣性周期変動と定義した。なお、反時計回り成分 S_+ の振幅が非常に小さいことから回転係数 C_R は 1 に近く、流速ベクトルの時間変化が真円に近い軌道を描くことがわかる (付

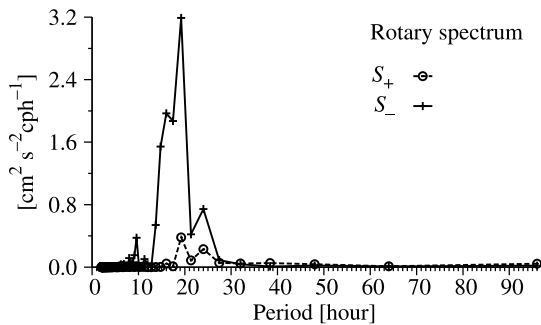


Fig. 4 Clockwise (solid line) and counterclockwise (dashed line) spectra of current at the depth of 30m at station B calculated by the data from 9:00JST, August 11 to 9:00JST, August 18.

録 A 参照)。

3.2 富山湾周辺における近慣性周期変動の発達、伝播過程

近慣性周期変動の卓越する期間に注目し、富山湾周辺における近慣性周期変動の発達、伝播過程を調べる。まず、近慣性周期変動が富山湾周辺海域で卓越していた時期を把握するために、T04 通過前後の近慣性周期変動エネルギーの時間変化を調べる。Fig. 3 (c) は、30m 深水平流速の 19 時間周期の回転スペクトルエネルギー密度の時間変化である。ラベルの時刻を中心に 95 時間 (19 時間周期 5 周期分の長さ) の時系列データを用いて見積もり、それを 1 時間ずつずらして計算し時間変化とした。なお、値は富山湾周辺海域 (Fig. 1 (a) 点線領域) の平均値である。能登半島沖を T04 が通過した後、時計回りのエネルギー密度が約 3 日間高い値を維持するが、15 日以降は急激にエネルギーレベルが下がっている。一方、反時計回りのエネルギー密度は時計回りのエネルギー密度よりも 1/4 程小さかった。従って、本事例で近慣性周期変動が卓越した期間として、T04 が通過した 8 月 12 日 12 時から 72 時間を中心として解析した。

18.5 から 19.5 時間周期のバンドパスフィルターによって抽出した近慣性周期変動による密度偏差と流速ベクトルの水平分布を Fig. 5 に示す。季節躍層以深の代表として 120m 深、季節躍層付

近の代表として 30m 深の結果を示した。まず、季節躍層以深の 120m 深では、能登半島北東端の飯田海脚周辺で正の密度偏差が発生し (Fig. 5 (a))、それが沿岸で岸を左に見る流れを伴いつつ岸を右に見ながら富山湾、入善を経由し、入善以東へと伝播した (Fig. 5 (b) ~ (d))。一方で、季節躍層付近の 30m 深では、大まかな密度・流速変動は 120m 深と類似するものの、流れの強い海域、弱い海域が散在し、複雑な水平構造を持っている (Fig. 5 (e) ~ (h))。また、富山湾東端の海岸線が凸状に沖へ張り出す入善沖から能登半島東岸へ伝播するような円弧状の波面のようなもの (Fig. 5 (f) ~ (h) の低密度偏差領域) も確認出来る。

120m 深における近慣性周期変動 1 周期分 (8 月 13 日 18 時~14 日 12 時) について 18.5~19.5 時間周期のバンドパスフィルターを適用した密度偏差の最大値の水平分布 (Fig. 6 (f)) から、飯田海脚周辺の大陸斜面付近に振幅の大きい領域がみられる。そこから小木、富山湾、入善を経由し、入善以東まで、密度偏差の大振幅領域が沿岸~大陸斜面に捕捉される形で分布している。同様に算出した 120m 深における流速の最大値の水平分布では、富山湾以西では、流れは基本的に岸で最も強く、沿岸に捕捉される特徴を持つが、能登半島東岸では、強流域がパッチ状に分布する (Fig. 6 (c))。一方、30m 深の密度偏差 (Fig. 6 (e)) では、能登半島東岸域での振幅は小さいものの、基本的には 120m 深の密度偏差同様に振幅の大きい領域が岸に捕捉される特徴が現れている。密度・流速変動が沿岸に捕捉されている特徴は、IGETA *et al.* (2009) で議論された、半島突端部で慣性振動もしくは近慣性内部波が散乱することで発生した近慣性沿岸捕捉波の特徴が現れたものだと考えられ、その発生域は飯田海脚上の 100m 深等深線で確認出来る浅瀬周辺であると判断できる。

一方、Fig. 6 (b) に示した 30m 深の流速最大値では入善沖で流れが最も強く、次いで小木南岸、さらに能登半島東沖 (800m 等深線より沖合の領域) に強流帯を確認できる。エクマン層内の水深 6.5m の流速最大値の分布 (Fig. 6 (a)) は 30m 深と類似しているが、飯田海脚沖の強流帯は 30m

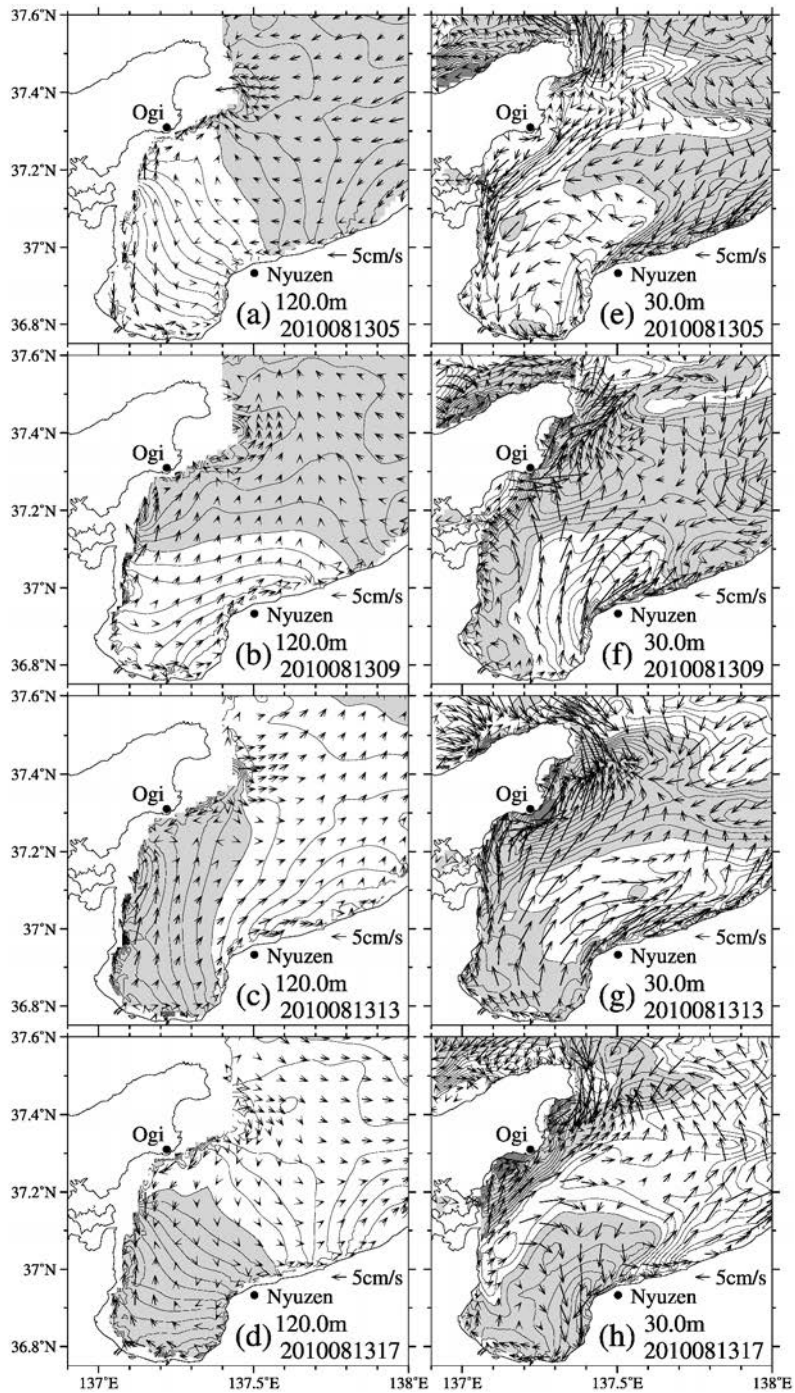


Fig. 5 Density anomaly (contour) and current (vector) of the period of 19-hours at the depth of (a-d) 120m and (e-f) 30m. Contour intervals of density anomaly are every $2 \times 10^{-5} \text{kgm}^{-3}$. The positive anomaly of density is shaded.

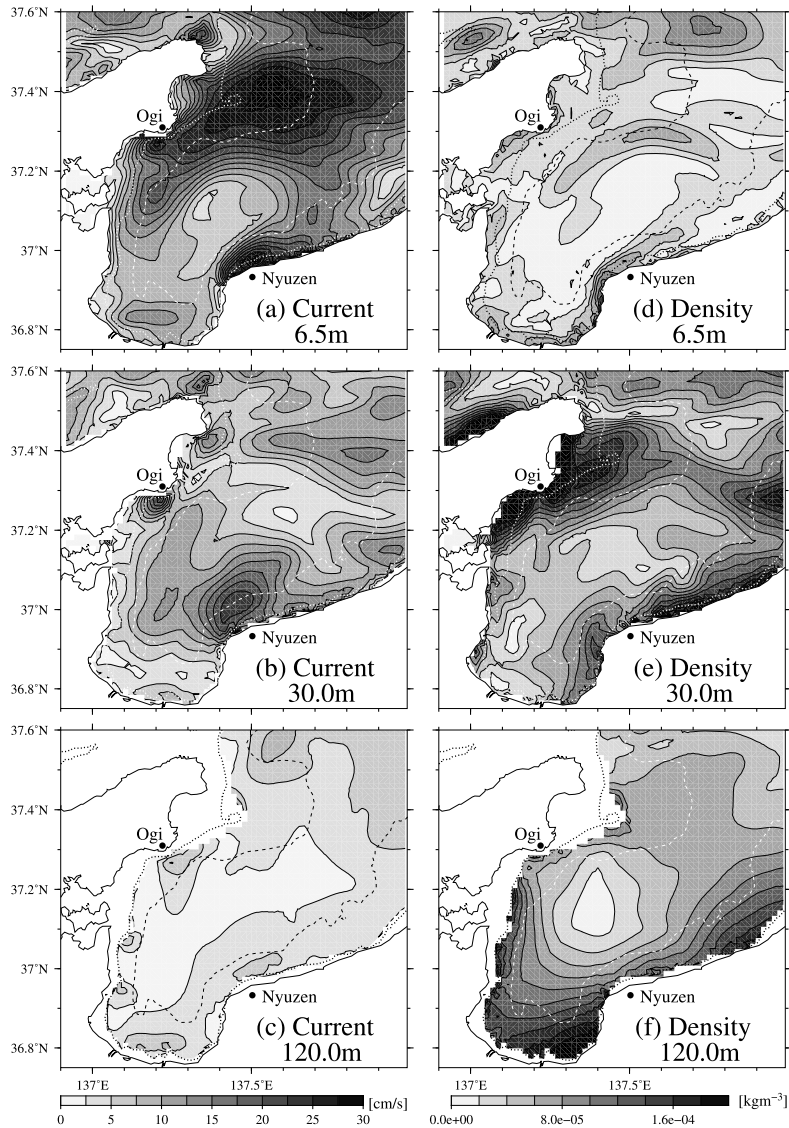


Fig. 6 Maximum (a-c) current velocity and (d-f) density anomaly during 19 hours around 3:30, August 14 at the depth of 6.5, 30 and 120m. Dashed and dotted lines are the contour at the bottom depth of 800m and 100m respectively.

深に比べて広範囲に分布している。以上から、30m 深以浅の流速分布には、近慣性沿岸捕捉波の伝播に加えて、近慣性内部波等の波動、もしくはそれに類する流動現象が重なり合うことで、複雑な振動形態を示したと判断できる。以降、その要

因をできる限り分離して示し、この複雑な流動・密度変動を理解することを試みる。

近慣性周期変動・内部波の伝播の時空間特性を可視化するために、密度偏差・流速変動の振幅と位相の空間構造を見積もる。密度偏差については

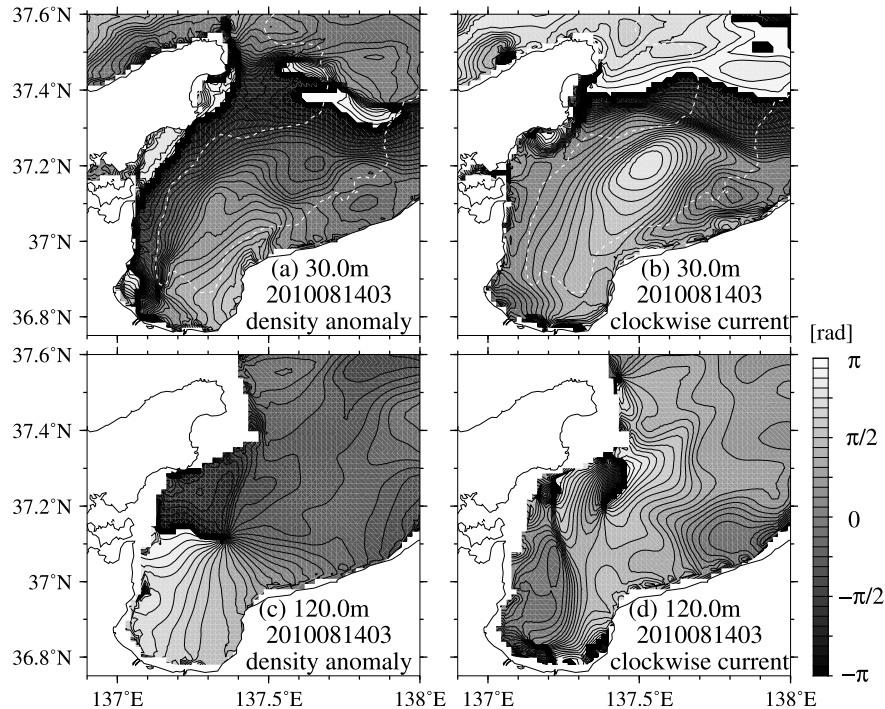


Fig. 7 Horizontal distribution of phase for (a) the potential density anomaly and (b) the clockwise component of horizontal current with a period of 19-hours calculated from the data for 95 hours around 3:30, August 14 at the depth of 30 m. (c), (d) are same as (a), (b) but for the depth of 120 m. Dashed lines are the contour at the bottom depth of 800m.

調和解析を用いて見積もるが、水平流速に関しては、その時計回り成分 Z_{-} (付録 A (4b) 式) の偏角 $\arg(Z_{-}(\sigma))$ を位相として、その空間構造に注目し特徴を抽出することを試みる。解析対象期間に関して、Fig. 3 (c) で実施した計算と同様に 95 時間分の流速データを使って、DR_C データの各水深、各グリッドについて見積もった。Fig. 7 に、密度偏差と流速の時計回り成分の 8 月 14 日 3 時 (8 月 12 日 4 時~8 月 16 日 2 時のデータを使用) の近慣性周期変動 (19 時間周期変動) の位相の水平分布を示した。季節躍層付近の代表として 30m 深、季節躍層以深の代表として 120m 深の結果を示している。位相の進行方向は π から $-\pi$ の向きである。ここで、振幅については、それぞれの水深帯で Fig. 6 に示した近慣性周期流速変動

の 1 周期間の最大値分布と良く似ていたため、本稿では重複を避けるため提示を省略する。

120m 深では、富山湾北方沖に密度偏差変動の無潮点があり、無潮点を中心に反時計回りに位相伝播していた様子が確認できるが (Fig. 7 (c))、その特徴は流速の時計回り成分では明確ではない (Fig. 7 (d))。一方 30m 深では、密度偏差、流速の時計回り成分の双方で、能登半島東沖では等位相線が海岸線に平行に分布し、能登半島東沿岸の広い範囲 (能登半島東岸の海岸線と 800m の等深線で囲まれた領域) で、岸に沿った方向で同位相に近い流速・密度変動が確認できる (Fig. 7 (a), (b))。この等位相線の分布は、近慣性周期変動が入善沖から能登半島東岸に向かって伝播し、その波面が海岸線・大陸棚に平行に入射していること

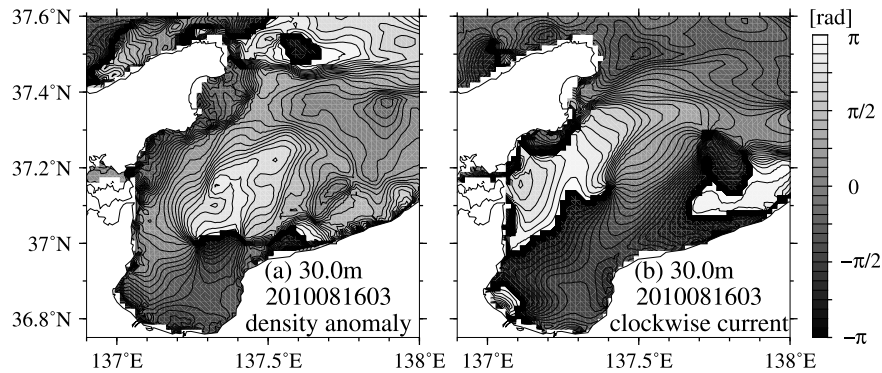


Fig. 8 Same as Fig. 7 (a), (b) but for calculated from the data for 95 hours around 3:30, August 16.

を示している。また、この等位相線が能登半島東沖に平行に分布する海域は、流速振幅が比較的大きい海域 (Fig. 6 (b) 800m の等深線より沖合) と重複している。

以上から、Fig. 5 の時間連続図で確認された、(1) 岸を右に見て伝播する沿岸捕捉波、(2) 入善沖から能登半島東岸への波動伝播の 2 つの特徴が、5 慣性周期の代表的な近慣性周期変動の特性として定量的に抽出できた。この振動系は約 2 日間持続したが、エネルギーが急激に減衰するのに伴い (Fig. 3 (c)), その位相構造は緩やかに変化した。これを示すために、近慣性周期変動の流速の時計回り成分の振幅が、8 月 14 日の半分程度にまで減少した 8 月 16 日を中心とした 5 慣性周期分のデータを用いて、30m 深の密度偏差と流速の位相分布を見積もった (Fig. 8)。密度偏差変動については、2 日前の 120m 深に見られた反時計回りの位相伝播構造 (Fig. 7 (c)) とほぼ同じ位相分布に変化し、沿岸捕捉波の伝播のシグナルが明確に現れている (Fig. 8 (a))。一方で、流速の時計回り成分に関しては、飯田海脚南方沖に無潮点が形成され、そこを中心の時計回りの伝播を示す分布となった (Fig. 8 (b))。これは、能登半島東沖～富山湾沖合の無潮点を中心に、最終的には、密度偏差は反時計回り、流速変動は時計回りと、逆に伝播する振動系が形成されたことを意味している。ここで、流速の時計回り成分の振幅の空間構

造は殆ど変化しなかった。

4. 考察

能登半島東岸～富山湾周辺海域の近慣性周期変動に関して以下の 4 つの特徴を抽出した：(1) 能登半島北東端で発生し、岸に捕捉された密度・流速変動 (反時計回りの位相構造)；(2) 入善沖から能登半島東岸への波動伝播；(3) エネルギー減衰中の流速の時計回り成分の時計回りの位相伝播 (密度変動と逆)；(4) 入善沖における強流帯形成。(1) は上述の通り、半島突端部で慣性振動 (または近慣性内部波) が散乱することで発生した近慣性沿岸捕捉波の特徴だと考えられるが、(2)・(3) は入善沖で何らかの要因で発生した近慣性内部波、(4) は、これらの波動もしくはそれに類する振動流の重ね合わせで形成されたと類推される。以下、上記 (2)～(4) について考察する。

4.1 富山湾東端で近慣性沿岸捕捉波の散乱によって発生する近慣性内部波

入善沖から能登半島東岸へ北西進する波動の発生タイミングを、Fig. 5 を用いて再確認する。30m 深では、能登半島東岸へ波及する近慣性内部波の峰の部分 (低密度偏差域) が、能登半島東岸沖で概ね岸に平行に分布することが 30m 深において明確に確認できる (Fig. 5 (h))。この峰の位置について時間を遡って追跡すると (Fig. 5 (g),

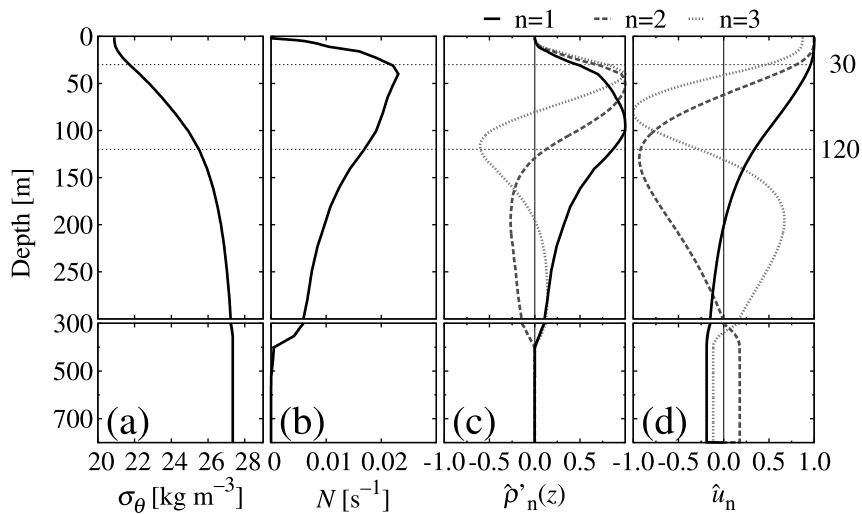


Fig. 9 Vertical profiles of (a) potential density, (b) buoyancy frequency averaged horizontally and temporally from 4:30, August 12 to 2:30, August 16, and the lowest three internal modes of (c) potential density anomaly and (d) horizontal velocity estimated from (b) interpolated linearly to 1m intervals. Horizontal dotted lines indicate the depth corresponding to the depth shown in Fig. 7.

(f), この波源は富山湾東端の入善沖であるように見える (Fig. 5 (f))。一方, Fig. 5 (f) と同時刻に, 120m 深 (Fig. 5 (b)) では, 能登半島東岸に沿って北から波及してきた近慣性沿岸捕捉波の峰の部分, 入善近傍を通過していることが明確に確認できる。なお, 図には示さないが, 近慣性沿岸捕捉波の谷の部分, 伝播する際にも, ほぼ同様の波動の伝播様式が確認できる。

一連の時間発展から, 入善沖から能登半島東岸へ波及する近慣性内部波は, 近慣性沿岸捕捉波の入善沿岸における海岸地形の水平的な変化による散乱過程を通して, 近慣性沿岸捕捉波から慣性重力波へエネルギーが変換される (例えば, WILKIN and CHAPMAN, 1990; DALE *et al.*, 2001) ことにより発生したと推測される。以下, 富山湾周辺海域における近慣性内部波の伝播シグナルを可能な限り抽出・描画することで, この推測の妥当性を示す。

富山湾周辺海域で近慣性内部波が持ち得る各鉛直モードの水平流速・密度の鉛直構造を見積もった (算出方法は付録 B 参照)。計算に用いたポテンシャル密度の鉛直プロファイル (Fig. 9 (a))

は, 富山湾周辺海域 (Fig. 1 (a) 点線領域) で領域平均し, さらに位相分布の算出に用いたデータの期間 (8月12日4時~8月16日2時) で期間平均をとった値とした。密度偏差 $\hat{\rho}'_n$, 水平流速 \hat{u}_n について, 低次の3つのモードの鉛直プロファイルを Fig. 9 (c), (d) に示した。

鉛直第1モードは位相速度 $c_1=1.94$ m/s で, 231m 深に水平流速の節を持ち, 95m 深に密度偏差の腹を持つ。鉛直第2モードは位相速度 $c_2=0.86$ m/s で, 水平流速については131m 深に腹, 62, 320m 深に節を持ち, 密度偏差については129m 深に節, 52, 196m 深に腹を持つ。鉛直第3モードは位相速度 $c_3=0.55$ m/s で, 水平流速は81, 196m 深に腹, 41, 196, 338m 深に節を持ち, 密度偏差については, 40, 117m 深に腹を持ち, 81, 196m に節を持つことがわかる。Fig. 7 で位相分布を示した30m 深では流速の第1モード, 密度偏差の第3モードの振幅が大きく, 120m 深では流速の第2モード, 密度偏差の第1, 3モードの振幅が大きかった。

これらの鉛直構造を持つ近慣性内部波が富山湾

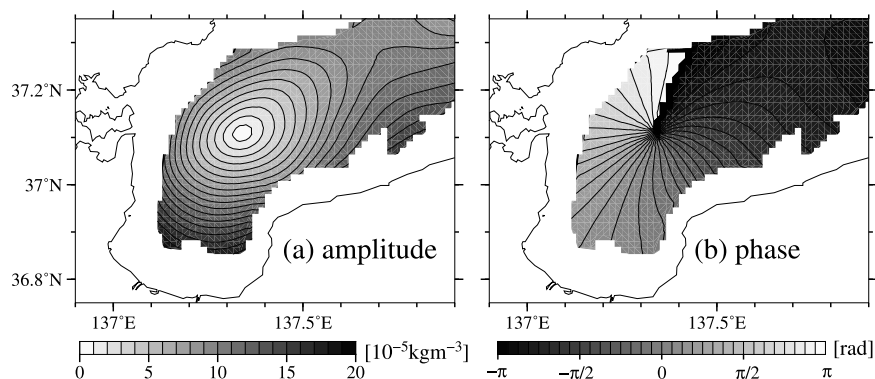


Fig. 10 Horizontal distribution of (a) the amplitude and (b) the phase for the first vertical mode of potential density anomaly.

周辺でどのように分布・伝播していたかを DR_C データから抽出する。各水平グリッドの密度偏差・東西流速・南北流速の 18.5 から 19.5 時間周期のバンドパスフィルターを通したデータに対し、Fig. 9 (c), (d) の鉛直第 1~3 モードの正規化したモードを最小二乗法により当てはめ、各モードの振幅の時系列を見積もり、その時系列データに対して調和解析を用いて近慣性周期変動の振幅と位相を抽出した。ここで、富山湾周辺海域 (Fig. 1 (a) 点線領域) の内部波の特性を見るために計算は水深 800m 以深の海域に限定したので、鉛直モード展開の計算も 800m 以浅とした。表層エクマン層内の風による吹送流を解析の対象外とするため、最小二乗法を用いた当てはめは、20~800m 深の DR_C データとモード型とを用いて行った。

Fig. 10, 11 は、上記手続きから得られた、密度偏差、東西・南北流速を用いて算出した鉛直第 1 モードの振幅と位相の水平分布で、8 月 14 日 3 時を中心とした 5 慣性周期分の結果である。密度偏差に注目すると、振幅は陸棚端付近で最も大きく入善北方に極小点を持ち、位相は対象海域を反時計回りに伝播し、無潮点は振幅の極小点と一致するという特徴を持つ (Fig. 10 (a), (b))。これは、近慣性沿岸捕捉波の伝播の特徴を示す Fig. 6 (f) や Fig. 7 (c) の特徴 (上記 (1)) と良く一致する。ここで、富山湾内における沿岸捕捉波は大陸棚の幅 (約 10km) がロスビーの内部変形半径 (約

20km) に比べて十分小さいため、内部ケルビン波的な特性を持つことが知られている (相木ら, 2006; IGETA *et al.*, 2011) ことから、この解析では、密度振幅に大きなシグナルが現れる内部ケルビン波的な特徴が抽出されたと解釈できる。

一方、流速の東西成分を用いたモード分解の結果からは、鉛直第 1 モードの振幅は、入善沖に極大を持ちつつ放射状に減衰し (Fig. 11 (a))、位相は振幅の極大が分布する入善沖を起点に、東西へ向かって能登半島東岸の海岸線に対して同位相で伝播する (Fig. 11 (b)) 特徴を示している。この特徴は南北流速成分を用いた解析結果 (Fig. 11 (c), (d)) でも確認出来る。これらの結果は、近慣性内部波の発生域が入善沖で、そこから能登半島沿岸へ伝播するという上記の推測をサポートする。

加えて、この海域において沿岸捕捉波が内部ケルビン波的な特性を持つことと、内部ケルビン波の伝播速度は内部重力波と等しい (GILL, 1982) ことを踏まえると、鉛直第 1 モード内部重力波の位相速度より、沿岸捕捉波の波長は約 130km と見積もられる。一方、富山湾奥から入善にかけての凸状の陸岸地形の岸沖方向の空間スケールは約 20km であり、近慣性沿岸捕捉波の波長に比べて十分に小さいと判断されることから、入善沿岸の地形変化で近慣性沿岸捕捉波が散乱することにより近慣性内部波が発生したと考えられる。

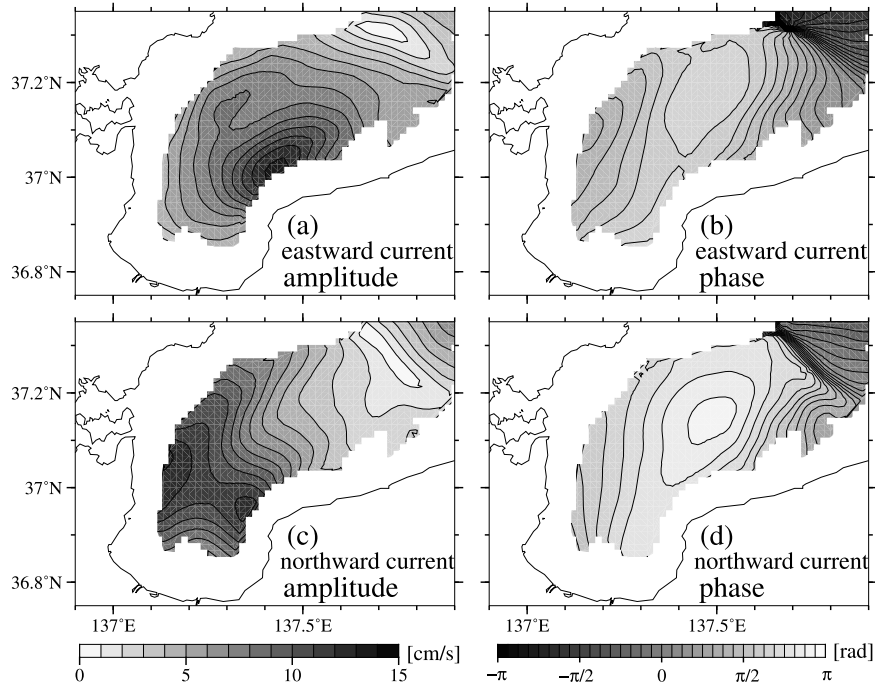


Fig. 11 Same as Fig. 10 but for (a,b) eastward and (c,d) northward current.

以上は、近慣性振動（内部波）が飯田海脚で散乱することで近慣性沿岸捕捉波が発生し、それが鉛直第1モードの内部ケルビン波的な特性を持って能登半島東岸～富山湾を岸沿いに伝播した後、入善沖に入射した際に沿岸の地形の突端部で散乱し、その散乱波の一部が鉛直第1モードの近慣性内部波として能登半島東岸へ伝播した、という一連の近慣性周期変動の伝播過程の推測（上記（2））を支持する結果である。

次に、エネルギー減衰中に流速の時計回り成分が密度変動とは逆に時計回りの位相伝播を示した特徴（Fig. 8, 上記（3））について考察する。Fig. 12はFig. 10, 11と同様の解析を8月16日3時を中心とした5慣性周期分の東西流速データを用いて実施した結果であり、Fig. 8と同じ期間での各鉛直モードの振幅・位相分布を示す。ここから、鉛直第2・3モードが能登半島東岸から北東方向へ位相伝播している様子が明確に確認できる（Fig. 12 (e), (f)）。つまり、Fig. 8に見られた時計回りの位相構造を形成する能登半島東岸で北東

方向へ反射された近慣性内部波は、鉛直第2・3モードで構成されていたことを意味している。一方で、第1モードには、北東方向へ伝播する傾向は見られない（Fig. 12 (d)）。従って、入善沖で発生し、能登半島東岸へ伝播した鉛直第1モードの近慣性内部波は、能登半島東岸の大陸斜面～沿岸域で反射・散乱され、散乱波の一部が鉛直第2・3モードの内部波として北東方向へ伝播した結果、流速の時計回り成分に富山湾を時計回りに位相伝播する構造が形成されたと解釈できる。

ここで、エネルギー減衰期にのみFig. 8 (b)のような伝播様式が現れたことに関しては、入善沖合で発生する近慣性内部波のエネルギーソースである近慣性沿岸捕捉波の振幅が小さくなるのに従い、発生する近慣性内部波の振幅は小さくなる一方で、初期段階に発生・伝播して能登半島東岸沖から北東方向へ反射された近慣性内部波の振幅が相対的に大きくなることによって、そのシグナルが5慣性周期分の代表的な特徴として現れたと考える。

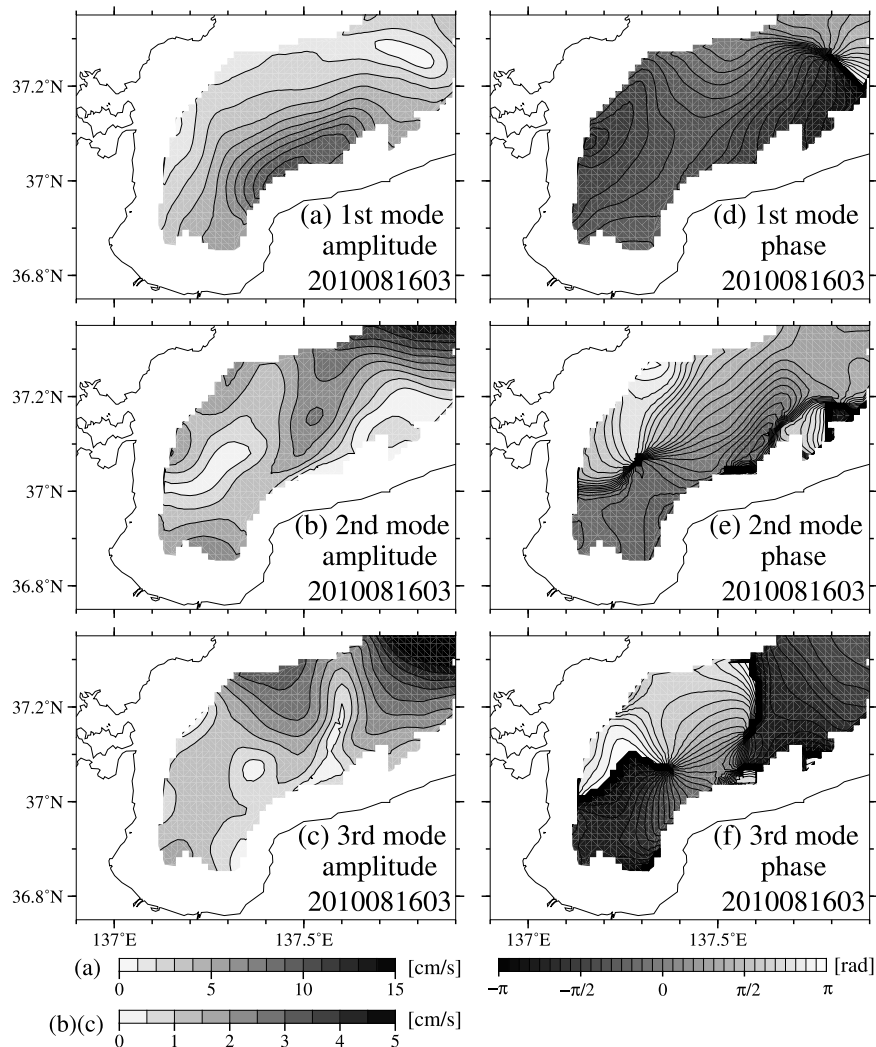


Fig. 12 Horizontal distribution of (a-c) the amplitude and (d-f) the phase for the lowest three vertical modes of eastward current calculated from the data for 95 hours around 3:30, August 16.

4.2 入善沖における近慣性周期変動起源の強流域の形成機構

Fig. 6に見られた近慣性周期変動による入善沖の強流域の形成過程(上記(4))について考察する。入善沖の強流域は、Fig. 6(a), (b)からエクマン層内の6.5m深と季節躍層内の30m深の双方で確認出来るが、6.5m深では強流域の中心が30m深に比べて沿岸に限定される様子が見て取

れる。これは、前述のように入善近傍の凸状の陸岸地形の岸沖方向の空間スケール(約20km)が近慣性沿岸捕捉波の水平スケール(波長約130km)よりも小さいため、沿岸捕捉波による流れが地形によって強制的に収束したことにより、沿岸域の流れが強まったことが成因の一つであると考えられる。

また、Fig. 7(c)から近慣性沿岸捕捉波の発生

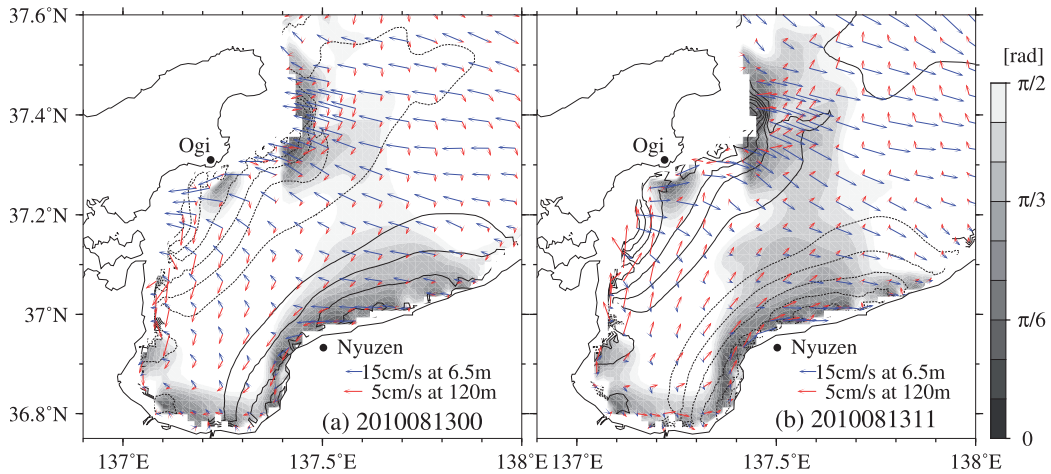


Fig. 13 Density anomaly at the depth of 120 m (contour line), current velocity at the depth of 120m (red vector) and 6.5m (blue vector), and difference of current angle between the depth of 120m and 6.5m (grayscale) at the time (a) trough and (b) crest of coastal trapped wave were located around Nyuzen. Solid and dashed lines represent a positive and negative anomaly, respectively. Contour intervals of density anomaly are every $2 \times 10^{-5} \text{kgm}^{-3}$.

源である飯田海脚周辺海域と、入善沖との位相差は約 π であることがわかる。これは、近慣性沿岸捕捉波由来の流れが、飯田海脚周辺海域で岸を右に見る流れの最大値を持つ時刻に、入善沖では岸を左手に見る流れの最大値を持つことを意味する。Fig. 13に沿岸捕捉波の峰と谷が入善近傍に分布した時刻のエクマン層内の流れ(6.5m深)と近慣性沿岸捕捉波由来の流れ(120m深)のベクトルとその流向差の絶対値を示した。飯田海脚周辺と入善沿岸の海岸線は概ね平行することから、鉛直第1モードの近慣性沿岸捕捉波由来の流れは、飯田海脚近傍と入善沿岸一帯とで、南西—北東方向で概ね類似した方向を向くこととなる(Fig. 13, 120m深ベクトル)。一方、エクマン層内の流れは基本的に慣性振動の運動形態を持っており、沿岸付近で岸に沿う流れになる傾向を除けば、空間構造に乏しいため、飯田海脚周辺と入善沿岸一帯とで概ね類似した方向を向く(Fig. 13, 6.5m深ベクトル)。この近慣性沿岸捕捉波由来の流れと慣性振動由来の流れとの関係を見ると、入善沖で流れの向きがほぼ一致することが分かる(Fig. 13, グレースケール)。このことから、入善

沖の表層では、海岸線の水平的な変化による流れの収束に加え、近慣性沿岸捕捉波の流れを慣性振動が共鳴的に強めることで、非常に強い近慣性周期の振動流が起きることが分かった。

5. まとめ

本研究は、短周期変動を対象とした予測計算を現業運用している高解像度海洋予測モデルの確定値を用いて、HIROSE *et al.* (2017)で流動変動の再現性の高さが確認されている台風1004号に伴う事例を対象に、近慣性内部波の富山湾周辺海域における振る舞いを調べた。その結果、以下のことが分かった(括弧内に特徴が現れている代表的な図を示す)。

- (1) 慣性振動が能登半島北東端の浅瀬近傍で散乱することで近慣性沿岸捕捉波が発生し、それが能登半島東岸～富山湾へ伝播する。(Fig. 6 (f), Fig. 10)
- (2) 沿岸捕捉波が入善沖へ達した際に凸状の地形で散乱し、それにより発生した近慣性内部波が能登半島東岸へ伝播する。(Fig. 11)
- (3) (2)の近慣性内部波は能登半島東岸一帯に同

位相の流速振動を形成した後北東方向の沖合へ反射される。(Fig. 11 (b), (d), Fig. 12 (e), (f))

(4) 入善沖に近慣性振動流の強流帯が形成される。(Fig. 6 (a), (b))

(1) の結果、密度偏差には反時計回りの位相分布、(2)・(3) の結果、流速変動には時計回りの位相分布が形成され、流速と密度偏差の位相分布に相違が生まれた。ここで、近慣性内部波が発生する入善沖では、流れが非常に大きくなっていた。これは、能登半島北東部から入善沖までの距離が、近慣性沿岸捕捉波の半波長分の長さとはほぼ一致しているために、入善沖での近慣性沿岸捕捉波起源の流れが、慣性振動起源の流れを強めたことが原因であると考えられた。

上記 (1) ~ (3) は近慣性内部波の波面が能登半島東岸の表層へ平行に入射し、東岸域一帯に同時多発的 (同位相) に近慣性振動流を励起する可能性を示す。この結果は大慶ら (2015) による観測結果と整合的である。当該海域の急潮と呼ばれる沿岸強流現象は、沿岸捕捉波や沿岸密度流などの岸を右に見て伝播する物理現象で解釈が試みられてきた。その際に、各地で観測された流速データのピークを用いて計算した伝播速度が非常に速く、沿岸捕捉波、沿岸密度流で解釈できない場合は、本研究で見られるような近慣性内部波のシグナルが混在している可能性がある。

急潮防災という観点では、強流を引き起こす現象が岸伝いに伝播するのか、沖合から波及するののかという問題は重要である。能登半島東岸では北から順に沿岸で強流が起きるのか、同時多発的に起きるのかという違いに繋がるからである。つまり、沿岸捕捉波、沿岸密度流、近慣性内部波のどれが卓越するかを定量的に理解する必要があるということになる。前者に寄与する南風の連吹と、後者に寄与する風ベクトルの時計回り成分 (近慣性周期変動エネルギーの海洋への注入の見積もり) に注目して事例解析を進めていく必要があるだろう。

能登半島東岸域へ近慣性内部波のエネルギーがどの程度到達するかを理解することも重要で、こ

れは本稿では言及できなかった。今後、鉛直高次モードの近慣性内部波が乗り上げやすい成層条件・海域について理想化した実験を行うことで理解する必要があるだろう。また、本研究からは入善沿岸で近慣性周期流速変動が特異的に強化される可能性が示された。この流れの強化機構を元に考えると、近慣性沿岸捕捉波の伝播速度が成層条件の変化に伴い遅くもしくは速くなることで、慣性振動による流速変動と位相が一致する海域が東西にシフトする可能性がある。当該海域における流動観測データの解析や流動構造の鉛直構造の観測等を進め、流速強化機構のさらなる理解を進める必要があるだろう。

謝辞

本研究は、文部科学省気候変動適応技術社会実装プログラム(SI-CAT)の支援により実施された。風速、台風経路は、それぞれ気象庁のMSM-GPVデータ、バストトラックデータに拠った。図の作成にはgnuplot, Generic Mapping Tool (GMT)を使用した。ここに記して感謝の意を表す。また、本論文に対してコメントを頂きました査読者の方にお礼申し上げます。

付録 A: 回転スペクトル

流速の回転成分のエネルギーを見積もるために、次式 (日野, 1977) により回転スペクトルを算出した。

$$S_{-}(\sigma) = \frac{2\pi}{T} \langle Z_{-}^{*}(\sigma) Z_{-}(\sigma) \rangle \quad (\text{A1a})$$

$$S_{+}(\sigma) = \frac{2\pi}{T} \langle Z_{+}^{*}(\sigma) Z_{+}(\sigma) \rangle \quad (\text{A1b})$$

T は周期、 σ は正の角周波数である。 Z_{-} 、 Z_{+} は複素数表示した流速ベクトル時系列 $z(t)$ の複素フーリエ係数で、

$$z(t) = u(t) + iv(t) \equiv \frac{1}{2\pi} \int_0^{\infty} \{Z_{+}(\sigma)e^{i\sigma t} + Z_{-}(\sigma)e^{-i\sigma t}\} d\sigma \quad (\text{A2})$$

によって定義される。 $|Z_{+}(\sigma)|$ 、 $|Z_{-}(\sigma)|$ はそれぞれ反時計回り、時計回りの円運動の半径に相当する。 Z_{-} 、 Z_{+} は流速の東西成分 u 、南北成分 v

$$u(t) = \frac{1}{2\pi} \int_0^\infty \{a_1(\sigma) \cos \sigma t + b_1(\sigma) \sin \sigma t\} d\sigma \quad (A3a)$$

$$v(t) = \frac{1}{2\pi} \int_0^\infty \{a_2(\sigma) \cos \sigma t + b_2(\sigma) \sin \sigma t\} d\sigma \quad (A3b)$$

のフーリエ係数 a_1 , b_1 , a_2 , b_2 を使って次式によって表される。

$$Z_+(\sigma) = \frac{1}{2} \{ (a_1(\sigma) + b_2(\sigma)) + i (a_2(\sigma) - b_1(\sigma)) \} \quad (A4a)$$

$$Z_-(\sigma) = \frac{1}{2} \{ (a_1(\sigma) - b_2(\sigma)) + i (a_2(\sigma) + b_1(\sigma)) \} \quad (A4b)$$

時計回りと反時計回りのどちらの成分が卓越しているかについては、回転係数 $C_R(\sigma) = \{S_-(\sigma) - S_+(\sigma)\} / \{S_-(\sigma) + S_+(\sigma)\}$ によって与えられる。 $C_R(\sigma) = 1$, $C_R(\sigma) = 0$ は複素ベクトル $z(t)$ が、それぞれ真円、直線上の軌道を指して運動することを表している。

付録 B: 鉛直モード展開

富山湾周辺海域での密度成層の平均場における内部波の鉛直固有モードを次のように算出した。密度平均の領域は Fig. 1 の点線領域内で 800m 深以上の海底水深がある場所とした。800m という水深は、平均領域に富山湾を含めることと、密度の鉛直変化が小さく浮力振動数がゼロに近い水深である (Fig. 9 (b)) という理由から選んだ。また、1000m 深で算出した場合と比べて第 1 モードの節の位置が鉛直グリッドの 1 グリッド分程度であったので、水深を 800m と仮定することは解析結果に大きな影響は無いと判断した。

ブシネスク近似と静水圧近似を仮定した非粘性成層流体の線形基礎方程式より、鉛直流 w に関する式は次のように与えられる (北出, 1994; KUNDU, 1990)。

$$\left(\frac{\partial^2}{\partial t^2} + f^2 \right) \frac{\partial^2 w}{\partial z^2} + \left(\frac{\partial^2}{\partial t^2} + N^2 \right) \left(\frac{\partial^2 w}{\partial x^2} + \frac{\partial^2 w}{\partial y^2} \right) = 0 \quad (B1)$$

f はコリオリパラメータ、 N は浮力振動数で $N^2 = -\frac{g}{\rho_0} \frac{\partial \rho_0}{\partial z}$ と定義される。 g は重力加速度、 ρ_0

は基本場の密度である。式 (B1) に対し、変数分離解

$$w = \hat{\varphi}(z) \bar{w}(x, y) e^{-i\sigma t} \quad (B2)$$

を仮定すると、 $\hat{\varphi}(z)$ に関する 2 階の同次線形微分方程式が次のように得られる。

$$\frac{d^2 \hat{\varphi}(z)}{dz^2} + \frac{N^2 - \sigma^2}{c_e^2} \hat{\varphi}(z) = 0 \quad (B3)$$

ここで c_e^2 は分離定数で、等価水深 H_e により、 $c_e^2 = \sqrt{gH_e}$ と表せる。同様にして圧力偏差 p' 、密度偏差 ρ' 、東西流速 u についても変数分離解を仮定することで、鉛直成分のみに関する方程式

$$\hat{\rho}' = \hat{\varphi} \frac{d\rho_0}{dz} \quad (B4)$$

$$\hat{u}(z) = \frac{\hat{p}}{\rho_0 g} = \frac{c_e^2}{g} \frac{d\varphi}{dz} \quad (B5)$$

が得られる。

2 階の同次線形微分方程式 (B3) を境界条件 $\varphi_n(z=0)=0$, $\varphi_n(z=-H)=0$, $H=800\text{m}$ の下で、Dirichlet 問題として shooting 法によって解き (GILL, 1982), 求めた鉛直 n 次モードの固有値 c_n から固有関数 $\hat{\varphi}_n$ を算出した。ここで、 H は平均水深である。また、固有値 c_n は鉛直 n 次モードの内部重力波の位相速度に対応する。求めた固有関数 $\hat{\varphi}_n$ を (B4), (B5) 式に用いて、各鉛直モードの密度偏差 $\hat{\rho}'_n(z)$ 、水平流速 $\hat{u}_n(z)$ について鉛直プロファイルを算出した。

引用文献

- 相木智一, 磯田豊, 小善圭一 (2006): 富山湾における数日周期の風強制流速変動. 北海道大学水産科学研究彙報, **57** (1・2), 9-18.
- 浅勇輔, 広瀬直毅, 千手智晴 (2007): 能登半島東岸において 2004 年に発生した急潮の数値実験. 海の研究, **16** (1), 39-50.
- DALE, A. C., J. M. HUTHNANCE AND T. J. SHERWIN (2001): Coastal-Trapped Waves and Tides at Near-Inertial Frequencies. Journal of Physical Oceanography, **31**, 2958-2970.
- D'ASARO, E.A., (1985): The energy flux from the wind to near-inertial motions in the surface mixed layer. Journal of Physical Oceanography, **15**, 1043-1059.

- FUKUDOME, K., Y. IGETA, T. SENJYU, N. OKEI AND T. WATANABE (2016): Spatiotemporal current variation of coastal-trapped waves west of the Noto Peninsula measured by using fishing boats. *Continental Shelf Research*, **115**, 1–13.
- GARRETT, C. (2001): What is the “near-inertial” band and why is it different from the rest of the internal wave spectrum?. *Journal of Physical Oceanography*, **31**, 962–971.
- GILL, A. E. (1982): *Atmosphere-Ocean Dynamics*, Academic Press, 662pp.
- GILL, A. E. (1984): On the behavior of internal waves in the wakes of storms. *Journal of Physical Oceanography*, **14**, 1129–1151.
- 日野幹雄 (1977): *スペクトル解析*. 朝倉書店, 300pp.
- HIROSE, N., K. TAKAYAMA, J.-H. MOON, T. WATANABE AND Y. NISHIDA (2013): Regional Data assimilation System extended to the East Asian Marginal Seas. *海と空*, **89**, 43–51.
- Hirose, N., Y. Kumaki, A. Kaneda, K. Ayukawa, N. Okei, S. Ikeda, Y. Igeta and T. Watanabe (2017): Numerical simulation of the abrupt occurrence of strong current in the southeastern Japan Sea. *Continental Shelf Research*, **143**, 194–205.
- IGETA, Y., Y. KITADE AND M. MATSUYAMA (2007): Numerical experiment on Kyucho around the Tango Peninsula induced by Typhoon 0406. *Journal of Oceanography*, **63**, 835–847.
- IGETA, Y., Y. KUMAKI, Y. KITADE, T. SENJYU, H. YAMADA, T. WATANABE, O. KATOH AND M. MATSUYAMA (2009): Scattering of near-inertial internal waves along the Japanese coast of the Japan Sea. *Journal of Geophysical Research: Oceans*, **114**, C10002.
- IGETA, Y., T. WATANABE, H. YAMADA, K. TAKAYAMA AND O. KATOH (2011): Coastal currents caused by superposition of coastal-trapped waves and near-inertial oscillations observed near the Noto Peninsula, Japan. *Continental Shelf Research*, **31**, 1739–1749.
- IGETA, Y., A. YANKOVSKY, K. FUKUDOME, S. IKEDA, N. OKEI, K. AYUKAWA, A. KANEDA, AND T. WATANABE (2017): Transition of the Tsushima Warm Current Path Observed over Toyama Trough, Japan. *Journal of Physical Oceanography*, **47**, 2721–2739.
- 北出裕二郎 (1994): 相模湾周辺海域における内部潮汐の発生と伝播に関する研究. 東京水産大学, 博士論文.
- KUNDU, P. K. (1984): Generation of coastal inertial oscillations by time-varying wind, *Journal of Physical Oceanography*, **14**, 1901–1913.
- KUNDU, P. K. (1990): *Fluid Mechanics*. Academic Press, 638pp.
- LEE, H. J., J.-H. YOON, H. KAWAMURA AND H.-W. KANG (2003): Comparison of RIAMOM and MOM in modeling the East Sea/Japan Sea circulation. *Ocean Polar Res.*, **25**, 287–302.
- 大慶則之, 奥野充一, 千手智晴 (2009): 気象擾乱通過後に能登半島沿岸で観測された急潮. *海の研究*, **18**, 57–69.
- 大慶則之, 奥野充一, 辻俊宏, 千手智晴 (2012): 能登半島周辺に急潮を引き起こす気象条件の特徴の解明 – 急潮防災を目指して. *水産海洋研究*, **76** (3), 131–140.
- 大慶則之, 奥野充一, 辻俊宏, 千手智晴 (2015): 能登半島東岸で2004年秋季に観測された大規模強流反復現象. *海の研究*, **24** (4), 133–146.
- 山崎恵市, 北出裕二郎, 井桁庸介, 渡邊達郎, 千手智晴, 山田東也, 大慶則之, 池田怜 (2015): 能登半島北東端沖で観測された近慣性内部波. *海の研究*, **24** (6), 203–226.
- WATANABE, M. AND T. HIBIYA (2018): A near-inertial current event in the homogeneous deep layer of the northern Sea of Japan during winter, *Journal of Oceanography*, **74**, 209–218.
- WILKIN, J. L., D. C. CHAPMAN (1990): Scattering of Coastal-Trapped Waves by Irregularities in Coastline and Topography. *Journal of Physical Oceanography*, **20**, 396–421.

受付: 2018年8月29日

受理: 2018年12月25日

A note on the abyssal circulation in the Japan Sea: suggestion from rotating-tank experiments

Tomoharu SENJYU¹⁾ and Jiro YOSHIDA²⁾

Abstract: In this study, we revisited the rotating-tank experiments reported by FALLER (1960) and SENJYU (1988) and qualitatively discussed the abyssal circulation in the Japan Sea by focusing on the geometric similarity of their partial barrier experiments. A point source of water near the apex of the pie-shaped rotating-tank formed the so called STOMMEL-ARONS type circulation pattern. The circulation in the partial barrier experiments basically consisted of a cyclonic circulation and a western boundary current in the southern two basins separated by a partial barrier extending from the rim. Recent observations on direct current in the abyssal Japan Sea have revealed a cyclonic circulation and strong currents near the western boundary in the southern two basins: the Yamato and Tsushima Basins. These similarities suggest the STOMMEL-ARONS type circulation in the abyssal Japan Sea, though the complex bottom topography and eddy activity are likely to modify the basic circulation pattern significantly.

Keywords : *Rotating-tank experiment, deep circulation, deep western boundary current, direct current observation*

1. Introduction

The oceanic abyssal circulation is one of the most important parts of the global climate system, which transports cold deep water in a high-latitude region to low-latitude areas. During the course of this circulation, cold water gradually upwells and eventually returns to the high-

latitude region by the surface currents. Therefore, abyssal circulation bears the lower part of the meridional overturning or thermohaline circulation (TALLEY *et al.*, 2011).

The first dynamic model of the global abyssal circulation was presented by STOMMEL (1958) and STOMMEL and ARONS (1960a, b). Their basic concept of the global abyssal circulation (hereafter, the SA-type circulation) is as follows: the volume of cold water sunken in the high-latitude regions (the northern North Atlantic and the Antarctic) is compensated by the upwelling over the world ocean. The vertical velocity (w , positive upward) accompanied by the upwelling induces positive (negative) relative vorticity through stretching of water column ($f\partial w / \partial z$, where f is the planetary vorticity) in the north-

-
- 1) Division of Earth Environment Dynamics, Research Institute for Applied Mechanics, Kyushu University
6-1 Kasuga-Koen, Kasuga City, Fukuoka 816-8580, Japan
E-mail: senjyu@riam.kyushu-u.ac.jp
 - 2) Tokyo University of Marine Science and Technology
4-5-7 Konan, Minato, Tokyo 108-8477, Japan
E-mail: jiroy@kaiyodai.ac.jp

ern (southern) hemisphere. Since, in the steady state, the relative vorticity must be balanced by the advection of planetary vorticity (βv , where β and v denote meridional derivation of f (df/dy) and meridional geostrophic velocity positive northward, respectively) to conserve potential vorticity, poleward flow appears over the interior region of each oceanic basin. To satisfy the condition of continuity, a western boundary current (WBC) is introduced toward low latitude in each basin. The basic characteristics of the SA-type circulation in the oceans, such as the deep WBC, have been validated by many researchers by using chemical tracers and neutral drifters (e.g., BROECKER and PENG, 1982; SWALLOW and WORTHINGTON, 1961).

The concept of the SA-type circulation was initiated from a rotating-tank experiment with a point source of water (STOMMEL *et al.*, 1958). Because this experiment was very simple, additional experiments were performed to examine several conditions appearing in the real ocean, for example lateral boundary (FALLER, 1960; SENJYU 1988), bottom topography (WELANDER, 1969; KUO and VERONIS, 1971), and nonlinear effects (VERONIS and YANG, 1972). In this study, we revisit the partial barrier experiments by FALLER (1960) and SENJYU (1988) and discuss the deep circulation in the Japan Sea by referring to the results of the rotating-tank experiments.

The Japan Sea has its own thermohaline circulation system with the formation of deep and bottom waters (hereafter, the Japan Sea Proper Water) which were surface water sunken in the northwestern part of the sea, south of Vladivostok (Fig. 1) (GAMO and HORIBE, 1983; SUDO, 1986; SENJYU and SUDO, 1993 & 1994; SENJYU *et al.*, 2002). In addition, the Japan Sea has southern and northern surface circulations with a WBC (the East Korean Current in the south and the Liman Current in the north) bounded by a sub-

arctic front, similar to the subtropical and subarctic gyres in the Pacific and Atlantic oceans. This indicates that the planetary β -effect is substantially important for basin-scale circulation in the sea. These conditions make us expect the SA-type circulation in the abyssal Japan Sea. Furthermore, the bottom topography of the Japan Sea (Fig. 1) is similar to the geometry of the partial barrier experiment (Fig. 2); a northern basin N corresponds to the Japan Basin, and two southern basins SW and SE correspond to the Yamato and Tsushima Basins, respectively. These two basins are bounded by a shallow ridge extending from the Oki Islands to the Yamato Rise (the Oki Spur), as well as its closed configuration.

In the next section, we describe the principle and method involved in the rotating-tank experiments referring to results of the test experiments of the SA-type circulation. Section 3 introduces some results of the partial barrier experiments by SENJYU (1988) weighted on the change of flow pattern when the length and angle of the partial barrier were varied. Section 4 provides a qualitative discussion about the Japan Sea deep circulation using the analogy of the partial barrier experiments. Finally, Section 5 presents concluding remarks.

2. Test experiments of the SA-type circulation

Prior to the partial barrier experiments, SENJYU (1988) performed a series of test experiments of the STOMMEL *et al.*'s (1958) SA-type circulation. In this section, the principle and method of the experiments are explained referring to the results of the test experiment.

A pie-shaped tank (Fig. 2, but without the partial barrier) containing water was set on a turntable and was rotated anticlockwise with respect to the vertical axis at a constant angular velocity (ω). Since the spin-up time scale $t_s = (h^2$

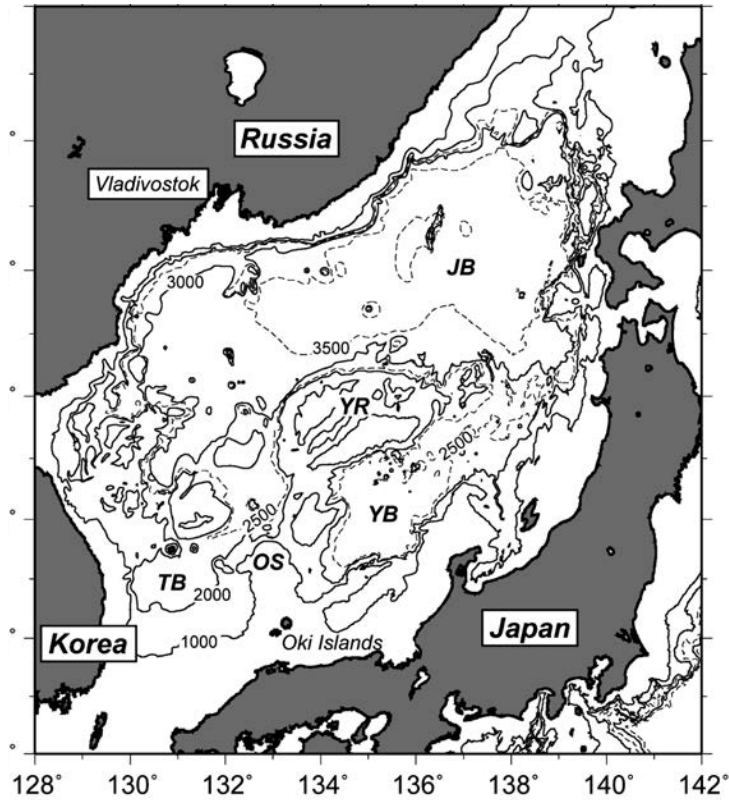


Fig. 1 Bottom topography of the Japan Sea. *JB*, *YB*, *TB*, *YR*, and *OS* denote the Japan Basin, Yamato Basin, Tsushima Basin, Yamato Rise, and Oki Spur, respectively.

$/\nu\omega)^{1/2}$ was estimated to be about 100 s using the water depth $h \sim O(10 \text{ cm})$, viscosity $\nu \sim O(10^{-2} \text{ cm}^2 \text{ s}^{-1})$, and $\omega \sim O(1 \text{ rad s}^{-1})$, each experiment was started after an hour rotation (rigid-body rotation).

After achieving the rigid-body rotation state, a small volume of dyed water was constantly injected into the tank from a point source near the apex of the sector (S_0), which corresponds to a narrow source region of the deep water in the real ocean. For the dyeing of water, a small volume of brilliant-blue was used. To minimize the density difference between waters in the tank and for the injection, the waters were put in the same environment at least 12-h long before each

experiment. At last, the smallness of the density difference was confirmed by vertical rigidity of the injected water during the experiments, that is, whether the injected water forms a TAYLOR'S ink wall or not (*e.g.*, Long, 1954).

The outlet of the dyed water was set at 1.0–1.5 cm below the water surface under the Ekman layer; the thickness of the Ekman layer is $\delta_E = (\nu / 2\omega)^{1/2} \sim O(10^{-1} \text{ cm})$, if we adopt the above values of ν and ω . In addition, the tank was covered with a clear acrylic lid to escape air stress on the water surface. The flow pattern in the tank visualized by the dyed injected water was recorded by a camera installed on the turntable.

The water level before the start of rotation

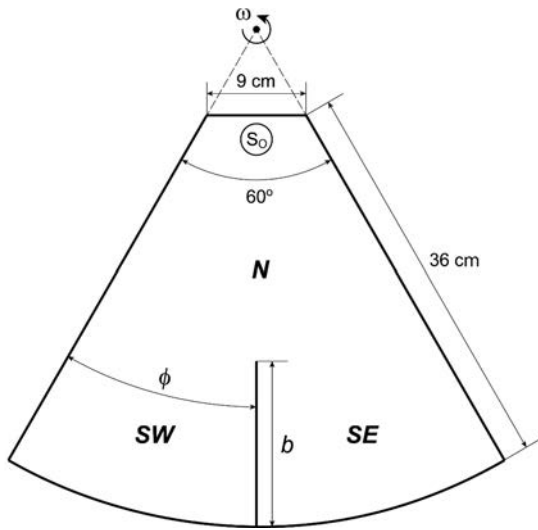


Fig. 2 Dimension of the experiment tank. *N*, *SW*, and *SE* indicate three basins separated by a partial barrier of length b and angle ϕ from the western boundary. S_0 is a point source of water. The tank is rotating anticlockwise at an angular velocity ω with respect to the vertical axis.

was set at 8.3 cm. However, the free surface of water during the experiments is a paraboloidal shape, with a minimum at the apex and a maximum at the rim, because of the balance of pressure gradient and centrifugal force. The planetary β -effect is approximately simulated by the radial variation of the water depth ($\beta \approx -2\omega (dh/dr)/h_0$, where r denotes the radial distance from the rotating axis and h_0 is the water depth at $r = 0$). Hence, the apex side (rim side) of the tank corresponds to the north (south) in the real ocean, and thus, we use the words “north”, “south”, “east”, “west”, and so on to show the direction.

Since there is no sink of water in the tank, the water surface slowly rises with time in the experiments, which simulates the upwelling in the interior region of the real ocean, although STOMMEL and ARONS (1960a, b) assumed the

steady state condition. This temporal change of the water level influences the planetary β -effect via the relation $\beta \approx -2\omega (dh/dr)/h_0(t)$, now h_0 is a function of time t . The injection rate of water was set at about $1.0 \text{ cm}^3 \text{ s}^{-1}$, and the duration of an experiment was about 30 min. Therefore, the volume of injected water at the end of the experiment reached 1800 cm^3 . Since the area of the tank is 1025.2 cm^2 , the difference of water level before and after the experiment was about 1.8 cm. This corresponds 23% of the initial water depth at the rotating axis ($h_0(0) = 7.8 \text{ cm}$). Therefore, we should keep on mind the fact that the β -effect was reducing by about 20% during the experiment.

Figure 3 shows time sequence of a test experiment. A clockwise eddy near the point source grew gradually (Fig. 3a-b), then a narrow and fast flow along the western boundary (the WBC) appeared from the eddy (Fig. 3c-d). The dyed water flowed eastward along the southern boundary accompanying a wide but sluggish northward flow (the interior flow) after arriving at the rim (Fig. 3e-g), finally a westward intensified cyclonic gyre (the SA-type circulation) was confirmed (Fig. 3h).

STOMMEL *et al.* (1958) set the ROSSBY number $R_o = V/(2R\omega)$ (V is the representative speed of the WBC and R is the distance from the rotating axis to the rim of the tank, 45 cm) to be $O(10^{-3})$, the same order of magnitude as that for the Gulf Stream system. However, SENJYU (1988) adjusted $R_o \sim O(10^{-2})$ due to the limit of the experimental equipment. The speed of the WBC tended to increase with increasing angular velocity (ω) and increasing injection rate (S_0). Therefore, SENJYU (1988) carefully checked the speed of the WBC in the test experiments and determined the ranges of ω and S_0 for the partial barrier experiments in the next section.

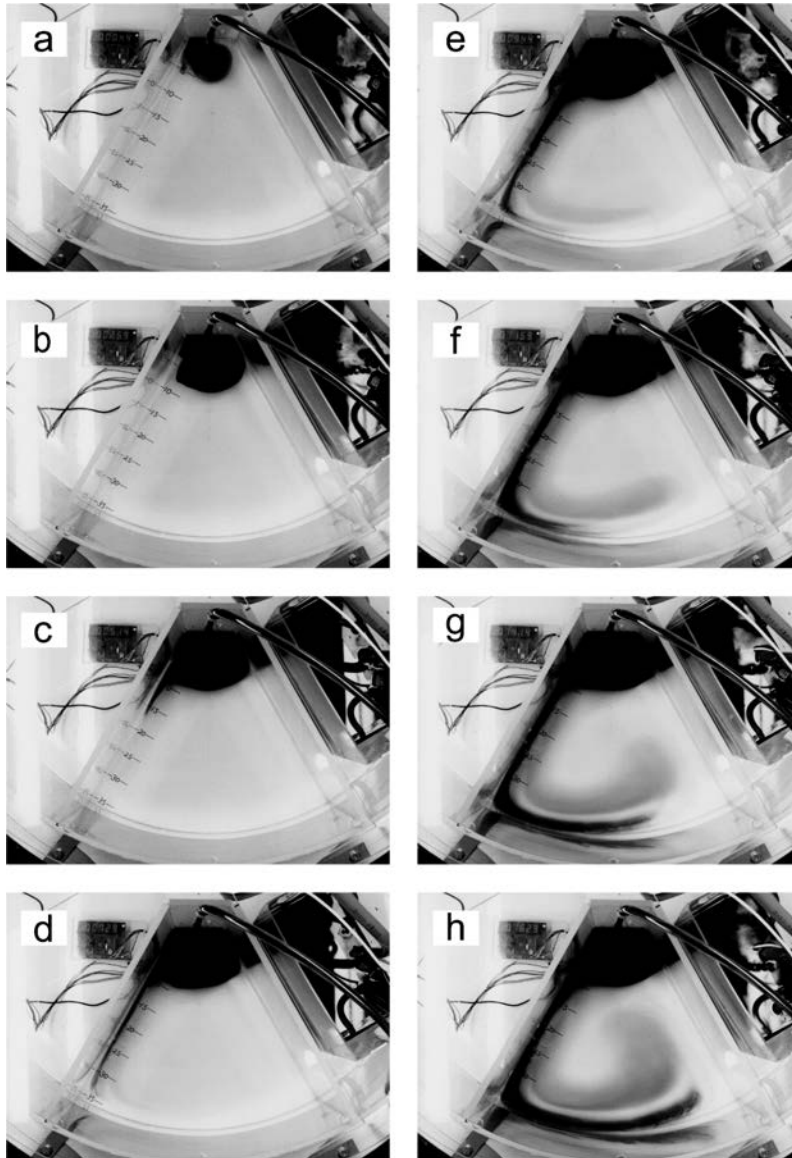


Fig. 3 Results of a test experiment for the SA-type circulation ($S_0 = 1.5 \text{ cm}^3 \text{ s}^{-1}$, $\omega = 0.79 \text{ rad s}^{-1}$). The photos show the distribution of dyed water at (a) 44 s (0.73 min), (b) 259 s (4.32 min), (c) 514 s (8.67 min), (d) 729 s (12.15 min), (e) 944 s (15.73 min), (f) 1159 s (19.32 min), (g) 1414 s (23.57 min), and (h) 1629 s (27.15 min) from the start of experiment.

3. Partial barrier experiments

For the partial barrier experiments, a meridional (radial) barrier extending from the rim (a

flat acrylic board of 4 mm thickness) was attached in the tank in order to divide the sector into three basins: *N*, *SW*, and *SE* (Fig. 2). The

Table 1. Parameters for the partial barrier experiments

	S_O ($\text{cm}^3 \text{s}^{-1}$)	b (cm)	$B (= b/36 \text{ cm})$	ϕ ($^\circ$)	ω (rad s^{-1})
Exp 1	0.2	15	0.42	30	0.79
Exp 2	0.5	15	0.42	30	0.79
Exp 3	1.0	15	0.42	30	0.79
Exp 4	1.5	15	0.42	30	0.79
Exp 5	1.0	10	0.28	30	0.79
Exp 6	1.0	20	0.56	30	0.79
Exp 7	1.0	15	0.42	20	0.79
Exp 8	1.0	15	0.42	40	0.79
Exp 9	1.0	15	0.42	30	0.70
Exp 10	1.0	15	0.42	30	0.90

experimental parameters were length of the barrier (b) (we use a non-dimensional length scale B which is the barrier length normalized by the radial extent of the tank, 36 cm) and angle of the barrier from the western boundary (ϕ), as well as injection rate of water at the point source (S_O) and angular velocity (ω) (Table 1). Basically, the changes of injection rate (Exps 1-4) and angular velocity (Exps 3 and 9-10) did not change the pattern of circulation. On the contrary, significant changes in flow pattern were observed depending on the length (Exps 3, 5-6) and the angle of the meridional barrier (Exps 3, and 7-8). Therefore, we show the results of Exps 3 and 5-8 below because our interest is how the SA-type circulation pattern in the previous section was modified by the partial barrier.

Firstly, the results of Exp 3 (the reference experiment) are shown in Fig. 4 using streak lines of the dyed injected water. In the first stage, the injected water formed a clockwise eddy of 12-15 cm diameter near the point source (1-3 min after the injection). Then, a narrow and fast flow along the western boundary appeared (4-5 min). We call this flow the WBC-N as this is the WBC in the N -basin. The WBC-N flowed into the SW -basin along the western boundary as the WBC-SW (6-7 min). The dyed water flowed eastward along the southern boundary accompanying

northward flow component after arriving at the rim (8-16 min). The northward interior flow was wider but much slower than the WBC-SW. At this time, a westward intensified cyclonic gyre was confirmed in the SW -basin. Part of the northward flow turned to the east at the tip of the meridional barrier, then flowed into the SE -basin forming a WBC (the WBC-SE) (17-20 min). The water arrived at the rim in the SE -basin flowed along the southern boundary accompanying weak northward component, showing a cyclonic gyre similar to that in the SW -basin (21-27 min).

A clear cyclonic gyre was formed in both the SW and SE -basins even when the length of the barrier was changed (Figs. 4 and 5). However, in the case of Exp 5, the WBC-SE was significantly broad and the westward intensification in the SE -basin did not fully develop (Fig. 5a), though a similar westward intensified gyre was formed in the SW and SE -basins in Exps 3 and 6 (Figs. 4 and 5b). This suggests that the short barrier in Exp 5 did not work as a barrier. The circulation pattern possibly approaches the SA-type circulation in Fig. 3 with decreasing the length of the barrier. Contrary, water of the WBC-SE was directly supplied from the clockwise eddy at the point source in Exp 6 (Fig. 5b) as the tip of the barrier is near the source region.

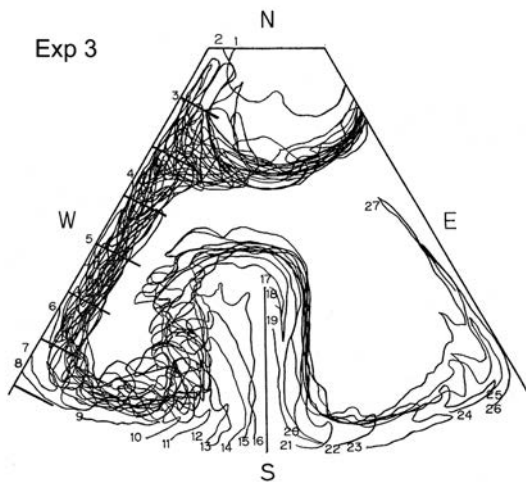


Fig. 4 Flow pattern of Exp 3 (the reference experiment) visualized by the dyed water. The contours indicate streak of the injected dyed water every 1 min. Numerals show the elapsed time from the start of the experiment (min). The ruler on the western boundary is graduated at 5 cm.

In Exps 3 and 8, clear cyclonic gyre was formed in both the *SW* and *SE*-basins (Figs. 4 and 6b). In contrast, the gyre in the *SW*-basin was obscure in Exp 7, though a cyclonic gyre was found in the *SE*-basin (Fig. 6a). A reason for the obscure gyre in the *SW*-basin is that a zonal

flow toward the *SE*-basin was separated from the WBC-N at 4–5 min and fed the WBC-SE together with the northward flow in the *SW*-basin. The volume of southward-flowing WBC equals the sum of the zonally-integrated northward interior flow and the volume of upwelling over the basin. Therefore, the volume of WBC-SE is larger than that of WBC-SW in Exp 7. In order to feed the larger volume of WBC-SE, the zonal flow was separated from the WBC-N. However, crossing of the zonal flow with the northward internal flows in the *SW*-basin disturbed the streak of dyed water, which resulted in the obscure gyre pattern in the basin.

4. Discussions

As pointed out earlier, the geometry of the partial barrier experiment is similar to the topography of the Japan Sea (Figs. 1 and 2). The *N*, *SW*, and *SE*-basins correspond to the Japan, Tsushima, and Yamato Basins, respectively. The meridional barrier coincides with the Yamato Rise and Oki Spur. In addition, the formation region of the Japan Sea Proper Water located on the northwestern Japan Basin (SENJYU and SUDO, 1993 & 1994; SENJYU *et al.*, 2002) agrees with the

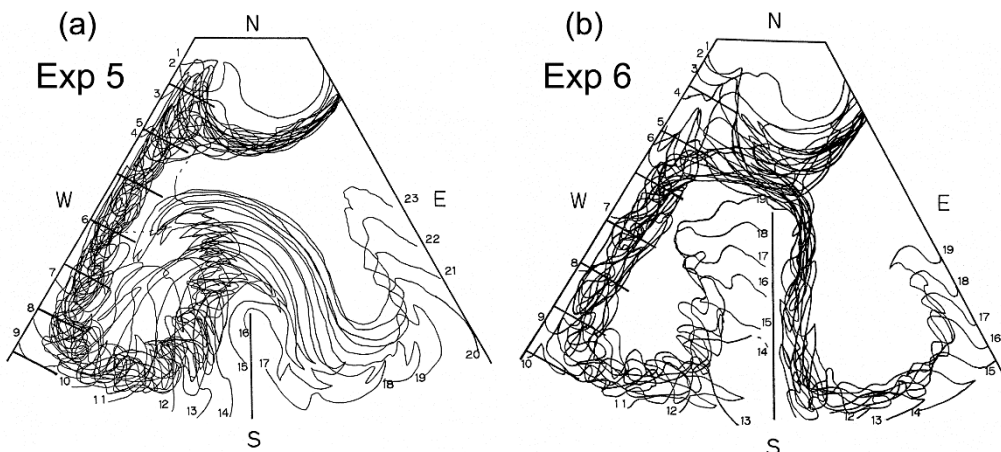


Fig. 5 Same as Fig. 4 except for Exp 5 (a) and Exp 6 (b).

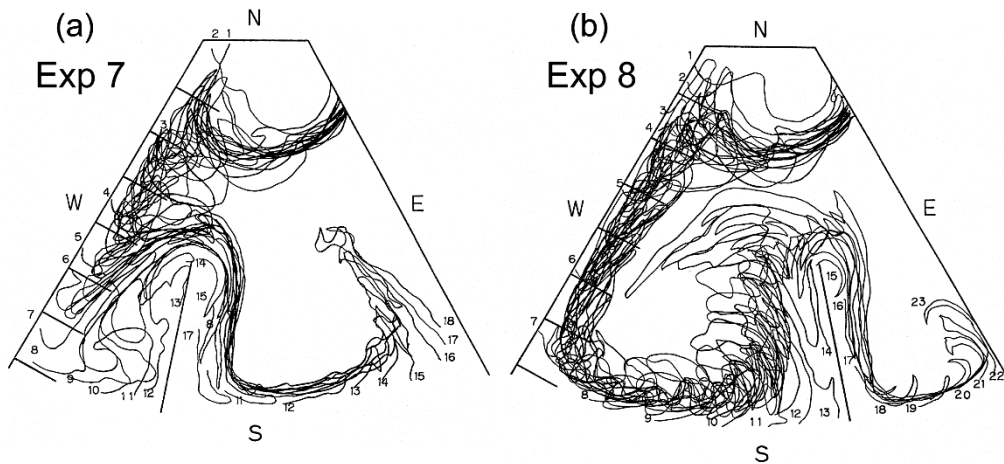


Fig. 6 Same as Fig. 4 except for Exp 7 (a) and Exp 8 (b).

point source of the *N*-basin in the experiments. Therefore, if the bottom topography of the Japan Sea were flat, with the simple topography of the Yamato Rise and Oki Spur, similar circulation pattern to the experiments is expected in the abyssal Japan Sea.

Figure 7 shows the mean flow vectors in the abyssal Japan Sea (> 1000 m) from direct current observations; this is the updated version of Fig. 3b in SENJYU *et al.* (2005b) adding our new data as well as these of FUKUSHIMA and KOJIMA (2011) and TEAGUE *et al.* (2005). By comparing with the flow pattern of the partial barrier experiments (Figs. 4–6), we found several common features.

The first is the cyclonic circulation in the southern basins (the Tsushima and Yamato Basins). The cyclonic circulation has been interpreted as a flow trapped on the slope of the basin's periphery, seeing shallow region on its right-hand side (CHOI and YOON, 2010). In fact, the observed flows tend to follow the contours of ambient potential vorticity (f/H , where H is bottom depth), which indicates that the topographic β -effect is more important than the planetary β -effect.

The second common feature that is interesting is the strong currents along the western boundary in the southern basins. We can find strong flows faster than 3 cm s^{-1} along the southeastern flank of the Yamato Rise in the Yamato Basin and the western periphery of the Tsushima Basin east of the Korean Peninsula. These strong flows are likely to be the WBC in each basin, a characteristic feature of the SA-type circulation.

The third common feature is that the water in the *SE*-basin is older than that in the *SW*-basin (FALLER, 1960). It has been considered that the Japan Sea Proper Water in the Yamato Basin is the oldest water in the Japan Sea, because it has the lowest concentration of dissolved oxygen in the sea (SUDO, 1986; GAMO *et al.*, 1986, SENJYU and SUDO, 1993 & 1994; SENJYU *et al.*, 2005a). However, the reason is probably different from the experiments. In the experiments, the WBC-SE was fed by the northward flow in the *SW*-basin, except in case of Exp 6 (Fig. 5b). While in the Yamato Basin, the deep and bottom waters are supplied directly from the Japan Basin, similar to Exp 6. It is meaningful that if we normalize the shallow ridge from the Yamato Rise to Oki Spur (about 560 km) by the latitudinal extent of the

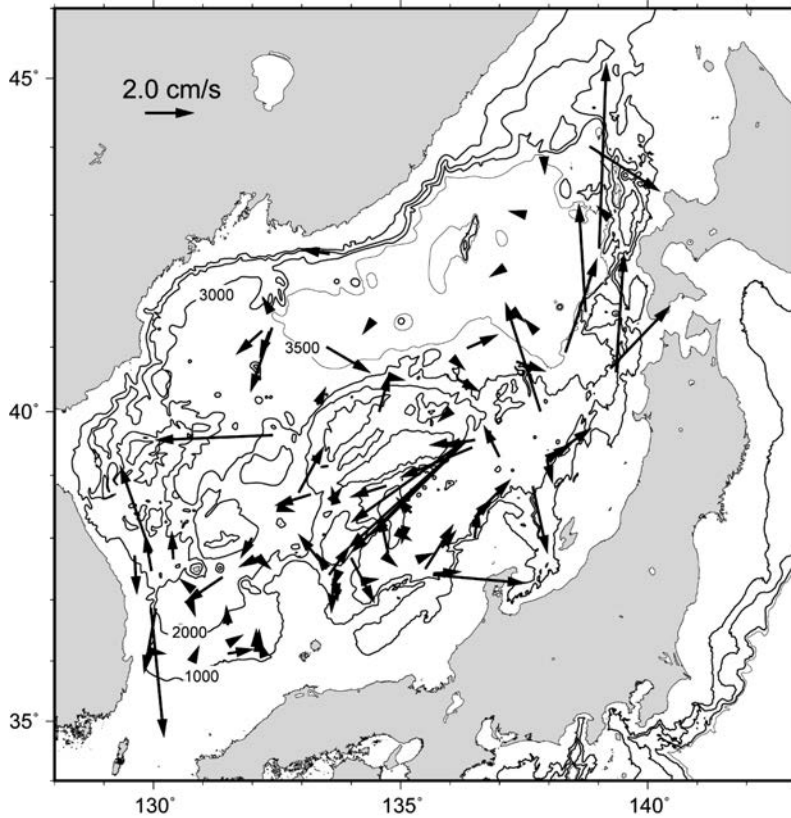


Fig. 7 Distribution of the mean flow vectors in the abyssal Japan Sea (1000 m-bottom) from direct current observations. A vector length of 2.0 cm s^{-1} is shown in the upper-left corner.

Japan Sea (roughly 1000 km), the non-dimensional length (B) is 0.56 as in Exp 6. Nevertheless, because of the narrow channel between the Japan and Yamato Basins, the water exchange between the basins is limited (SENJYU *et al.*, 2013, SENJYU *et al.*, 2017), and the water in the Yamato Basin is a modified water that has lower dissolved oxygen concentration due to the closed circulation in the basin (SENJYU *et al.*, 2005a, b).

However, there are many different points between the experiments and observations. For example, remarkable northward flows in the eastern Japan Basin cannot be explained by the SA-

type circulation. The basic SA-type circulation is likely to be strongly modified not only by the complex bottom topography, but also by eddy activity (CHOI and YOON, 2010; YOSHIKAWA, 2012).

5 Concluding remarks

We have made a qualitative discussion throughout, focusing on the geometric similarity between the partial barrier experiments and the Japan Sea. There are several common features between the experiments and the observed deep flow field in the sea. The cyclonic circulation and strong currents near the western boundary in the Yamato and Tsushima Basins suggest the

SA-type circulation. However, the complex bottom topography and eddy activity are likely to modify the basic SA-type circulation pattern.

The key strategy to confirm the SA-type circulation in the Japan Sea is to perform observations of the deep WBC in the Japan Basin. However, it flows in the North Korean territory which is an inaccessible area due to political problems at present. Data analysis of neutral drifters, such as ARGO floats, may be an effective way. In addition, chemical tracer observations are useful in capturing the deep flow pattern. Hydrographic observations in a wide area including Russian and Korean territories are desired.

Nowadays, studying geophysical fluid dynamics with the help of rotating-tank experiments is somewhat out-of-date. However, in general, laboratory experiments have an advantage of providing an intuitive understanding of phenomena. Therefore, we believe that laboratory experiments including rotating-tank experiments are still valuable not only in the field of education but also in heuristic research, even though numerical model experiments have highly progressed.

Acknowledgments

This work is a contribution to the JY's retirement ceremony. TS wishes to thank Emeritus Professors Hideo Sudo and Masaji Matsuyama in Tokyo University of Fisheries (present Tokyo University of Marine Science and Technology) for useful discussion and encouragement in TS's master course student days. Part of this study was supported by the Environment Research and Technology Development Fund of Ministry of the Environment, Japan (2-1604) and JSPS KAKENHI Grant Number 18H03741.

References

- BROECKER, W. S. and T.-H. PENG (1982): Tracers in the Sea. A publication of the Lamont-Doherty Geological Observatory, Columbia University, New York, 690 pp.
- CHOI, Y. G. and J.-H. YOON (2010): Structure and seasonal variability of the deep mean circulation of the East Sea (Sea of Japan). *J. Oceanogr.*, **66**, 349-361. doi:10.1007/s10872-010-0031-y.
- FALLER, A. J. (1960): Further examples of stationary planetary flow patterns in bounded basins. *Tellus*, **12:2**, 159-171.
- FUKUSHIMA, S. and T. KOJIMA (2011): Characteristics of deep current observed near the bottom in the Sea of Japan. Report of Hydrographic and Oceanographic Researches, Hydrographic and oceanographic department, Japan Coast Guard, **47**, 32-43.
- GAMO, T. and Y. HORIBE (1983): Abyssal circulation in the Japan Sea. *J. Oceanogr. Soc. Japan*, **39**, 220-230.
- GAMO, T., Y. NOZAKI, H. SAKAI, T. NAKAI and H. TSUBOTA (1986): Spatial and temporal variations of water characteristics in the Japan Sea bottom water. *J. Mar. Res.*, **44**, 781-793.
- KUO, H.-H. and G. VERONIS (1971): The source-sink flow in a rotating system and its oceanic analogy. *J. Fluid Mech.*, **45** (3), 441-464.
- LONG, R. R. (1954): Note on TAYLOR's "ink walls" in a rotating fluid. *J. Meteor.*, **11**, 247-249.
- SENJYU, T. (1988): Study on abyssal circulation by rotating-tank experiments. Master's thesis, Tokyo University of Fisheries, 71 pp. (unpublished manuscript)
- SENJYU, T. and H. SUDO (1993): Water characteristics and circulation of the upper portion of the Japan Sea Proper Water. *J. Mar. Sys.*, **4**, 349-362.
- SENJYU, T. and H. SUDO (1994): The upper portion of the Japan Sea Proper Water; its source and circulation as deduced from isopycnal analysis. *J. Oceanogr.*, **50**, 663-690.
- SENJYU, T., T. ARAMAKI, S. OTOSAKA, O. TOGAWA M. DANCHENKOV, E. KARASEV and Y. VOLKOV (2002): Renewal of the bottom water after the winter 2000-2001 may spin-up the thermohaline circula-

- tion in the Japan Sea. *Geophys. Res. Lett.*, **29** (7), doi: 10.1029/2001GL014093.
- SENJYU, T., Y. ISODA, T. ARAMAKI, S. OTOSAKA, S. FUJIO, D. YANAGIMOTO, T. SUZUKI, K. KUMA and K. MORI (2005a): Benthic front and the Yamato Basin Bottom Water in the Japan Sea. *J. Oceanogr.*, **61**, 1047–1058, doi:10.1007/s10872-006-0021-2.
- SENJYU, T., H. R. SHIN, J.-H. YOON, Z. NAGANO, H. S. AN, S. K. BYUN and C. K. LEE (2005b): Deep flow field in the Japan/East Sea as deduced from direct current measurements. *Deep-Sea Res. II*, **52**, 1726–1741. doi:10.1016/j.dsr2.2003.10.013.
- SENJYU, T., T. ARAMAKI, S. S. TANAKA, J. ZHANG, Y. ISODA, Y. KUMAMOTO, S. HIBINO and T. NAKANO (2013): Abyssal water mass exchange between the Japan and Yamato Basins in the Japan Sea. *J. Geophys. Res. Ocean*, **118**, 4878–4888, doi: 10.1002/jgrc.20373.
- SENJYU, T. and T. ARAMAKI (2017): Volume transport from the Japan Basin to the Yamato Basin in the abyssal Japan Sea inferred from direct current observations. *J. Oceanogr.*, **73**, 235–247, doi: 10.1007/s10872-016-0399-4.
- STOMMEL, H. (1958): The abyssal circulation. *Deep-Sea Res.*, **5**, 80–82.
- STOMMEL, H., A. B. ARONS and A. J. FALLER (1958): Some examples of stationary planetary flow patterns in bounded basins. *Tellus*, **10:2**, 179–187.
- STOMMEL, H. and A. B. ARONS (1960a): On the abyssal circulation of the world ocean- I. Stationary planetary flow patterns on a sphere. *Deep-Sea Res.*, **6**, 140–154.
- STOMMEL, H. and A. B. ARONS (1960b): On the abyssal circulation of the world ocean- II. An idealized model of the circulation pattern and amplitude in oceanic basins. *Deep-Sea Res.*, **6**, 217–233.
- SUDO, H. (1986): A note on the Japan Sea Proper Water. *Prog. Oceanogr.*, **17**, 313–336.
- SWALLOW, J. C. and L. V. WORTHINGTON (1961): An observation of a deep countercurrent in the western North Atlantic. *Deep-Sea Res.*, **8** (1), 1–21.
- TALLEY, L. D., G. L. PICKARD, W. J. EMERY and J. H. SWIFT (2011): *Descriptive Physical Oceanography. An Introduction*. Sixth Edition, Elsevier, MA, USA, ISBN: 978-0-7506-4552-2.
- TEAGUE, W. J., K. L. TRACEY, D. R. WATTS, J. W. BOOK, K.-I. CHANG, P. J. HOGAN, D. A. MITCHELL, M.-S. SUK, M. WIMBUSH, J.-H. YOON (2005): Observed deep circulation in the Ulleung Basin. *Deep-Sea Res. II*, **52**, 1802–1826.
- VERONIS, G. and C. C. YANG (1972): Nonlinear source-sink flow in a rotating pie-shaped basin. *J. Fluid Mech.*, **51** (3), 513–527.
- WELANDER, P. (1969): Effects of planetary topography on the deep-sea circulation. *Deep-Sea Res.*, *supp.* **16**, 369–391.
- YOSHIKAWA, Y. (2012): An eddy-driven abyssal circulation in a bowl-shaped basin due to deep water formation. *J. Oceanogr.*, **68**, 971–983, doi:10.1007/s10872-012-0148-2.

Received: August 1, 2018

Accepted: December 21, 2018

資 料

第 56 卷第 3・4 号掲載欧文論文の和文要旨

今脇資郎¹⁾・高野健三²⁾ : 1978-1985 年に西部北太平洋の深層で係留流速計によって観測された中規模渦

西部北太平洋の海央で係留流速計による観測を繰り返し行い 50 件の流速記録を得た。深さ 5000 m 層で、ほぼ 7 年にわたる連続流速記録を得た。全期間の平均流速は北向きで速さは 1 cm s^{-1} 以下である。低周波流速変動（中規模渦）の運動エネルギーは平均流の運動エネルギーの 30 倍以上である。渦運動エネルギーの周波数スペクトルから、エネルギーの大部分が中規模の帯域（周期 30-235 日）に含まれており、周期の長い（短い）帯域では東西（南北）方向のエネルギーが卓越していることが分かった。深さ 4000 m 層でのアレー観測から、中規模渦の相対渦度の時間変化は主に惑星渦度の移流と釣り合っていることが分かった。ただし相対渦度の移流と高次の水平発散もある程度の働きをしているかもしれない。これらのことは、中規模渦が基本的に順圧ロスビー波またはその変形波として理解できることを示している。

(1 九州大学名誉教授, 横浜市都筑区牛久保東, 2 千葉県松戸市上本郷。連絡先著者: 今脇資郎 imawaki@g04.itscom.net)

千手智晴¹⁾・吉田次郎²⁾ : 日本海の深層循環に関する一考察: 回転水槽実験からの示唆

FALLER (1960) および千手 (1988) の回転水槽実験で行われた部分障壁実験との幾何学的相似性に注目して、日本海の深層循環を定性的に議論した。パイ型水槽の頂点付近に置いた水のソースによって、水槽内部にはいわゆる STOMMEL-ARONS 型の循環が形成される。部分障壁実験における循環は、基本的には、水槽縁から伸びた障壁によって隔てられた二つの海盆内の低気圧性循環と西岸境界流によって構成されている。一方、近年の直接測流によると、日本海南部の大和海盆と対馬海盆深層にも低気圧性循環と西岸境界域における強い流れが観測されている。このような類似性は日本海深層における STOMMEL-ARONS 型循環を示唆しているが、複雑な海底地形や渦活動により強く変質されていることがうかがえる。

(1 九州大学 応用力学研究所 地球環境力学部門 海洋動態解析分野 〒 816-8580 福岡県春日市春日公園 6-1 TEL 092-583-7668 FAX 092-583-7735 e-mail senjyu@riam.kyushu-u.ac.jp, 2 東京海洋大学 船舶海洋オペレーションセンター 〒 108-8477 東京都港区港南 4-5-7 jiro@kaiyodai.ac.jp)

学 会 記 事

1. 諸会議報告

2018 年度第 2 回幹事会議事録

日時：2018 年 8 月 29 日（水）15 時 00 分～16 時 30 分

場所：東京海洋大学品川キャンパス 2 号館 200B 号室

参加者：小松, 今脇, 吉田, 高柳, 小池, 田中, 荒川, 奥村, 内田, 本多（事務局）

(1) 報告事項

- ① 第 1 回水産・海洋科学研究連絡協議会（5/28, 海洋大品川キャンパス）での議論について議事録を基に出席した田中祐志幹事が報告した。
- ② 2018 年度総会, 評議員会および学術研究発表会（6/2, 日仏会館）について荒川庶務幹事が報告した。2018 年度から日仏会館会議室使用料の割引率が下がったため, 研究発表会会費の正会員参加費 2,000 円を 3,000 円に, 非会員参加費 3,000 円を 4,000 円に各 1,000 円値上げした。その結果, 今までとはほぼ同額の収支となった。（荒川）
- ③ 第 1 回日仏関連学会連絡協議会（6/25, 日仏会館）に荒川庶務幹事と本多事務員が出席した。（荒川）
- ④ 学会誌 La mer 第 56 巻 1-2 号は発送済み, 3-4 号は編集作業中で年内刊行の予定であることが報告された。（吉田編集委員長）

(2) 審議事項

- ① 2019 年度日仏海洋学会代表団受け入れ準備委員会および現況を報告した。（小松）当初, 2018 年 10 月 12 日から 19 日に岡山県備前市日生（ひなせ）, 宮城県気仙沼市, 東京日仏会館, フランス大使館での催しを予定していたが, フランス側の都合により 2019 年に延期された。準備委員会の構成は次の通りである。

委員長	小松会長
副委員長	小池渉外幹事

委員	荒川庶務幹事, 奥村庶務幹事, 中野渉外幹事, 上原顧問, 關哲夫（元・東北水研所長）
会員以外の関係者	佐々木良（元・宮城水試場長）, 田中文裕（NPO 里海づくり研究会議事務長）, 山内宏康（気仙沼リアスアーク美術館学芸員）, 等
事務局	本多事務員

- ② 第 18 回日仏海洋学シンポジウムおよび学会創立 60 周年記念事業の委員を選出した。順次, 2018-2019 年度幹事全員に委員を委嘱することにした。（小松）

委員長	小松会長
副委員長	高柳副会長
広報・シンポジウム	広報幹事（内田, 柳本）
募金	高柳副会長
特別編集委員	吉田編集委員長, 編集幹事（田中）
フランス人研究者対応	小池渉外幹事, 上原顧問
総務・業務支援・事務局	庶務幹事（荒川, 奥村）

(3) その他

- ① J-STAGE および ISSN の進捗状況について報告があった。（内田）
 - ・オンライン ISSN 登録済（8 月）, 予定番号：2434-2882
 - ・J-STAGE 各種書類提出（10 月）
 - ・J-STAGE 利用説明会（1-2 月, JST 東京本部, 参加必須）
 - ・J-STAGE 搭載のサイト提供開始（2 月以降, 1 年以内に初回公開必要, 2 回目以降はいつでも可能）
- ② 学術著作権協会より権利委託手続きの変更および転載許諾事業開始についての説明会に本多事務局員が出席する予定。（9/27 もしくは 10/2, ビジョンセンター東京）
- ③ 英語版 La mer 投稿規定を現行内容に則して修正し, ホームページや La mer に反映することにした。（吉田）

2018 年度第 3 回幹事会議事録

日 時：2018 年 12 月 7 日（金）16 時 00 分～18 時 00 分

場 所：東京海洋大学品川キャンパス 2 号館 200B 号室

参加者：小松, 今脇, 森永, 高柳, 小池, 田中, 荒川, 北出, 奥村, 内田, 本多（事務局）

(1) 報告事項

- ① 学術著作権協会主催「権利委託手続きの変更および転載許諾事業開始についての説明会」(9/27, ビジョンセンター東京)に本多事務員が出席した。
- ② 第 2 回水産・海洋科学研究連絡協議会(10/29, 海洋大品川キャンパス)に吉田副会長が出席した。(代理報告：北出)
- ③ 日仏間の海洋・水産学分野における研究および研究者の交流活動に貢献した功績に対し、フランス国家功労勲章オフィシエが小池康之会員に与えられ、叙勲式が行われた。(10/1, フランス大使公邸) (写真 1)
- ④ 学会誌 La mer 第 56 巻 3-4 号は投稿論文 4 本の予定、年内出版予定であることが報告された。(代理報告：荒川)

(2) 審議事項

- ① (一般社団法人)学術著作権協会が始める転載許諾事業について意見交換を行なった。(内田, 本多事務員)
- ② 著作物の適正な再利用の促進を目的として、著作者が自らの著作物の再利用を許可するという意思表示を手軽に行えるようにするための様々なレベルのライセンスを策定し普及を図る国際的プロジェクトの運営

主体である国際的非営利団体クリエイティブ・コモンズの発行するライセンスを La mer 掲載論文に表示するかについて提案があった。(内田)

- ③ 日仏海洋学会の新しい会員を獲得するためにどのようなことが可能か、提案を交え意見交換を行った。(奥村) また、La mer の Web of Science への掲載審査申請の提案があった。(内田)
- ④ 2019 年度日仏海洋学会代表団受け入れ準備委員会について現状報告があった。2018 年 11 月にフランス大使館による 2019 年度日仏間研究交流活動補助金の募集に対し、日仏海洋学会代表者の受入れとして申請した。(小松)
- ⑤ 第 18 回日仏海洋学シンポジウムおよび学会創立 60 周年記念事業について進捗状況を確認した。来年より準備委員会を 2 か月に 1 回程度のペースで開くことにした。(小松)
- ⑥ 英語版 La mer 投稿規定がホームページに掲載されたが、日本語の投稿規定とのズレを早急に修正することにした。

(3) その他

- ① 賞規定 3. 『出来る』から『できる』に表記変更し、2019 年度評議員会へ提案することにした。
- ② 日仏関連学会連絡協議会(2018/12/11, 日仏会館)に小松会長と本多事務員が出席予定。
- ③ 日仏会館は『カキをめぐる日仏交流：歴史、産業、文化』をタイトルとしたイベントを 2019 年度(12 月～3 月)に企画しており、当学会は共催依頼されている。試食用カキ代金は当学会負担になる等、提案の説明があった。(小松, 小池)



写真 1 小池康之会員がフランス国家功労勲章オフィシエ受章(於・フランス大使公邸, 写真提供：在日フランス大使館)

2. 新入会員

氏名	所属	種別	紹介者
久賀 みづき	水産研究・教育機構 日本海区水産研究所	正	なし
横田 峻	水産研究・教育機構 水産大学校	学	田上 英明

有本 光希	水産研究・教育機構 水産大学校	学	田上 英明
生平 遥菜	水産研究・教育機構 水産大学校	学	田上 英明
永井 節子	水産研究・教育機構 水産大学校	学	田上 英明

3. 所属および住所変更

氏名	新しい所属先
中野 知香	東京海洋大学 環境測定学研究室 〒108-8477 東京都港区港南 4-5-7
松本 陽	福島県水産資源研究所 〒976-0005 福島県相馬市光陽 1-1-14
土井 航	鹿児島大学 水産学部 〒890-0056 鹿児島県鹿児島市下荒田 4-50-20

4. 退会

関根義彦

5. 寄贈図書

Ocean Newsletter (海洋政策研究財団) : No.429-440
国立科学博物館研究報告 A 類 (動物学) : 第 44 卷第 2 号-第 3 号

Ocean Breeze (東京大学大気海洋研究所) : 第 28 号-第 29 号

東京大学大気海洋研究所 要覧・年報 2018

なつしま (JAMSTEC) : 通巻 369 号-371 号

FRANEWS (水産総合研究センター) : No.55-56

Techno-ocean News (テクノオーシャンネットワーク) : No.67

広島日仏協会報 BULLETIN No.205

農村工学研究部門成果情報 平成 29 年度

農村工学通信 ; No.112-113

東京大学大気海洋研究所 メール通信 ; 第 12 号

賛 助 会 員

株 式 会 社 イ ー エ ム エ ス	兵庫県神戸市中央区東川崎町 1-3-3 神戸ハーバーランドセンタービル 13 F
い で あ 株 式 会 社	東京都世田谷区駒沢 3-15-1
公益財団法人海洋生物環境研究所	東京都新宿区山吹町 347 藤和江戸川橋ビル 7 階
ケー・エンジニアリング株式会社	東京都台東区浅草橋 5-14-10
J F E アドバンテック株式会社	兵庫県西宮市高畑町 3-48
株 式 会 社 新 協	東京都文京区大塚 4-40-1
株 式 会 社 セ ア ・ プ ラ ス	神奈川県横浜市緑区十日市場町 822-10
株 式 会 社 独 立 総 合 研 究 所	東京都江東区

(※詳細はセキュリティのため非公開)

日仏海洋学会入会申込書

(正・学生会員)

申込日 年 月 日
年度より入会

私は日仏海洋学会会則に同意し、下記の通り入会を申し込みます。

フリガナ			
氏名			
ローマ字			
生年月日	年 月 日	会誌送り先 (自宅 / 勤務先)	
メールアドレス			
勤務先			
勤務先住所	〒		
自宅住所	〒		
TEL		FAX	
紹介会員名			

■会員種別および会費 (不課税)

正会員：8,000円

特別会員^(※)：6,000円

学生会員：4,000円

賛助会員：1口10,000円以上

※年度初めに満65歳以上で学会事務局へ申告した者

■事業年度 4月1日～翌年3月末日

■備考

入会申込書送付先：〒150-0013 東京都渋谷区恵比寿3-9-25

(財)日仏会館内

日 仏 海 洋 学 会

郵便振替番号：00150-7-96503

日仏海洋学会入会申込書

(賛助会員)

申込日 年 月 日
年度より入会

日仏海洋学会会則に同意し、下記の通り入会を申し込みます。

フリガナ			
会社・機関名			
住所	〒		
TEL		ご担当者名	
FAX		所属	
口座数 (1口1万円より)	口	メールアドレス	
紹介会員名		TEL	

■事業年度 4月1日～3月末日

■備考

入会申込書送付先：〒150-0013 東京都渋谷区恵比寿 3-9-25

(財) 日仏会館内

日 仏 海 洋 学 会

郵便振替番号：00150-7-96503